The Dissertation Committee for Daiju Uehara
certifies that this is the approved version of the following dissertation:

Estimation of Helicopter Rotor Loads from Blade Structural Response

Committee:

Jayant Sirohi, Supervisor

David B. Goldstein

Krishnaswa Ravi-Chandar

Jeffrey K. Bennighof

Mahendra J. Bhagwat

Estimation of Helicopter Rotor Loads from Blade Structural Response

by

Daiju Uehara

DISSERTATION

Presented to the Faculty of the Graduate School of

The University of Texas at Austin

in Partial Fulfillment

of the Requirements

for the Degree of

DOCTOR OF PHILOSOPHY

THE UNIVERSITY OF TEXAS AT AUSTIN

December 2019

Dedicated to my family, for their endless love, support, and encouragement.

Acknowledgments

First of all, I would like to express my sincere gratitude to my academic advisor and mentor in life, Prof. Jayant Sirohi. On the first day I came to Austin, I was a young Japanese kid who had no experience of living outside Japan, studying rotorcraft, and even speaking English. Even so, from the first day to the end of my PhD program, Prof. Sirohi has been patient, and always listened to me. If he had not been my advisor, I would have gone back to Japan by the end of the first year without earning any degree. He shared a variety of his personal stories and experiences from the old-days memories when he was a young PhD student just like myself. These stories taught me that even a great professor and teacher, Prof. Sirohi, had gone through tough challenges similar to those that I have faced during the graduate school. His advice, as an academic advisor and as a person who had overcome the similar challenges and achieved success, helped me in all the time.

In addition to my advisor, I would like to acknowledge the rest of the dissertation committee: Prof. David Goldstein, Prof. K. Ravi-Chandar, Prof. Jeffrey Bennighof, and Dr. Mahendra Bhagwat, for their invaluable suggestions and comments to my thesis and during the proposal and defense. Their broad and critical comments to my research opened up new horizons that I would have never come up with by myself.

My sincere thanks also goes to Dr. Christopher Cameron and Dr. Anand Carpatne, who were my senior PhD students in the research group. Chris and Anand provided significant support not only for academic, research-related topics, but also for my private life. I do not know how many times I asked questions to them, how many times I had drink with them, and how many times we laughed together. I am so lucky that I had Chris and Anand as my seniors.

I would like to thank my research collaborators: Dr. Roland Feil, Dr. Juergen Rauleder, and Dr. Larry Matthies. Roland and Juergen provided detailed, thorough understanding of rotorcraft dynamics from the perspective of numerical modeling, and improved the quality of our collaborative conference proceedings and peer-reviewed journal publications. Larry gave me an internship opportunity at NASA JPL in 2018 summer, and provided insights to the collaborative work, mission modeling of small VTOL aircraft for exploration of Titan. Thanks to these collaborators, I was able to write and publish 5 research papers in total, based on these collaborations.

I thank my fellow lab colleagues: Young-Joon, Jason, Sergio, Palash, Marc, Krystal, Patrick, Chloe, and Matt, for the countless discussions and meetings, for the informal conversations, and for all the fun we have experienced together in the last five and half years. Besides the colleagues in the research group, I would also like to appreciate all of my friends who I met at UT Austin. I want to keep in touch with all of them for the rest of my life.

Lastly, of course, I would like to thank my family. My parents and

sisters have always supported me with love. At every turning point of my life, including when I decided to leave my home town Okinawa and go to Tokyo after high school, and when I decided to leave my home country Japan and go to the United States after undergraduate, my parents just encouraged me to do so. They did not show me how they felt in their heart at all, just gave the push I needed. I just want to say, thank you.

Estimation of Helicopter Rotor Loads from Blade Structural Response

Publication No. _____

Daiju Uehara, Ph.D.
The University of Texas at Austin, 2019

Supervisor: Jayant Sirohi

Measuring the load distribution along a helicopter rotor blade has been one of the most challenging tasks in experimental aeromechanics. Conventional loads measurements with on-blade instrumentation, such as pressure transducers for airloads and strain gages for structural loads, require the experimentalist to overcome a large number of technical barriers; for example, sensor integration to the rotor blade structure, sensor failure due to strong centrifugal forces, and influence of sensor installation on rotor blade dynamics. The goal of this dissertation is to develop a new, combined experimental and theoretical methodology to estimate helicopter rotor loads without using these conventional on-blade sensors.

The rotor loads estimation methodology begins with the measurement of blade structural deformation measurements using non-contact, optical, time-resolved Digital Image Correlation (DIC). The time-resolved DIC technique

successfully showed its capability of measuring the three-dimensional deformation time history of a rotating blade for both a small- and a large-scale rotor in hover. The modal properties (natural frequencies, mode shapes, damping ratios, and modal coordinates) of the blade in the rotating-frame were then extracted from the deformation time history using Natural Excitation Technique - Eigensystem Realization Algorithm (NExT-ERA) and Complexity Pursuit (CP), which are operational modal analysis (OMA) algorithms. The first three modes were identified by the OMA algorithms and well correlated with a numerical model. Rotor loads were then finally estimated based on the measured deformations and blade modal characteristics.

Having validated the present approach incrementally with measurements performed on rotors at different scales, configurations, and operating conditions, the current study estimated the spanwise lift distribution and integrated thrust at the hub for a 2 m-diameter, two-bladed, isolated single rotor in hover. Due to a lack of participating modes (only the first and second flap modes), the estimated sectional lift distribution did not capture the lift loss typically observed at regions of the blade tip and induced by trailing tip vortices. Nevertheless, the mean value of the estimated thrust at the rotor hub was within 5% of the measured value for all the operating conditions.

Table of Contents

List of Tables

List of Figures

Chapter 1

Introduction

1.1 Problem Statement

Understanding rotor vibratory loads remains an essential task for helicopter design. Helicopters typically encounter significant vibration in transition or high-speed flight regimes, due to aerodynamic phenomena such as blade-vortex interaction (BVI) and negative loading on the advancing side. Those loadings induce significant elastic deformations of the rotor blade structure during helicopter operations as shown in Fig. 1.1. To understand the nature of rotor loads due to the structural and aerodynamic loadings, a number of flight and wind tunnel tests have been performed in the past [3, 4, 5]; however, measuring rotor loads is still one of the most challenging assignments of experimental research in the rotorcraft field. Direct surface pressure measurements using on-blade pressure transducers is a typical methodology for measuring aerodynamic forces on a rotor blade, while structural loads (or inertial loads) are conventionally measured with on-blade strain gages as shown in Fig. 1.2. In order to perform these rotor loads measurements, experimentalists need to overcome several technical barriers, such as the installation of sensors and electrical wiring on a rotor blade, usage of expensive slip rings, and sensor failure due to strong centrifugal forces. Aerodynamics and structural

dynamics of the rotor blade can also be significantly altered by installation and modifications to accommodate the pressure transducers, static pressure taps, and strain gages.

Figure 1.1: Comparison between images taken during static display and flight operation of the CH-53 Sea Stallion [1, 2]

These challenges have motived an alternate approach to investigate helicopter rotor loads; that is, airloads estimation strategies based on the structural response of a rotor blade. The capability of estimating rotor loads using only measured structural response would not only reduce cost and time to complete measurements, but also help one to understand the complex rela-

tionship between the structural and aerodynamic loads on a helicopter rotor. Bousman [6] provided a good summary of previous airload estimation methodologies, as well as his method that estimates blade aerodynamic forces based on measured flap bending moments and modal parameters of a rotor blade. This work showed good agreement between the estimated and directly measured spanwise aerodynamic loadings, except for regions near the blade tip. Wang et al. [7] discussed a combined analytical-experimental approach to predict the vibratory loads in an articulated rotor. In this study, the estimated airloads were obtained based on strain measurements as well as the lifting-line aerodynamic and finite element blade structural models, with a satisfactory agreement to the corresponding flight test data. These previous studies have shown that aerodynamic estimations appeared to be theoretically robust and feasible for prediction of rotorcraft dynamic behaviors; however, the method-

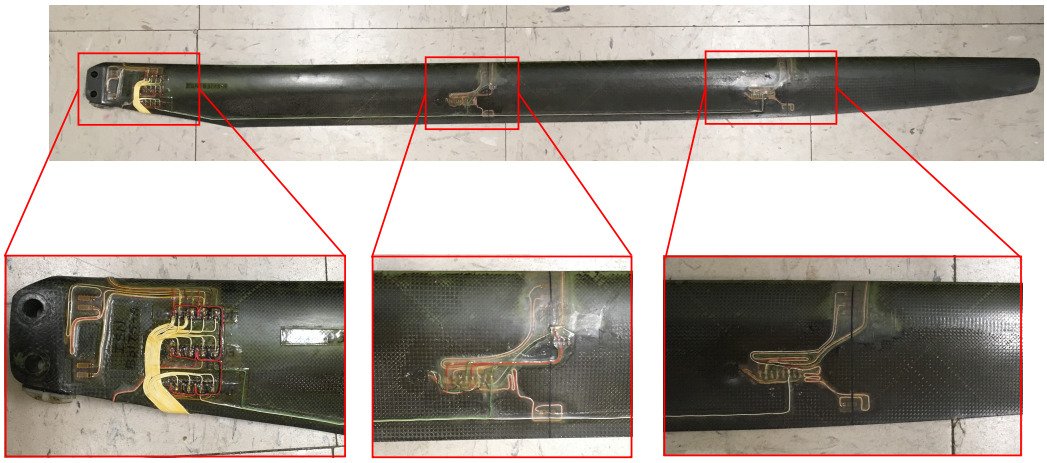

Figure 1.2: An example of complex on-blade strain gage instrumentation

ologies used in these studies rely on precise identification of modal parameters of a rotating rotor blade (i.e., mode shapes, modal amplitudes, and natural frequencies), as well as data measured by pointwise on-blade sensors (i.e., strain gages). The former would necessitate additional experiments (modal tests) or to develop an accurate finite element model of the blade structure, while the latter would require extensive preparation for measurements with challenges inherent to operating in a high centrifugal force environment.

In other words, the helicopter rotor loads estimation can be achieved if the two major problems mentioned above, one relevant to modal parameter identification and the other relevant to on-blade sensor failure, are addressed. As a possible approach to modal characteristics extraction, this dissertation introduces a system identification algorithm, called Operational Modal Analysis (OMA). The OMA, also called output-only modal analysis, is widely recognized as an attractive technique to extract modal parameters of a structure in its operating condition. The significance of the OMA is that it only requires measurement of the resultant responses of a structure under ambient or operational excitation, in contrast to classical modal analysis that requires measurements of both the input and output. This feature makes OMA well-suited for investigating the dynamic behavior of a rotating rotor blade, especially considering the challenge of measuring aerodynamic excitation forces.

The other concern for a successful rotor load estimation, on-blade sensors failure, can be resolved by introducing non-contact optical measurement techniques that requires no troublesome preparation and installation of sen-

sors on a target specimen. To date, the optical methodologies have been applied to a variety of different structural engineering fields, including helicopter rotor blade deformation and strain measurements in the rotating frame; for example, photogrammetry, holographic interferometry, and projection moiré interferometry (PMI). Among quite a few of these methodologies, this dissertation selects the Digital Image Correlation (DIC) deformation measurement technique, since the DIC technique has shown its robustness in measuring rotor blade deformations at different rotor configurations and scales, as discussed in [8, 9, 10, 11]. The DIC deformation measurement technique is able to measure three-dimensional displacements over the entire blade span at a high spatial resolution with minimal preparation of the test article (i.e., painting the rotor blade surface with stochastic speckle patterns).

This dissertation presents a new experimental and theoretical methodology for helicopter rotor loads estimation based on blade structural response. Theoretical developments of the three key components of the methodology (digital image correlation, operational modal analysis, and rotor loads identification) are first presented. Three different model-scale rotor hover test stands used for verification of the proposed experimental and theoretical framework are then described. The results of hover tests on the three different rotor systems are presented with a focus on the rotor blade deformations, modal parameter identifications, and rotor loads reconstructions.

1.2 State of the Art

This section discusses the literature related to the three core elements of the present study: the optical deformation measurement techniques, the operational modal analysis (OMA) algorithms, and rotor loads estimation methodologies.

1.2.1 Optical deformation measurement

Digital Image Correlation (DIC) is categorized as a photogrammetric measurement technique. Photogrammetry is an image-based optical measurement technique that has been commonly applied to structural deformation monitoring due to its robustness and ability to capture full-field deformation of the target structure, with the help of digital cameras and powerful computers [12]. In the applications to rotating structures, optical measurement techniques can be divided into three major categories:

- Grid method
- Point Tracking
- Digital Image Correlation

1.2.1.1 Grid method

The grid method is one of the earliest optical methods for measurement of structural deformations [13]. The basic procedure of the grid method is as follows; (1) regular marking patterns are applied to the target surface of a

test specimen, (2) diffusive light reflection from those patterns are recorded, (3) the differences between two grid images are used to calculate the deformations of the structure. The projected grid method was used for the Higher Harmonic Control Aeroacoustic Rotor Tests (HART) program, performed by Kube et al. [14]. The method provided flapwise and torsional deflections along the blade span at selected azimuthal angles, and its results were compared to signals measured by on-blade strain gages. Electronic Speckle Pattern Interferometry (ESPI) and Projection Moiré Interferometry (PMI) are other non-contact optical approaches. The former electronically observes formation of fringes and records images of the reference (undeformed) and deformed objects [15, 16], while the latter evaluates fringe interference patterns between the deformed projected grid and a computationally phase-shifted grid to calculate out-of-plane displacements [17, 18]. Recently, Sekula [19] employed PMI to measure blade deformations of a model-scale rotor in hover in the NASA Langley subsonic wind tunnel and hover test facility, and successfully acquired the out-of-plane hub height, tip height, and the flap angles of the 66.5 in (1.69 m)-radius target blade. These results showed that measuring blade deflection using digital images is feasible.

1.2.1.2 Point Tracking

The key idea of the point-tracking optical deformation measurement is to place reflective markers onto the surface of a target structure and track the motion of the markers by digital cameras. A few examples of this methodology

are shown as follows:

Three-Dimensional Point Tracking (3DPT) technique is an optical technique that identifies and tracks the coordinates of discrete and reflective points mounted on the target structure. Ozbek et al. [20, 21, 22] utilized the 3DPT technique to measure the dynamic response of a 80 m diameter rotor on a 2.5 MW wind turbine using four CCD cameras, and achieved an average accuracy of 25 mm over a measurement window of 220 m. Schneider [23] introduced the Stereo Pattern Recognition (SPR) technique for rotor blade position and deflection measurements on a 40% Mach-scaled model helicopter rotor in a wind tunnel and successfully measured the blade displacements using four digital cameras located underneath the rotor. Abrego et al. [24] performed blade displacement measurements using multi-camera stereo photogrammetry during the full-scale wind tunnel testing of the UH-60A rotor and compared the experimental results with CFD/CSD predictions. Baqersad et al. [12] provided a good summary of photogrammetry and optical methods in the context of structural dynamics. Lundstrom et al. [25], combined 3DPT and modal parameter identification to monitor the dynamics of a 10.1-m diameter helicopter main rotor; they were able to extract the rotating natural frequencies and operating deflection shapes (ODS). Javh et al. [26] also performed a hybrid measurement, combining photogrammetry and several modal parameter identification methods and successfully identified the eigenvalues and mode shapes from a set of very noisy digital images, though this measurement was not performed on rotary machines.

1.2.1.3 Digital Image Correlation

The basic, two-dimensional digital image correlation (2D DIC) technique was first developed in 1980s following the wide usage of the projected grid method, in order to measure in-plane deformation and strain field. Since then, the same technique has been called with different names in the literature; for example, texture correlation, electronic speckle photogrammetry, and digital speckle correlation. Peters and Ranson [27] developed the theoretical basis of the digital correlation of speckle images with a simple measurement of rigid body translational motion. Theory of DIC was then validated in the literature through measurements of deflections of a cantilever beam [28, 29]. Chu et al. [30] also corroborated these findings through the measurement of rigid-body rotation, constant-angular velocity, and uniform-finite strain. Image correlation approach with subdivided small interrogation windows, which is commonly implemented in modern DIC algorithms, was introduced in late 1990s by McNeill et al. [31] for accurate and rapid camera calibrations and profiling of target structure images.

In the DIC technique, a random speckle pattern is painted on the surface of target structure undergoing deformation and digital images of the surface are captured before and after deformation. Cross-correlation of these images in conjunction with calibration of a stereo pair of cameras yields the three-dimensional deformation of the surface over the whole field of the image. DIC has the capability of not only capturing a large field of vision, but also measuring extremely small deformation of a structure on the order of a few

microns [32]. Although ESPI also has the capability of measuring small structural motion on the same order of sensitivity, it is not well-suited for measuring large deflections of a structure unlike DIC approach. Another advantage of DIC is its ready applicability to dynamic deformation measurements. These instantaneous measurements can be analyzed by a dynamic sequence of digital images taken by high-speed image recording equipment. Schmidt et al. [33] used a stereoscopic set of high-speed cameras with a pulsed YAG laser as a light source to measure rapid deformations of a road wheel tire, achieving a short exposure time of 7 nanoseconds.

Over the past few years, special attention has been paid to the DIC technique not only in the field of experimental structural and solid mechanics, but in a large number of different research and engineering fields, such as tensile testing of a knee tendon, deformation of a frog heart, tissue studies, and testing of biomimetic materials in microscopic biomechanics [34]. The fundamental 2D DIC framework itself has been extensively investigated and improved towards reducing computational cost, widening application range, and achieving high accuracy and precision. One critical expansion of the application area was to be capable of measuring out-of-plane, three-dimensional deformation over the curved surface of a structure.

The three-dimensional DIC (3D DIC) is the technique used in the present study. The 3D DIC has been applied to different types of rotor blade deformation measurements. For example, Sirohi and Lawson [8, 9] used the 3D DIC method to measure the deformation of a model-scale rotor blade at sev-

eral azimuthal locations using a phase-averaging technique, that is, the images are captured at a specific azimuthal location and averaged over multiple rotor revolutions. The process is repeated at a different azimuthal location, yielding an average deformation at each azimuthal location [10, 11]. However, due to the averaging process, these deformations are not correlated in time. Sicard and Sirohi [9] utilized the 3D DIC technique to measure the deformation of an extremely flexible rotor blade at a specific azimuthal location with validation performed using laser displacement sensor measurements and an aeroelastic numerical simulation tool. The DIC measurement technique was also used by Cameron et al. [35] to measure the rotating modal properties of a flexible blade in a reduced-scale coaxial helicopter rotor over a field of view limited to one quarter of the rotor disk.

Although both the 2D and 3D DIC method have proven to be useful tools for full-field rotor blade deformation measurement in rotating frame, none of the past studies have measured the time history of deformation of a rotating helicopter rotor blade. The present study extends the range of 3D DIC measurement over a much larger field of view with the spatial resolution on the order of 0.1% of a rotor radius, in order to obtain the continuous time history and transient deformations of a model-scale rotor blade in hover.

1.2.2 Operational Modal Analysis

Operational Modal Analysis (OMA) only requires measurement of the response of a structure under ambient or operational excitation, in contrast to

classical experimental modal analysis (EMA) that requires measurements of both the input and output information. Since the beginning of its development in civil engineering, OMA methodologies have been proposed in a wide variety of engineering applications, particularly in situations where measuring input forcing or exciting the structure is impractical, such as in large-scale bridges, buildings, aircraft, and wind turbines.

There are a number of different OMA techniques formulated in the past. Of them, this dissertation focuses on four algorithms that have been applied to a number of different engineering and research fields including rotary structures, such as wind turbines and helicopters. A list of the algorithms is as follows:

- Ibrahim Time Domain (ITD) method
- Eigensystem Realization Algorithm (ERA)
- Natural Excitation Technique (NExT)
- Complexity Pursuit (CP)

The Ibrahim Time Domain (ITD) is categorized as a time-domain modal identification algorithm and utilizes free-response time histories measured at several measurement points on a target structure. The theoretical basis was proposed and developed by Ibrahim in 1977 [36], and has been used to extract the modal characteristics of several types of structures such as cantilever beams or spacecraft payloads [37]. Recently, Rizo-Patron and Sirohi [11]

used the ITD method to extract the modal properties of a cantilever beam and a model-scale, conventional rotor blade under rotation. Cameron et al. [35] identified the rotating natural frequencies and mode shapes of a rotor blade on a reduced-scale coaxial, counter-rotating rotor system using the modified version of ITD algorithm. Two common features in these two previous studies are: (i) the excitation to the spinning structure was a periodic gust from a compressed air source, and (ii) the deformation measurements were not continuous in time. Nevertheless, the ITD algorithm was able to identify the first three flap-bending natural frequencies and mode shapes.

The Eigensystem Realization Algorithm (ERA) is essentially a system realization methodology that realizes a linear model for a dynamic system, and the realized system can be transformed into modal space for modal parameter identifications. Juang and Pappa [38] first developed the basis of ERA and applied it to the modal testing on the Galileo spacecraft. Since then this algorithm has been used for various problems; for example, in fluid mechanics for flow control [39] and model reduction, and in civil engineering for modal testing on large-scale structures [40].

The Natural Excitation Technique (NExT) is another methodology of modal analysis that allows derivation of pseudo-impulse response functions based only on output information. The NExT is in general employed together with a time domain modal identification scheme, such as the ERA or the Poly-reference Time Domain algorithm. Regarding the applications to rotating machinery, James et al. [41] performed modal testing with the NExT on

vertical and horizontal axis wind turbines, and there have been a number of follow-up studies to this pioneering work in wind turbine research and development [42, 43, 44].

The Complexity Pursuit (CP) algorithm belongs to a broad family of Blind Source Separation (BSS) algorithms. In general, signals measured in any physical system are a mixture of statistically independent source signals [45]. Blind Source Separation is a methodology that allows identification and separation of the sources without any input information. The usefulness of the BSS techniques has been demonstrated for a diverse variety of data analyses, such as financial time series of the Japanese stock market [46] and human brain imaging dynamics [47]. The application to structural analysis was introduced by Roan et al. [48] for damage detection and condition health monitoring of a structure, and Kerschen et al. [49] described structural modal analysis using a BSS technique called Independent Component Analysis, along with numerical validations. The general concept of the CP algorithm was first formulated by Stone [50] in the field of neural computation and applied to structural modal parameter extraction by Yang and Nagarajaiah [51].

As described above, these OMA algorithms have proved their worth as tools for modal identification of different types of structures, including a helicopter or wind turbine rotor blade. However, most of the past studies applied the OMA algorithms to the deformation that was obtained by traditional, conventional instrumentation, such as strain gages at a limited number of measurement points. Only few studies in the literature have combined OMA and

optical deformation measurement techniques, although OMA in conjunction with the non-contact optical measurement methods seems to have great potential for reducing traditional difficulties of identifying rotor blade structural dynamic characteristics. Thus, the current study in this dissertation applies all the four methodologies to rotor blade structural responses measured using the DIC technique, and evaluates the compatibility and applicability of each OMA algorithm to the optically-obtained structural deformation.

1.2.3 Rotor loads estimation from structural response

Rotor loads estimation or rotor loads identification is a theoretical framework for the determination of helicopter rotor loads based on measured structural response. The identification includes the aerodynamic and structural loads on the rotor. This concept has been discussed in the rotorcraft community because the determination of blade structural response is much more tractable than that of blade airloads. Direct surface pressure measurement with on-blade transducers is still a challenging task for experimentalists due to extensive preparation for measurements with a high likelihood of sensor failure caused by high vibration and centrifugal forces.

Although there exist various approaches for rotor load identification, which are well summarized in Ref. [52], a number of previous studies can be classified as normal modes or modal superposition methodologies. Somerson [53] presented a methodology of estimating rotor inflow and flapwise airloads distribution based on the inertial force distribution associated with nor-

mal modes of the rotor blade, with measured flap bending strain and blade root motion. Bousman [6] also proposed the rotor flapwise loads estimation technique based on a modal expansion of the flapping beam equation of motion with the aid of flap bending moment measurement. These previous studies gave the key suggestion that in applications of their methodologies, at least the first three modes in addition to the rigid body mode should be employed for accurate estimation of spanwise airloads distribution.

Recent work has involved the growth of accurate computational modeling of a helicopter rotor for estimating rotor loads. Öry and Lindert [54] introduced a methodology of reconstructing applied forces to rotor blades by inversely solving the equations of motion in modal space, based on flight test data on Kamov-26 and Hughes 500E. Wang et al. [7] used a lifting-line aerodynamic model to derive spanwise aerodynamic force distribution on a rotor blade based on strain data measured at a few points. In these studies, the required modal parameters were obtained from the finite element modeling of the rotor blade. Apart from the modal expansion approaches, ShouShen et al. [55] developed a force analysis methodology, called Inverse Transfer Matrix Method, to deal with the inherent issues with modal analysis (i.e., ill-posed problems must be solved to obtain generalized modal coordinates). The methodology was verified using the response data obtained during the NASA/Army UH-60A Airloads Program. Schrage et al. [56] also applied the Inverse Transfer Matrix Method to the blade out-of-plane and in-plane moments measured by a large number of on-blade sensors, in order to determine the rotor loads on the

YAMAHA R-50/RMAX UAV testbeds. Although the proposed methods and processes in these studies were verified and have been shown to be useful in practice, accurate computational models of the rotor, such as a finite element model for the structure, aerodynamic model, and inflow distribution model, were required to obtain the necessary information for loads estimation.

From these studies, it appears that the framework of estimating rotor loads has been well defined, however, the previous studies have some drawbacks associated with their rotor loads identification approaches, such as: an excessive amount of measured quantities (bending moment, displacement, slope at blade root, and strain of the structure), or precise computational modeling of the rotor. Thus, the approach presented in this dissertation makes use of the basic theoretical framework of the modal expansion techniques as presented in the literature, and integrates the load estimation methodology with the DIC deformation measurement technique and the OMA algorithms.

1.3 Present approach

The primary goal of this study is to develop a theoretical and experimental methodology for estimating helicopter rotor loads based on measurements of blade structural response. The present approach consists of three steps: (i) The continuous deformation time history of a reduced-scale rotor blade is measured using the DIC technique. (ii) The measured blade deformation is processed with several OMA algorithms, i.e., Natural Excitation Technique (NExT), Eigensystem Realization Algorithm (ERA), and Complexity

Pursuit (CP), in order to identify modal frequencies and mode shapes in the rotating frame. (iii) The rotor loads including the structural and aerodynamic forces are identified based on the measured blade deformations and the modal parameters obtained in the previous two steps. This combined DIC-OMA approach would yield a simple and inexpensive strategy to estimate rotor loads without using on-blade sensors and detailed computational models of the rotor. It is especially valuable because the challenging and costly problem of performing accurate surface pressure measurements could be avoided.

First, the combined DIC-OMA approach is applied to a 0.46 m-diameter, two-bladed, extremely flexible rotor for verification of the proposed methodology. The time history of the extremely flexible rotor blade deformation in hover is measured using the DIC technique, and the measured responses are processed with the NExT, ERA, and CP algorithms. The experimental results are compared and correlated to an aeroelastic numerical prediction, developed by Sicard [9].

The approach is then extended to measurements on a larger-scale (2 m-diameter), single-bladed, coaxial counter-rotating (CCR) rotor system. The measured blade deformation employing the DIC and the identified modal parameters are compared to numerical analysis, provided from Ref. [57].

Finally, the rotor loads estimation methodology is applied to the blade response of a 2 m-diameter, two-bladed, isolated single rotor in hover. Three different rotor operating conditions are tested: (1) steady-state, constant loading at certain rotor thrust level (collective pitch input), (2) periodic loading at

once-per-revolution frequency (cosine cyclic pitch input), and (3) step change in rotor blade pitch angle (step function collective pitch input). Hub load (rotor thrust) is then reconstructed from numerical integration of the estimated spanwise lift distribution along the blade quarter-chord axis, and is compared to the time history of rotor thrust directly measured by a load cell installed on the rotor hub.

1.4 Contribution of the Current Research

There are three major contributions of the present work:

1. Development of an experimental methodology to measure the continuous time history of helicopter rotor blade deformation over the entire blade span including flap, lead-lag, and torsional bending degrees of freedom, with minimum preparation of the test specimen (i.e., painting the surface of the structure).

2. Identification of rotating frame natural frequencies and mode shapes of a rotor blade in its operating condition without using conventional on-blade sensors.

3. Estimation of helicopter rotor loads using only measured structural response, resulting in significant reduction of time and cost for measurement.

1.5 Organization of the Dissertation

Chapter 1 describes the importance of understanding the nature of helicopter rotor loads, and the limitation of current experimental and theoretical tools for rotor loads estimation. The new approach in the present study to overcome these limitations is proposed and the key components of the approach are described. The literature review provides the state-of-the-art in each key component of the present approach. Additionally, experimental setups and procedures for verification of the proposed approach are introduced and briefly explained.

Chapter 2 presents the theoretical development and formulation of the current approach for estimating rotor loads based on blade structural response. This chapter covers the fundamentals of the non-contact optical blade deformation measurement technique (digital image correlation), operational modal analysis (NExT, ERA, and CP), and rotor loads estimation methodology used in the dissertation.

Chapter 3 documents the details of three experimental setups and procedures used in the present study. The setups include: (i) a 0.46 m-diameter, two-bladed, extremely flexible single rotor hover test stand, (ii) a 2 m-diameter, single-bladed, coaxial counter-rotating (CCR) rotor hover test stand, and (iii) a 2 m-diameter, two-bladed, isolated single rotor hover test stand. This chapter also explains the arrangement of the digital image correlation measurement for each rotor test bed.

Chapter 4 discusses the results of the DIC blade deformation measurement, modal parameter identification, and rotor loads estimation of each experimental system. Note that the setups (i) and (ii) are used for verifying the applicability and robustness of the combined DIC-OMA approach, while the setup (iii) is used for verifying the entire process of the current methodology, including the DIC, the OMA, and rotor loads estimation. These individual measurements on the three different rotor configurations and operating conditions examine whether the methodology proposed in this dissertation is a general tool for helicopter rotor loads estimation.

Chapter 5 summarizes the key conclusions of the present research, and provides several suggestions for future directions of study.

Chapter 2

Theoretical Development

This chapter is divided into three sections, each corresponding to the theoretical development of three key components (DIC, OMA, and rotor loads estimation methodology) of the present study. The basic concept of the DIC is introduced and explained in § 2.1. The mathematical frameworks of the three OMA algorithms (NExT, ERA, and CP) are presented in § 2.2. The rotor loads estimation methodology based on the modal expansion technique is described in § 2.3.

2.1 Digital Image Correlation

Digital Image Correlation (DIC) begins with comparing digital images of a structure taken at different stages of deformation. By tracking subsets of pixels, the DIC processing algorithm can compute surface displacement and reconstruct full field 2D or 3D deformation vector fields and strain maps. This section first defines the blade coordinate system used in the study, then explains the basic principles of 2D and 3D DIC technique.

2.1.1 Blade coordinate system

The deformed position of the rotor blade is described using the blade-fixed coordinate system, shown in Fig. 2.1. The origin of the coordinate system is fixed at the center of rotation (center of the rotor hub), and the coordinate system rotates about the positive z-axis at a constant rotational speed of Ω. The x-axis is along the quarter-chord axis of the undeformed rotor blade. Additionally, three degrees of freedom are used in the study: out-of-plane (flapwise) motion, in-plane (lead-lag) motion, and torsional (feathering) motion with respect to the hub plane under the action of changing aerodynamic lift and drag forces. Blade deformation measured using the DIC technique shown in chapter 4 follows this definition of the blade-fixed coordinate system.

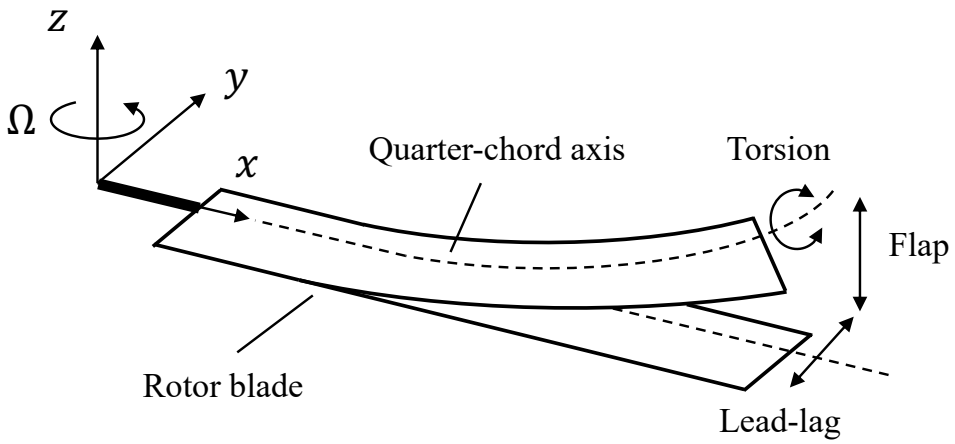

Figure 2.1: Blade coordinate system

2.1.2 2D DIC

The basic procedure of the 2D DIC deformation measurement is as follows:

1. Random speckle patterns are applied onto a surface of the target structure.

2. Camera calibration is performed to compute a mapping function between global coordinates and camera image plane coordinates.

3. A sequence of digital images of the surface of the target structure is obtained by digital cameras, such as CMOS or CCD cameras, before, during, and after deformation.

4. The full image is divided into a set of small interrogation windows (also called subsets) with an area of multiple pixels such as 16×16 pixels.

5. Light intensity distribution inside each interrogation window is computed.

6. The algorithm searches for an area of same light intensity distribution in the image before and after deformation using 2D image correlation.

7. Once the location of the target interrogation window is found in the deformed image, a 2D displacement vector corresponding to the motion of the window is computed, and the search-and-compute process is repeated for all the interrogation windows on each image.

To search for the same subset match in the reference and deformed image (Step. 6 and 7 in the procedure), the normalized cross-correlation function $C(x_0, y_0, x_1, y_1)$ is computed as follows:

$$C(x_0, y_0, x_1, y_1) = \frac{\sum F(x_0, y_0) G(x_1, y_1)}{\sqrt{\sum F(x_0, y_0)^2 G(x_1, y_1)^2}} \tag{2.1}$$

where $F(x_0, y_0)$ and $G(x_1, y_1)$ represent the light intensity (values of gray levels of the pixels) inside the area of the subset from the undeformed and deformed images, respectively. (x_0, y_0) and (x_1, y_1) are the coordinates of a central point on the target subset before and after deformation, respectively. Figure 2.2 shows a schematic of the subset search process.

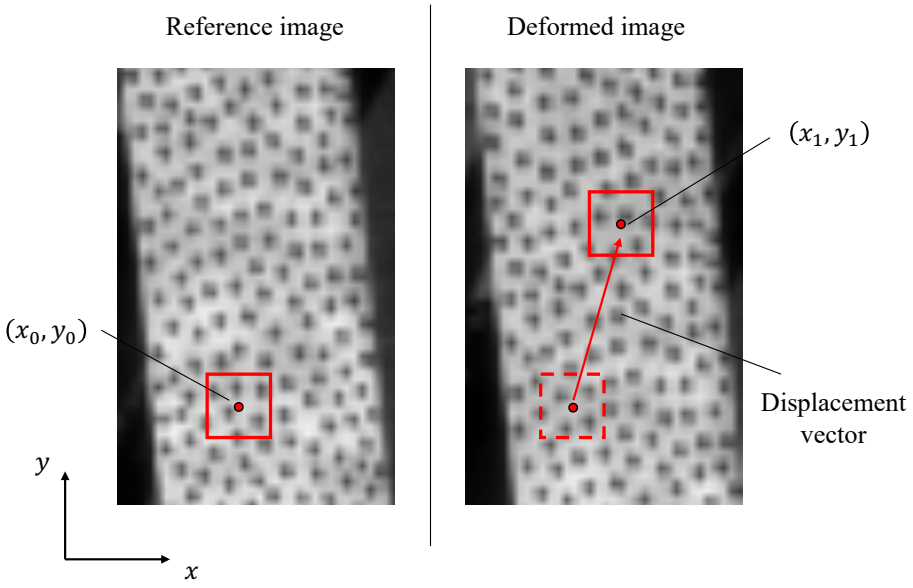

Figure 2.2: A schematic of subset search process

Essentially, displacement computations are treated as an optimization problem, that is, the displacement vector is calculated by searching a set of the coordinates (x_1, y_1) after deformation, that maximizes the cross-correlation function $C(x_0, y_0, x_1, y_1)$. That is the reason why this technique is called digital image correlation. Details of the mathematical development of 2D DIC are available in Ref. [58].

2.1.3 3D DIC

3D DIC generally uses multiple digital cameras and arranges their relative positions in a stereoscopic manner, taking images of a target structure from different perspectives. A commercially available software LaVision DaVis 8.4.0 [59] is used for camera control and calibration, image acquisition, and DIC processing.

First, a physical point in global coordinates (laboratory coordinates, (x, y, z)) is mapped onto the image plane of cameras 1 and 2, as shown in Fig. 2.3. The mapping functions $M_1(x, y, z)$ and $M_2(x, y, z)$ are defined during the camera calibration process as is the case of 2D DIC. Then the corresponding point in image coordinates of camera 1 before and after deformation are searched by solving the optimization problem with the cross-correlation function using Eq. 2.1, and a 2D displacement vector 1 is computed. The same procedure is repeated for the corresponding image from camera 2, and a 2D displacement vector 2 is computed. With the help of the surface height distribution $H(x, y)$ and the two mapping functions $M_1(x, y, z)$ and $M_2(x, y, z)$,

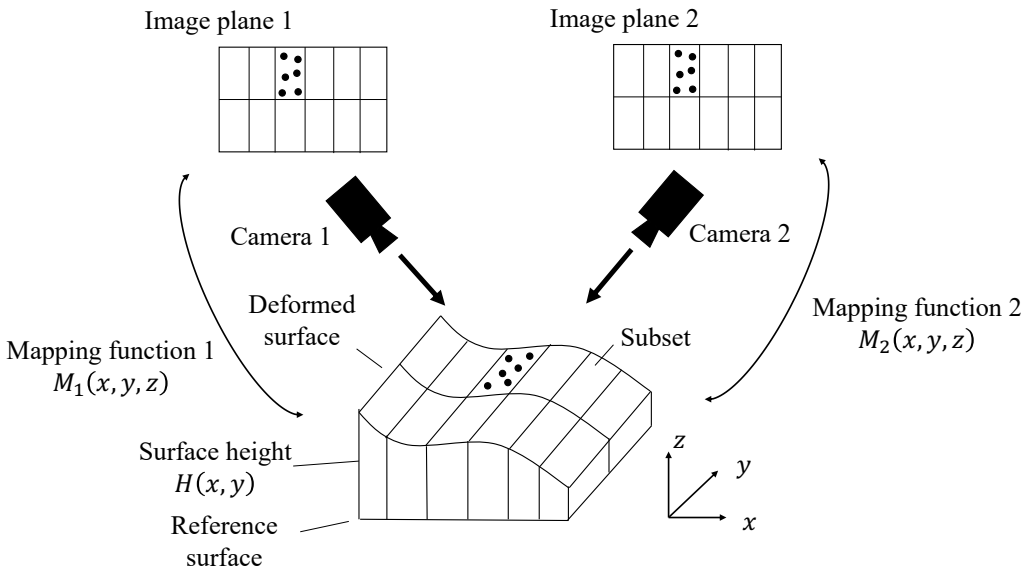

Figure 2.3: A schematic of the basic 3D DIC principle

the two 2D displacement vectors are combined to a 3D displacement vector, as shown in Fig. 2.4. Since there are a large number of experiment-specific parameters for the DIC deformation measurement, details of its setting, such as lens magnification, aperture, light source, size of subset, camera resolution, and camera mount arrangement, will be described in chapter 3.

2.2 Operational Modal Analysis

This section describes the theoretical framework of the two Operational Modal Analysis (OMA) algorithms used in the dissertation: Natural Excitation Technique & Eigensystem Realization Algorithm (NExT-ERA) and Complexity Pursuit (CP).

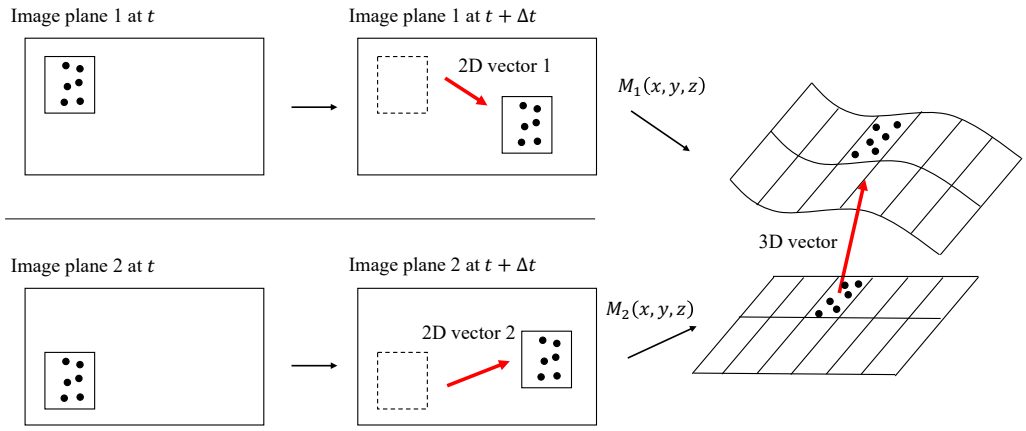

Figure 2.4: A calculation scheme of the 3D displacement vector

2.2.1 NExT-ERA

Since NExT is in general employed together with a time domain modal identification scheme such as ERA, an overview of the technique is presented here as the NExT-ERA combined approach.

The first step of NExT-ERA analysis is to compute cross-correlation functions based on measured structural response. The correlation functions can be expressed as summation of exponentially decaying sinusoidal signals and each signal consists of a damped natural frequency and damping ratio, that is equivalent to that of an associated structural mode. These cross-correlation functions are thus used as pseudo-impulse response functions and processed by ERA for extraction of modal properties.

Consider the differential equation of motion for a multi-degree-of-freedom

structure

$$\mathbf{M}\ddot{\mathbf{x}}(t) + \mathbf{C}\dot{\mathbf{x}}(t) + \mathbf{K}\mathbf{x}(t) = \mathbf{f}(t) \tag{2.2}$$

where $\mathbf{M}$, $\mathbf{C}$, and $\mathbf{K}$ are the mass, damping, and stiffness matrices respectively, $\mathbf{f}(t)$ is the force vector, and $\ddot{\mathbf{x}}(\mathbf{t})$, $\dot{\mathbf{x}}(t)$, and $\mathbf{x}(t)$ are the acceleration, velocity, and displacement vectors at time t. Assuming that the system is excited by a white noise, Eq. 2.2 can be written as:

$$\mathbf{M}\ddot{\mathbf{X}}(t) + \mathbf{C}\dot{\mathbf{X}}(t) + \mathbf{K}\mathbf{X}(t) = \mathbf{F}(t) \tag{2.3}$$

where $\mathbf{X}(t)$ is the random response vector and $\mathbf{F}(t)$ is the random excitation vector. Then multiplying Eq. 2.3 by a reference scalar random response vector $X_i(s)$ at a location i and time s on the system yields

$$\mathbf{M}\ddot{\mathbf{X}}(t)X_i(s) + \mathbf{C}\dot{\mathbf{X}}(t)X_i(s) + \mathbf{K}\mathbf{X}(t)X_i(s) = \mathbf{F}(t)X_i(s) \tag{2.4}$$

Taking the expected value of Eq. 2.4 results in

$$\mathbf{M}E[\ddot{\mathbf{X}}(t)X_i(s)] + \mathbf{C}E[\dot{\mathbf{X}}(t)X_i(s)] + \mathbf{K}E[\mathbf{X}(t)X_i(s)] = E[\mathbf{F}(t)X_i(s)] \tag{2.5}$$

where E is the expectation operator. Using R as the cross-correlation function operator and $\tau = t - s$ as the time separation between t and s, Eq. 2.5 can be expressed as:

$$\mathbf{M}\mathbf{R}_{\ddot{\mathbf{X}}X_i}(\tau) + \mathbf{C}\mathbf{R}_{\dot{\mathbf{X}}X_i}(\tau) + \mathbf{K}\mathbf{R}_{\mathbf{X}X_i}(\tau) = \mathbf{R}_{\mathbf{F}X_i}(\tau) \tag{2.6}$$

The following relationship holds according to Caicedo et al. [60]:

$$R_{\dot{x}_i x_j}(\tau) = \dot{R}_{x_i x_j}(\tau) \tag{2.7}$$

$$R_{x_i^{(m)}x_j}(\tau) = R^{(m)}_{x_i x_j}(\tau) \tag{2.8}$$

where $x_i(t)$ and $x_j(t)$ are random response vectors at two different locations i and j, and $x_i^{(m)}$ is the mth derivative of $x_i(t)$ with respect to time, and $R^{(m)}_{x_i x_j}(\tau)$ denotes the mth derivative of the cross-correlation function $R_{x_i x_j}(\tau)$ with respect to τ.

With the assumption that the responses of the system are uncorrelated to the random excitation $\mathbf{F}(t)$, Eq. 2.6 can now be expressed as

$$\mathbf{M}\ddot{\mathbf{R}}_{\mathbf{X}X_i}(\tau) + \mathbf{C}\dot{\mathbf{R}}_{\mathbf{X}X_i}(\tau) + \mathbf{K}\mathbf{R}_{\mathbf{X}X_i}(\tau) = 0 \tag{2.9}$$

In Eq. 2.9, it is obvious that the cross-correlation function $\mathbf{R}_{\mathbf{X}X_i}(\tau)$ satisfies the homogenous differential equation of motion. As described by James et al. [41], the cross-correlation function is equivalent to a sum of decaying sinusoids of the same form as the impulse response of the original structure in time domain. This cross-correlation function obtained with the NExT analysis is used as an input to ERA process.

Computing cross-correlation functions is the key step of the NExT algorithm. Based on the fact that the cross-spectral density (frequency domain) is equivalent to the cross-correlation function (time domain), $R_{x_i x_j}(\tau)$ can be calculated using the inverse Fourier transform of the cross-spectral density of $x_i(t)$ and $x_j(t)$ as described in Ref. [61]. First, the responses $x_i(t)$ and $x_j(t)$ are divided into data blocks, possibly with overlapping. The cross-spectral density function is then computed with ensemble averaging and Hanning window

of the Fourier Transform of each data block in order to improve the accuracy of the computation. Then the cross-correlation function between the two channels i and j is obtained using

$$R_{x_i x_j}(n) = \frac{1}{N} \sum_{k=0}^{N-1} S_{x_i x_j}(k) exp\left(i \frac{2\pi k n}{N}\right), \quad n = 0, \ldots, N-1 \tag{2.10}$$

where k and n represent indices in frequency and time domain, respectively, and $S_{x_i x_j}(k)$ is the discrete cross-spectral density function between the two channels i and j.

It should be noted that the assumption made for the theoretical development, i.e., the white noise excitation is uncorrelated, is not necessarily met for modal analysis on a real structure. Nevertheless, the operational modal analysis with NExT has been performed successfully on real structures in past studies [41, 62, 63] without satisfying the assumption, i.e. the excitation to the structure is not a white noise; it is typically bandwidth limited and does not have equal power at all frequencies. For appropriate use of this method, it is essential for an analyst to determine the number of samples used for the algorithm, the number of data blocks, the number of overlapping data points, the length of the data blocks, shape of window, and reference channels for calculating cross-correlation functions. These are all typically determined by trial-and-error.

For the formulation of ERA, consider the state-space equations in continuous time

$$\begin{aligned} \dot{\mathbf{x}}(t) &= \mathbf{A}_c \mathbf{x}(t) + \mathbf{B}\mathbf{u}(t) \\ \mathbf{y}(t) &= \mathbf{C}\mathbf{x}(t) \end{aligned} \tag{2.11}$$

where $\mathbf{x}(t)$ is the state vector, $\mathbf{u}(t)$ is the excitation vector, $\mathbf{y}(t)$ is the response vector to the excitation, and $\mathbf{A}_c$, $\mathbf{B}$, and $\mathbf{C}$ are state-space matrices in continuous time. Assuming that an impulse excitation is applied to the dynamic system, a solution to these equations has the form

$$\mathbf{Y}(t) = \mathbf{C}e^{\mathbf{A}_c t}\mathbf{B} \tag{2.12}$$

where $\mathbf{Y}(t)$ consists of the free responses of the system to an impulse excitation. In discrete time, the solution is represented as

$$\mathbf{Y}(n) = \mathbf{C}\mathbf{A}^{n-1}\mathbf{B} \tag{2.13}$$

where $\mathbf{Y}(n)$ is the response at the n^{th} time step, $\mathbf{A} = e^{A_c \Delta t}$ is the discrete-time state transition matrix and Δt is the time step of system discretization. The goal of ERA is to estimate the constant matrices $\mathbf{A}$, $\mathbf{B}$, and $\mathbf{C}$ from the impulse response data $\mathbf{Y}(n)$ acquired from measurement. The system modal parameters are then computed from the eigenvalues and eigenvectors of the constructed state matrices. Note that the $\mathbf{y}(t)$ vector is the output of the NExT algorithm that yields pseudo-impulse responses from the measured structural deformation. It is important to mention that the matrices $\mathbf{B}$ cannot be estimated for the present modal identification since the NExT is an output-only modal analysis technique and the real excitation to the structure is unknown. However, the modal parameters are obtained from the matrices $\mathbf{A}$ and $\mathbf{C}$.

System realization starts from building the generalized Hankel matrix:

$$\mathbf{H}(n-1) = \begin{bmatrix} \mathbf{Y}(n) & \mathbf{Y}(n+1) & \dots & \mathbf{Y}(n+p) \\ \mathbf{Y}(n+1) & \ddots & & \vdots \\ \vdots & & & \\ \mathbf{Y}(n+q) & \dots & & \mathbf{Y}(n+p+q) \end{bmatrix} \tag{2.14}$$

where $\mathbf{Y}(n)$ is in this case the $N \times 1$ vector which consists of the pseudo-impulse responses computed by NExT at the n^{th} time step, and N is the number of channels corresponding to the number of interrogation windows during DIC processing. The parameters p and q correspond to the size of the Hankel matrix. As a rule of thumb for selecting p and q, the analyst should consider ten times the number of expected modes for the number of columns p, and twice to three times the number of columns p for the number of rows q in the Hankel matrix. Normally, the Hankel matrix is formed with block rows and block columns data shifted in time by one sample from the previous block row and column.

The Hankel matrix for $n = 1$ can be decomposed by using the singular value decomposition as

$$\mathbf{H}(0) = \begin{bmatrix} \mathbf{CB} & \mathbf{CAB} & \dots & \mathbf{CA}^{p-1}\mathbf{B} \\ \mathbf{CAB} & \ddots & & \vdots \\ \vdots & & & \\ \mathbf{CA}^{q-1}\mathbf{B} & \dots & & \mathbf{CA}^{p-1+q-1}\mathbf{B} \end{bmatrix} = \mathbf{R} \sum \mathbf{S}^T. \tag{2.15}$$

Then the n^{th} order system realization is calculated as

$$\begin{aligned} \mathbf{A} &= \textstyle\sum_n^{1/2} \mathbf{R}_n^{1/2}\, \mathbf{H}(1)\, \mathbf{S}_n \sum_n^{-1/2} \\ \mathbf{C} &= \mathbf{E}^T\, \mathbf{R}_n \sum_n^{1/2} \end{aligned} \tag{2.16}$$

where $\mathbf{H}(1)$ is the Hankel matrix for $n = 2$ and $\mathbf{E} = [\mathbf{I} \;\; \mathbf{O}]$ with an identity matrix $\mathbf{I}$ and a null matrix $\mathbf{O}$ of appropriate order. These matrices are then

transformed to modal coordinates by multiplying with the eigenvector matrix of $\mathbf{A}$

$$\begin{aligned} \mathbf{\Lambda} &= \mathbf{\Psi}^{-1}\mathbf{A}\mathbf{\Psi} \\ \mathbf{C}_m &= \mathbf{C}\mathbf{\Psi} \end{aligned} \tag{2.17}$$

where $\mathbf{\Lambda}$ is the diagonal matrix of eigenvalues of $\mathbf{A}$ and $\mathbf{\Psi}$ is the matrix of eigenvectors of $\mathbf{A}$. After transforming back to the continuous time domain, one can obtain the modal damping ratios and damped natural frequencies of the system from the real and imaginary parts of the eigenvalues, respectively. The column vectors of $\mathbf{C}_m$ correspond to the mode shapes.

However, there are a number of parameters that an analyst needs to determine for identifying true physical modal parameters for the use of NExT-ERA. This drawback provides motivation for using another OMA algorithm, Complexity Pursuit, which will be described in the following section. Further details and theoretical background of NExT and ERA can be found in Refs. [38, 41].

2.2.2 Complexity Pursuit

The Complexity Pursuit (CP) algorithm is classified under the family of Blind Source Separation (BSS) algorithms. Consider the differential equation of motion for a multi-degree-of-freedom structure with mass matrix $\mathbf{M}$, damping matrix $\mathbf{C}$, and stiffness matrix $\mathbf{K}$

$$\mathbf{M}\ddot{\mathbf{x}}(t) + \mathbf{C}\dot{\mathbf{x}}(t) + \mathbf{K}\mathbf{x}(t) = \mathbf{F}(t) \tag{2.18}$$

where $\mathbf{F}(t)$ is the force vector and $\ddot{\mathbf{x}}(t)$, $\dot{\mathbf{x}}(t)$, and $\mathbf{x}(t)$ are the acceleration, velocity, and displacement vectors at time t. The modal transformation can be expressed as

$$\mathbf{x}(t) = \boldsymbol{\Phi}\boldsymbol{\eta}(t) \tag{2.19}$$

where $\boldsymbol{\Phi}$ and $\boldsymbol{\eta}$ are the modal matrix and modal coordinate vector of the system, respectively. Note that the modes of a system form, by definition, a linearly independent set of basis vectors [64]. Let us introduce the general concept of BSS in mathematical form as

$$\mathbf{y}(t) = \mathbf{x}(t) + \mathbf{n}(t) = \mathbf{A}\ \mathbf{s}(t) + \mathbf{n}(t) \tag{2.20}$$

where $\mathbf{y}(t)$ is the measured displacement vector at time t, $\mathbf{n}(t)$ is a noise vector, $\mathbf{s}(t)$ is the source vector, and $\mathbf{A}$, often called "mixing" matrix, is a transfer matrix between sensors and sources. As shown in Eq. 2.20, the usage of BSS within the context of operational modal analysis is to estimate the mixing matrix $\mathbf{A}$ and the source vector $\mathbf{s}$ from the measured output responses $\mathbf{y}(t)$, and interpret them as the modal matrix $\boldsymbol{\Phi}$ and modal coordinates $\boldsymbol{\eta}$ of the structural system.

This methodology can significantly simplify the multi-degree-of-freedom modal parameter identification due to the fact that each separated source ideally represents the equivalent single-degree-of-freedom response, whose frequency and damping ratio are associated with each structural mode. Mode shapes are represented by columns of the mixing matrix $\mathbf{A}$. It should be noted that the dimension of the estimated modal matrix is $N \times N$, where N is the

number of measurement points, meaning that BSS separates the measured data into N different source signals. A number of techniques falling under the broad spectrum of BSS can be found in the literature. These techniques share the fact that a priori information about the sources or the input forcing is not required.

The CP algorithm separates source signals by using a measure of signal complexity called temporal predictability. The temporal predictability of a signal describes how well one can predict the value of a signal at the next time step, knowing only the values of the signal at the previous time steps. The algorithm is based on the theorem that the temporal predictability of a mixture of source signals is lower than that of each contained source signal, i.e., each source signal, or mode, is less complex than the measured signal, or superposition of modes. Therefore, the algorithm tries to find the mixing matrix $\mathbf{A}$ of the system, so that the temporal predictability of each resulting source is as high as possible, which basically reduces to an optimization problem. Details on this method are well summarized in the literature [50]; a brief overview is given here.

The temporal predictability $G(y_i)$ of a signal is given by

$$G(y_i) = \log \frac{\sum_{j=1}^{N} [y_i(t_j) - \overline{y}_i(t_j)]^2}{\sum_{j=1}^{N} [y_i(t_j) - \hat{y}_i(t_j)]^2} \tag{2.21}$$

with y_i being a signal at i th measurement location with N time entries, and $\bar{y}_i$ and $\hat{y}_i$ being the long-term and short-term predictors respectively; these are

expressed as weighted sums of signal values measured up to time t_{j-1} given by

$$\overline{y}_i(t_j) = \lambda_L \overline{y}_i(t_{j-1}) + (1-\lambda_L) y_i(t_{j-1}), \qquad 0 < \lambda_L < 1 \tag{2.22}$$

$$\hat{y}_i(t_j) = \lambda_S \hat{y}_i(t_{j-1}) + (1-\lambda_S) y_i(t_{j-1}), \qquad 0 < \lambda_S < 1 \tag{2.23}$$

Values of $\lambda_L = 0.99$ and $\lambda_S = 0.5$ are used in this study. Minimization of the function $G(y_i)$ leads to an eigenvalue problem that yields the columns $\mathbf{A}_i$ of the mixing matrix and corresponding eigenvalues $\mathbf{\Lambda}_i$ as follows:

$$\hat{\mathbf{C}}^{-1}\bar{\mathbf{C}}\mathbf{A}_i = \mathbf{\Lambda}_i \mathbf{A}_i \tag{2.24}$$

where $\hat{\mathbf{C}}$ and $\bar{\mathbf{C}}$ are the short-term and long-term covariance matrices respectively, calculated by:

$$\begin{aligned} \hat{\mathbf{C}} &= \sum_{j=1}^{N} (\mathbf{y}(t_j) - \hat{\mathbf{y}}(t_j))(\mathbf{y}(t_j) - \hat{\mathbf{y}}(t_j))^T \\ \bar{\mathbf{C}} &= \sum_{j=1}^{N} (\mathbf{y}(t_j) - \bar{\mathbf{y}}(t_j))(\mathbf{y}(t_j) - \bar{\mathbf{y}}(t_j))^T \end{aligned} \tag{2.25}$$

The biggest advantage of the CP algorithm is ease of implementation; only two parameters λ_L and λ_S need to be chosen and the algorithm is robust to the choice of these parameters, in contrast to the NExT-ERA approach. The primary differences are summarized in the flow chart shown in Fig. 2.5.

Thus, this present study selected the CP algorithm as a primary scheme to extract rotating-frame modal properties of a rotor blade.

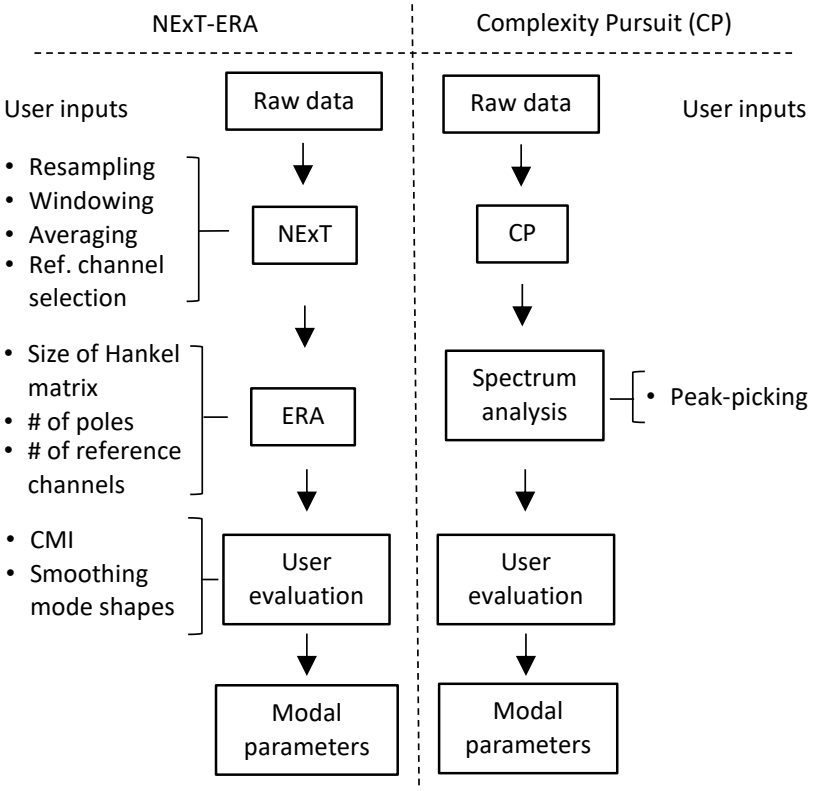

Figure 2.5: Flow chart of the OMA algorithms

2.3 Rotor loads estimation

Rotor loads estimation mainly consists of two components: one is the estimation of distributed forces along the rotor blade span and the other is the estimation of integrated loads acting at the rotor hub. Each component has inertial and aerodynamic terms. This study focuses on the estimation of

out-of-plane rotor loads.

The vertical hub reaction force, which is essentially the rotor thrust, is the net shear at the root of the rotating blade and is theoretically obtained by integrating the sectional inertial and aerodynamic forces on the blade. Considering a rigid blade with no hinge offset as shown in Fig. 2.6, the vertical shear S_z at the blade root is expressed as

$$S_z = \int_0^R F_z \, dr - \int_0^R m\ddot{z} \, dr \tag{2.26}$$

where R is the blade radius, F_z is the sectional aerodynamic force, m is the mass per unit length, and $\ddot{z}$ is the transverse (out-of-plane) acceleration. Equation 2.26 is applicable to either articulated or hingeless rotors, since the z axis is always aligned to the rotational axis of the rotor.

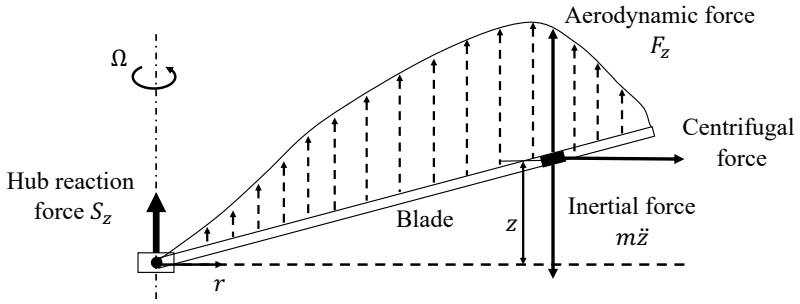

Figure 2.6: Diagram of rotor blade forces

2.3.1 Inertial loads

Let us first consider the estimation of the inertial loads distributed along the rotor blade. The inertial force is expressed in the second term

of Eq. 2.26. The transverse acceleration $\ddot{z}$ can be obtained by numerically differentiating measured out-of-plane displacements z in space, since the DIC technique measures three-dimensional, full-field, time-resolved deformation of the blade structure. With the mass properties of rotor blades calculated from a CAD model, one can compute the distributed inertial forces on the blade as a function of time (azimuthal angle) and space (radial location).

However, it is known that numerical differentiation of measured data severely amplifies measurement noise. Thus, it is quite important to apply smoothing methods to measured data in advance of numerical differentiation, in order to accurately compute inertial loads. There are a number of methodologies available in the literature for measurement data smoothing, each with advantages and disadvantages. The first methodology tested in the present study is the method of data smoothing and numerical differentiation by a regularization approach. In particular, the problem statement in this study falls into the class of Tikhonov regularization problems [65]. The general concept of regularization is as follows:

Provided a set of data $y(x_i)$, where $i = 1, 2, ...N$, the regularization method defines an objective function Q;

$$Q(\hat{y}) = \int_{x_1}^{x_N} \left|\hat{y}(x) - y(x)\right|^2 \, dx + \lambda \int_{x_1}^{x_N} \left|\frac{d^2\hat{y}}{dx^2}\right|^2 \, dx \tag{2.27}$$

where $y(x)$ is a continuous function that exactly describes the given data trend. The first term of the equation above is to quantify the goodness of fit of a "smooth" function $\hat{y}(x)$ to the trend $y(x)$, whereas the second term of

the equation is to determine the "roughness" of $\hat{y}(x)$. The second derivative of $\hat{y}(x)$ corresponds to the curvature of the function. Since large curvature of a function means that the function changes rapidly, constraining the term to be small makes the desired curve smooth. The goal of the regularization is to find a function $\hat{y}(x)$ such that the objective function $Q(\hat{y})$ is minimized with a weighting factor λ. Further details of the mathematical development as well as several methods for selecting an appropriate value of λ can be found in Ref. [66].

To evaluate the applicability to rotor blade deformation measured using DIC, the regularization algorithm was applied to the out-of-plane bending deformation of a 2 m-diameter rotor blade spun at 900 RPM. Figure 2.7 compares the unprocessed and regularized flapwise bending deformation extracted from the quarter-chord axis of the rotor blade at a certain time instant. The unprocessed deformation showed an unusual dip at regions of the blade tip, possibly due to the fact that the significant blade deformation at the tip introduced out-of-focus blur and poor DIC processing quality in raw digital images. This non-physical trend must be smoothed out before numerical differentiation is performed. However, the regularization process with two different weighting factors λ could not either remove the dip in Fig. 2.7a, or preserve the tip deflection in Fig. 2.7b.

Alternately, polynomial curve fitting was applied to the same set of data used for the regularization processing. As shown in Fig. 2.8, the large dip was eliminated and the blade tip deflection was well preserved. Based

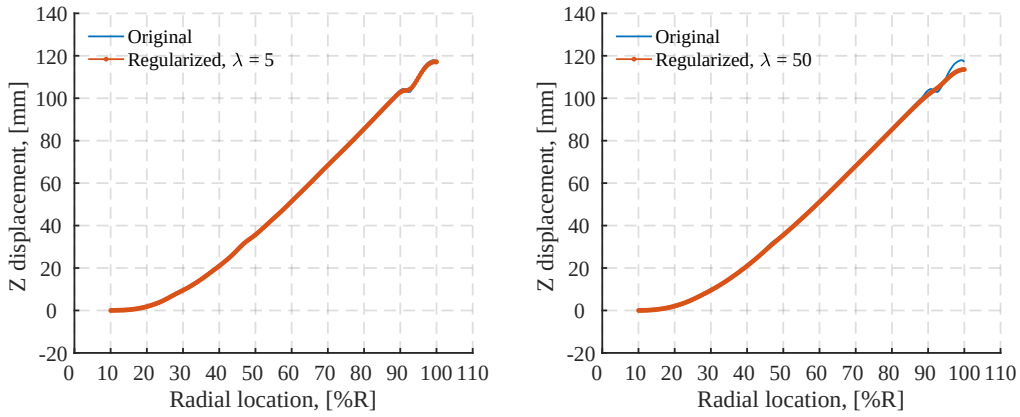

(a) $\lambda = 5$ (b) $\lambda = 50$

Figure 2.7: Unprocessed and regularized flapwise blade deformation

on this result, a 3rd-order polynomial curve fit was selected to smoothen the deformation measured by DIC in this dissertation. Note that the inertial properties of a rotor blade used in this study are known from an accurate CAD model, and its details are described in chapter 3.

2.3.2 Aerodynamic loads

The spanwise distribution of airloads along the rotor blade is estimated using a formulation in modal space [67]. The present approach makes use of modal parameters identified using the CP algorithm. The partial differential equation of motion for the out-of-plane bending of a rotating rotor blade is represented as

$$\frac{\partial^2}{\partial r^2}\left(EI\frac{\partial^2 z}{\partial r^2}\right) - \frac{\partial}{\partial r}\left[\int_r^R m\Omega^2\rho d\rho\frac{\partial z}{\partial r}\right] + m\ddot{z} = F_z \tag{2.28}$$

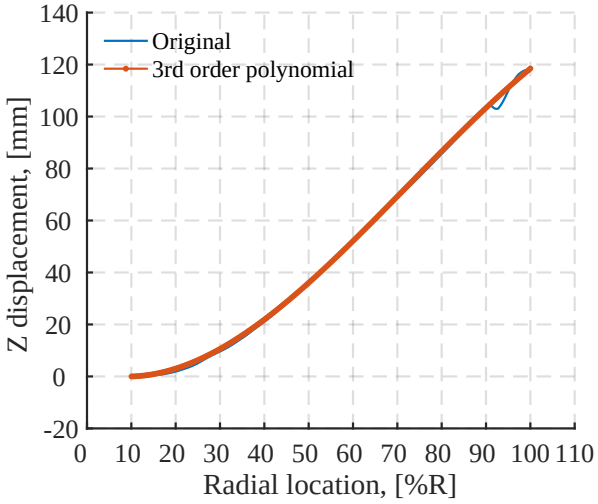

Figure 2.8: Measured flapwise blade deformation and 3rd-order polynomial curve fit

where E is the modulus of elasticity of the blade section, I is the area moment about the chordwise principal axis, and Ω is the rotational speed. Now consider the free vibration of the rotating rotor blade at frequency ν. The solution for the homogeneous partial differential equation can be written as

$$z = \eta(r)e^{i\nu t} \tag{2.29}$$

Substituting Eq. 2.29 to 2.28 and making the right hand side of Eq. 2.28 zero, the result is

$$\frac{d^2}{dr^2}\left(EI\frac{d^2\eta}{dr^2}\right) - \frac{d}{dr}\left[\int_r^R m\Omega^2\rho d\rho\frac{d\eta}{dr}\right] - \nu^2 m\eta = 0 \tag{2.30}$$

which can be viewed as the equation for vibration in a vacuum. This modal equation yields an eigenvalue problem for the natural frequency ν and mode shape $\eta(r)$ and there exists a series of eigensolutions $\eta_k(r)$ and corresponding

eigenvalues ν_k of the k-th mode. The out-of-plane deflection $z(r,t)$ is thus expanded as a series of mode shapes describing the spanwise deformation as

$$z(r,t) = \sum_{k=1}^{\infty} \eta_k(r) q_k(t) \tag{2.31}$$

where $\eta_k(r)$ and $q_k(t)$ correspond to the k th mode shape and modal coordinate of the rotating rotor blade, respectively. Substituting Eq. 2.31 into 2.28 yields

$$\sum_k \left(\frac{d^2}{dr^2}\left(EI \frac{d^2\eta_k}{dr^2} \right) - \frac{d}{dr}\left[\int_r^R m\Omega^2 \rho d\rho \frac{d\eta_k}{dr} \right] \right) q_k + \sum_k m\eta_k \ddot{q}_k = F_z \tag{2.32}$$

The terms in the first summation in Eq. 2.32 can be replaced by Eq. 2.30, yielding

$$\sum_k (\nu_k^2 m\eta_k q_k + m\eta_k \ddot{q}_k) = F_z. \tag{2.33}$$

Thus, if the modal parameters (i.e., natural frequencies ν_k, mode shapes η_k, and modal coordinates q_k, $\ddot{q_k}$) are known, one can compute the distributed aerodynamic force F_z along the rotor blade from Eq. 2.33. This modal approach discussed above is practical if one is considering the fact that a small number of modes are typically needed to represent the flapwise dynamics of the rotating rotor blade [67]. With the distributed loads identified, rotor hub loads can be obtained by integrating the radial distribution of both structural and aerodynamic forces along the blade span, based on Eq. 2.26. For verification of the present methodology, the estimated hub loads are compared to the results of rotor loads measurement, which is simultaneously performed with the DIC deformation measurement. The outline of the whole procedure is described in the flowchart shown in Fig. 2.9.

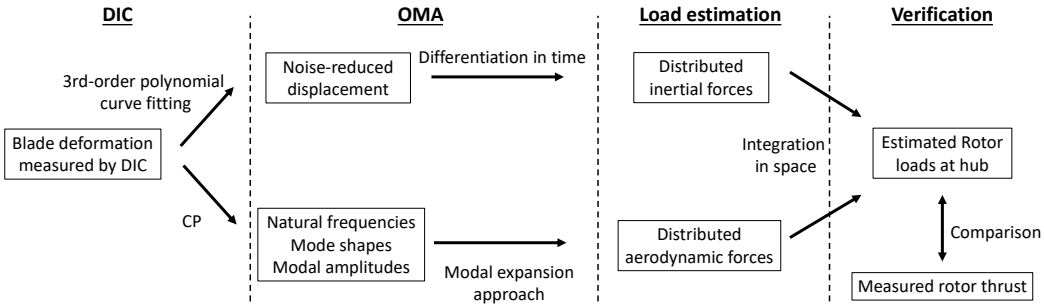

Figure 2.9: A flowchart of the whole approach proposed in this dissertation

2.3.3 Numerical experiment

Before the load estimation based on the measured data was examined, a numerical experiment was carried out using a finite element model of a one dimensional (1D) rotating cantilever beam with an arbitrary external forcing. The numerically-derived blade elastic response and modal parameters were used as an input to the present framework of rotor loads estimation approach, and the known external force was compared to that estimated by the present approach. The purposes of the numerical experiment were; (i) to examine if the approach proposed in this dissertation was feasible to estimate rotor loads distribution based on identified modal parameters and blade deformation and (ii) to evaluate the influence of the participating number of modes on accuracy of rotor loads estimation.

Figure 2.12 shows the original and estimated force distribution along the blade span, obtained from the numerical experiment on the 40-element (80 degrees of freedom) 1D rotating cantilever beam spun at 900 RPM. The

shape of the original excitation to the system followed a typical spanwise lift distribution along a helicopter blade, that is, the lift force increases as the local flow velocity increases towards the blade tip and the sharp drop occurs at proximity of the blade tip due to the strong downwash from the trailed blade tip vortices [68].

As can be seen in Fig. 2.10a, the first three modes were not enough to reconstruct the unique shape of the typical airload over the blade span, especially at regions near the blade tip. As the number of participating modes increased, the accuracy of the load estimation was improved and the overall shape was satisfactorily captured with 10 modes, as shown in Fig. 2.10c. From Fig. 2.10d to 2.10f, there was little improvement after the number of participating modes went beyond 15 modes.

From this numerical experiment, it was discovered that the proposed approach would require at least 10 modes to estimate a typical shape of aerodynamic loading over a rotating helicopter blade. Considering the general difficulty of experimentally identifying higher-order structural modes, which oscillate at high frequencies with low amplitudes, accurate estimation of spanwise lift distribution over the rotor blade with the identified modes might be impractical. However, hub loads (thrust), obtained by numerical integration of the lift distribution along the blade span, could be close to a value directly measured by a load cell installed in the rotating frame, according to Fig. 2.11, which compares the area under the distributed lift curves along the blade radial location for both the original and estimated load with the first three modes.

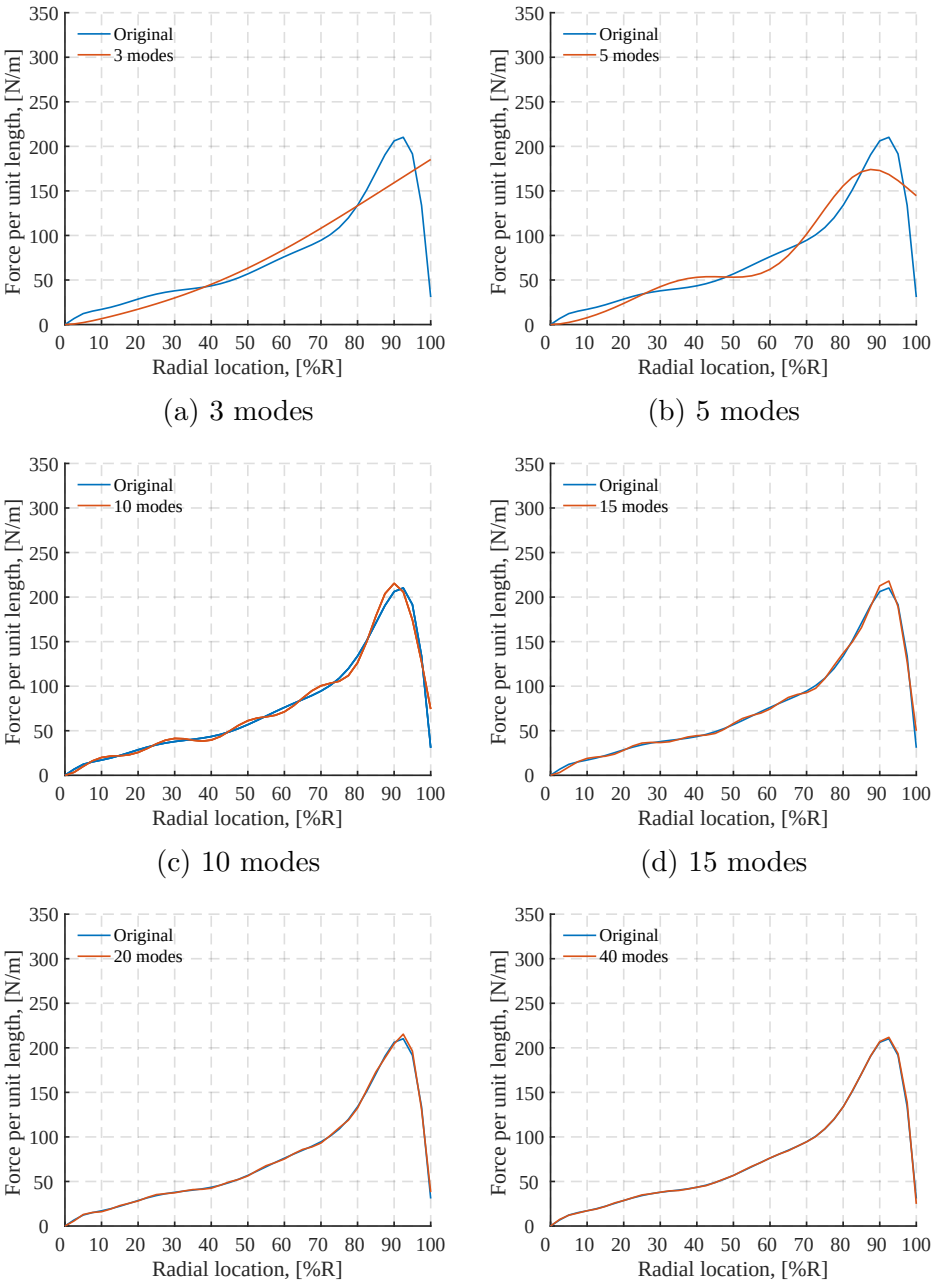

Figure 2.10: Comparison between the original and estimated lift distribution over the finite element 1D rotating beam

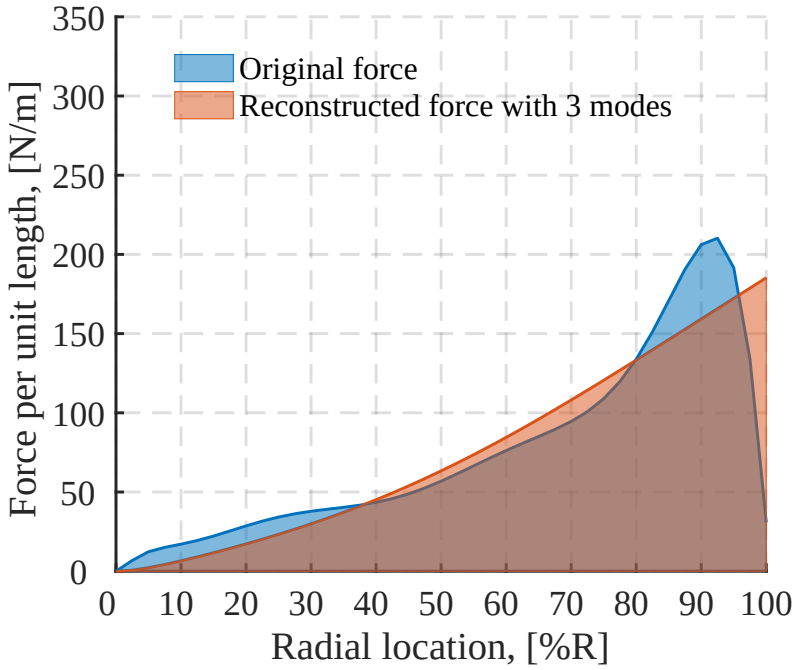

Figure 2.11: Integrated force comparison between the original and reconstructed loads

To quantitatively assess the influence of the number of participating modes on estimation accuracy, two metrics were used: One was the area difference between the original and estimated hub loads defined as Eq. 2.34, and the other was the root-mean-square (RMS) error of the spanwise lift distribution expressed as Eq. 2.35. $\hat{F}_z$ and F_z correspond to the estimated and original loads, respectively.

$$\text{Area difference} = \int_0^R d\hat{F}_z - \int_0^R dF_z \tag{2.34}$$

$$\text{RMS} = \sqrt{\frac{1}{R}\int_0^R [\hat{F}_z(x) - F_z(x)]^2 dx} \tag{2.35}$$

The area difference normalized by the mean original hub load and the RMS error are plotted in percentage as a function of the number of modes participating in the estimation process, as shown in Fig. 2.12a and 2.12b. Both plots show the common trend that the difference dramatically decreases from the first three to ten modes participation, and gradually converges towards zero. The conclusion from the qualitative analysis, that is, hub loads might be accurate even with a small number of modes participation, is now reinforced by the fact that the hub load estimated from the first three modes falls within approximately 2% deviation from the original value.

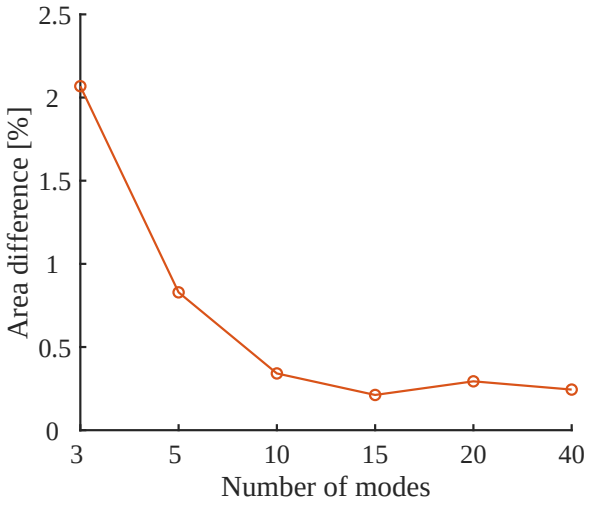

(a) Integrated loads difference

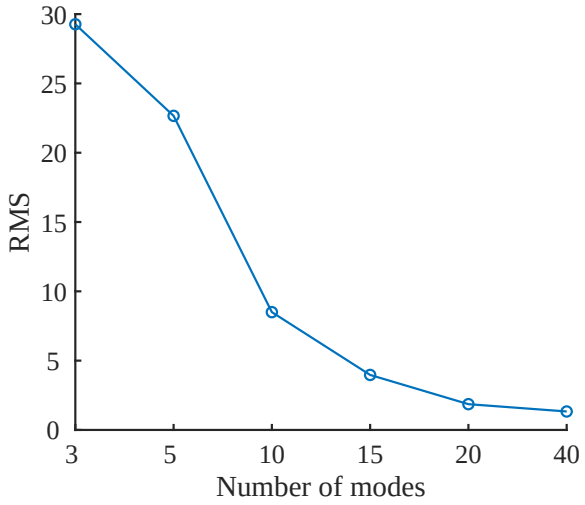

(b) RMS error of the spanwise lift distribution

Figure 2.12: Comparison between the original and estimated loads as a function of the number of participating modes

Chapter 3

Experimental Setup and Procedure

This chapter describes the experimental setups, test envelopes, and procedures conducted to validate the rotor loads estimation approach proposed in the dissertation. To verify the applicability of the present theoretical framework to various rotor configurations, blade deformation and rotor loads measurements were performed on two different scale rotor hover test stands:

- Small-scale test bench: A 0.46 m-diameter, two-bladed, extremely flexible rotor
- Large-scale test bench: A 2 m-diameter, single-bladed or two-bladed, single or coaxial counter-rotating (CCR) rotor

The rotor loads estimation starts with measuring the deformation time history of the rotor blade using the time-resolved DIC, which requires one to take a sequence of digital images over an entire rotor disk. The diameter of the rotor is an essential measurement parameter that determines the whole setup of the DIC measurement, including camera positioning and optical equipment arrangement. To show the scalability and flexibility of the methodology, the

current study performed the time-resolved DIC measurements on the small- and large-scale rotor blade.

Using these hover test rigs, three test campaigns were conducted. Test campaign 1 was performed on the small-scale, extremely flexible rotor hover test stand, and Test campaigns 2 and 3 were performed on the large-scale, 2 m-diameter rotor test stand at different rotor configurations and operating conditions. This chapter is divided into three sections. In § 3.1, the design, specification, and instrumentation of each rotor test stand are documented. In § 3.2, the camera arrangement, optical settings, and other details of DIC rotor blade deformation measurement on each rotor test stand are presented. In § 3.3, the measurement envelope and procedure of the three test campaigns are summarized.

3.1 Hover Test Stand

3.1.1 Extremely Flexible Rotor (small-scale test bench)

This rotor blade is extremely flexible; it is constructed out of a thin carbon fiber ribbon whose structural stiffness is negligible. The extremely flexible rotor blade concept has been proposed to increase the weight efficiency and survivability of helicopter rotors. In this concept, centrifugal force on the blades during rotation provides stiffness as well as stability. Because the elimination of a structural stiffness requirement results in reduced weight, such rotor blades have been proposed for heavy-lift helicopters. The low stiffness of the rotor blade precludes conventional methods of deformation measurement;

and makes it an ideal testbed for the DIC measurement. This subsection describes the key components of this extremely flexible rotor hover test stand.

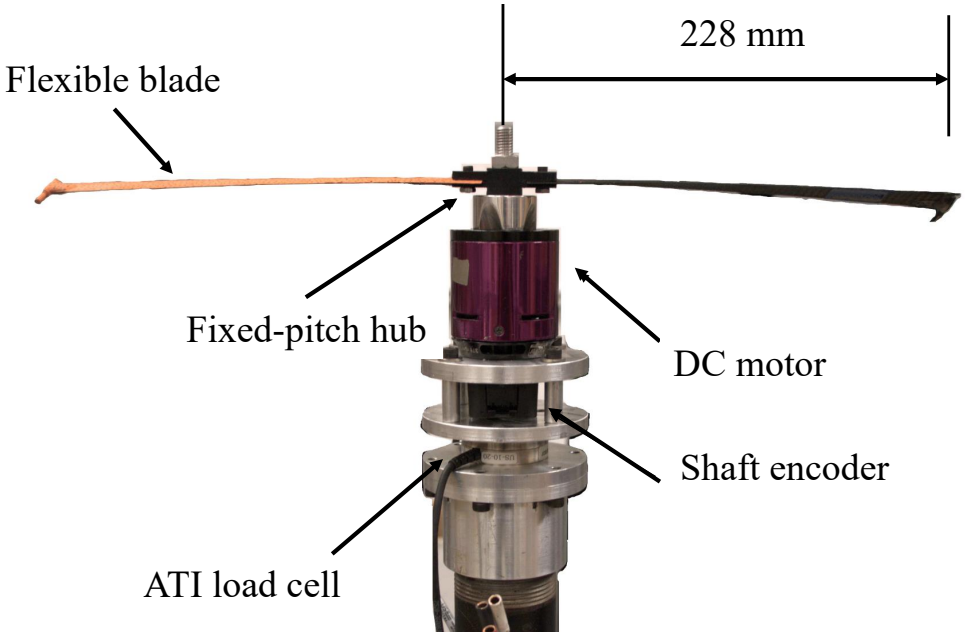

Figure 3.1: Side view of the rotor test article

3.1.1.1 Rotor configuration

The two-bladed rotor test article, shown in Fig. 3.1, consists of two flexible blades and a fixed-pitch rigid hub. The blade structure comprises two plies of $\pm 45^{\circ}$ AS4/3501-6 prepreg and a tungsten rod (25.4 mm long, and 2.4 mm diameter) held at the blade tip in a chordwise direction (see Fig. 3.2) to provide centrifugal stiffening and passive stabilization. A rectangular brass plate (51 μm thick, 7.6 mm length in chordwise, and 15.2 mm length in span-

wise direction) is inserted between the two plies of the composite laminate at regions of the leading edge, and a brass cylinder is directly soldered onto the plate. The brass structure with a small amount of epoxy is used to hold the tungsten mass at the blade tip. The blade is nominally untwisted with a constant thin circular arc airfoil profile; the thin, open section profile results in low bending stiffness and negligible torsional stiffness, both dominated by centrifugal force.

The fixed-pitch hub was designed in CAD and fabricated using a rapid-prototyping plastic 3D printer. Four different root pitch angles were selected for hover testing; 0°, 10°, 20°, and 30°. The rotor parameters are summarized in Table 3.1; note the low thickness to chord ratio of the rotor blades. The whole rotor assembly is placed onto a six-component strain gage load cell (ATI Mini-40) to measure hub loads. The rotor is driven by a brushless DC motor (Hacker A50-16S) and the rotational speed is measured by a 1024/rev optical incremental encoder (US Digital E5), as shown in Fig. 3.1.

Table 3.1: Rotor system parameters

Rotor diameter	456 mm
Root cutout	11 %R
Blade airfoil	Thin circular arc
Camber	9%
Chord	26.2 mm
Thickness to chord ratio	1.5%
Number of blades	2

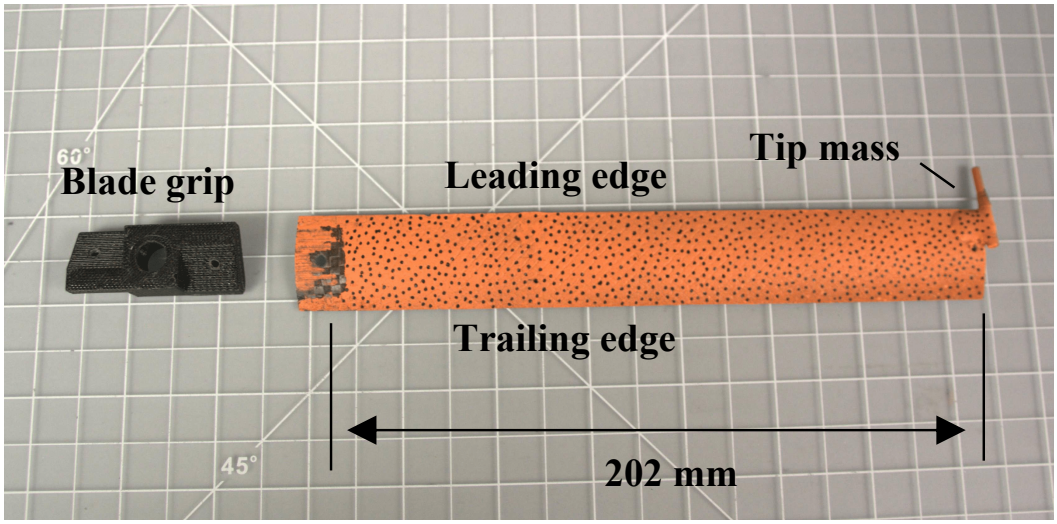

Figure 3.2: The hub and the flexible blade with the fluorescent paint and random speckle pattern

3.1.1.2 Data acquisition

Analog/digital signal data acquisition (DAQ) was obtained by a National Instruments (NI) multi-function data acquisition card (NI-PCI-6052E) with a 68-pin DAQ breakout connector (NI-SCB-68). Both analog signals from the ATI load cell and digital signals from the US DIGITAL optical encoder were acquired by the card. A high-speed counter on the DAQ card was used for measuring the azimuthal locations of the rotor with the incremental A, B, and one-per-revolution Z index channel from the encoder. Another high-speed counter on the DAQ card was used to downsample the original incremental signal from the channel A, and the downsampled digital pulse train was used for triggering shutter timing of high-speed cameras and laser strobing (for DIC

measurement) at integer multiples of the rotational frequency. The one-per-revolution pulse from the Z-index was used to synchronously start analog data logging and image acquisition.

3.1.2 Single-Bladed or Two-Bladed, Isolated Single or CCR Rotor (large-scale test bench)

A 2 m-diameter, rigid rotor hover test stand was designed, fabricated, and assembled as a large-scale test bench to measure the transient loads and blade deformations in hover. As shown in Fig. 3.3a and 3.3b, the hover stand can be configured as a single-bladed or two-bladed, isolated single or coaxial counter-rotating (CCR) rotor. Note that the rotor stand, shown in Fig. 3.3, is oriented horizontally to facilitate imaging of the entire rotor disk, needed to perform the DIC blade deformation measurement.

3.1.2.1 Drive system

A hydraulic power unit drives the rotors through a belt-driven transmission system with synchronous 64-toothed belts and pulleys. As shown in Fig. 3.4, there are two belt-pulley arrangements in the transmission, each corresponding to the upper rotor or lower rotor in CCR rotor configuration. Row 1 in Fig. 3.4 is connected to the inner main shaft, which rotates the lower rotor in a clockwise direction, whereas row 2 is connected to the outer main shaft, which rotates the upper rotor in a counter-clockwise direction. In the CCR rotor configuration, a serpentine belt with an idler causes the upper and the lower rotors to spin in the opposite directions at the same rotational speed.

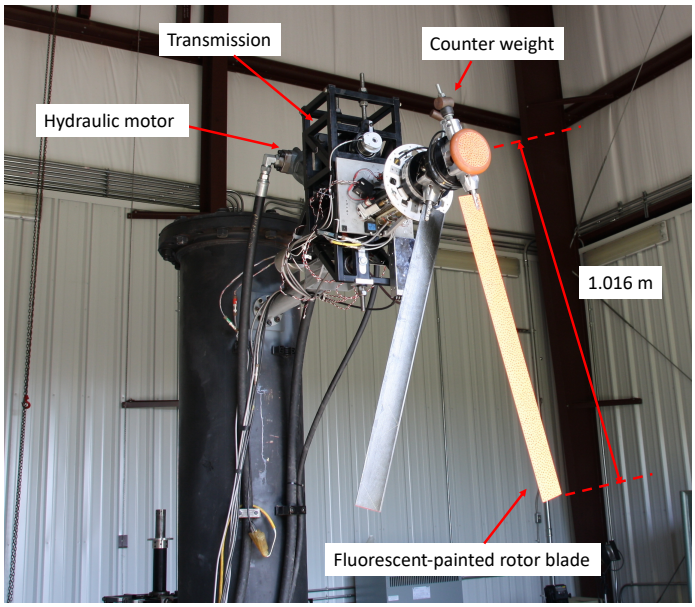

(a) Single-bladed, CCR rotor configuration

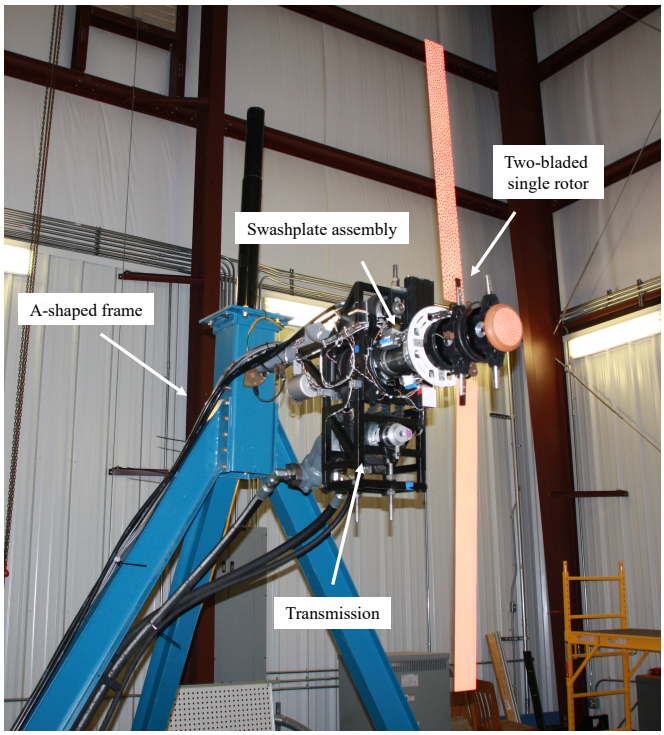

(b) Two-bladed, isolated single rotor configuration

Figure 3.3: The large-scale rotor test stand

A hydraulic motor (Rexroth AA2FM-63) attached to the drive shaft spins the upper and lower pulleys together, and the maximum power provided by the hydraulic unit is 105 kW at 4000 RPM.

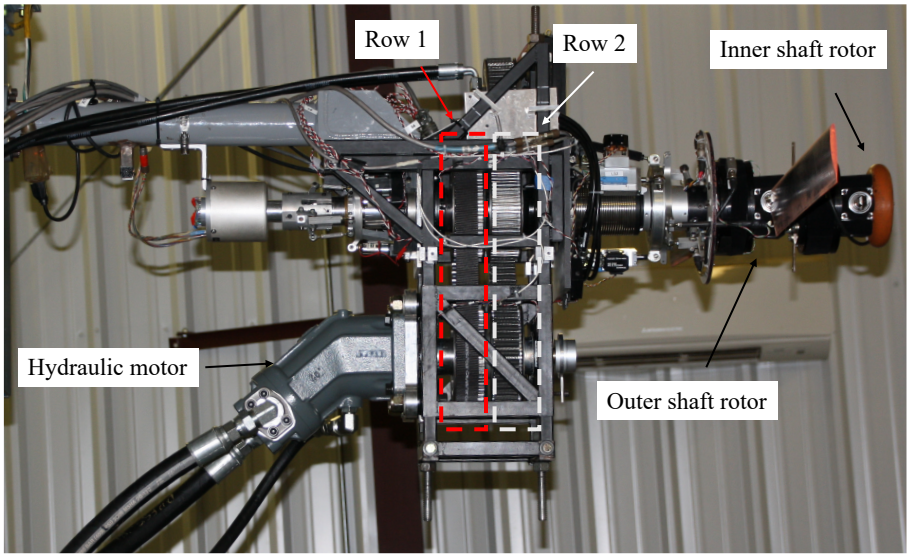

Figure 3.4: Side view of the transmission system

3.1.2.2 Rotor configuration

The CCR rotor system is designed to replicate the X2TD rotor system [69], featuring a rigid hub and a closely-spaced CCR rotor. The specifications of the rotor system are summarized in Table 3.2. For the CCR rotor system, the blade passages occur at the top and bottom of the rotor disk, i.e.,

at azimuthal angles of 0° and 180°. In single-bladed rotor configurations, one rotor blade and a counter-weight are attached to each rotor, whereas in two-bladed rotor configurations two identical blades are attached to each rotor. A counter-weight is attached to the hingeless hub to balance the location of the center of mass (CM) of each rotor. The counter-weight assembly consists of a cylindrical-shaped steel solid piece, a threaded rod, and a rod fixture on the hub. To adjust the location of CM of the entire rotor assembly, the location of the steel piece can be readily changed by rotating the threaded rod.

Table 3.2: Summary of rotor parameters for the large-scale hover test stand

Parameter	**Single**	**Coaxial**
Number of blades N_b	1 or 2	1 or 2 (each)
Radius R, m	1.016	
Root cutout, m	0.122	
Rotor spacing, m	-	0.140
Airfoil section	VR-12 with 5% trailing edge tab	
Precone, deg.	3	
Chord c, m	0.080	
Solidity σ	0.025 or 0.05	0.05 or 0.10
V_{tip}, m/s	95.8	
Rotational speed Ω, RPM	900	

3.1.2.3 Rotor blade

Rotor blades used on the large-scale test stand have the following features: no taper, constant chord, uniform VR-12 airfoil section including a 5% trailing edge tab. The blade structure is made of a foam core and forward D spar, wrapped with carbon-epoxy composite materials (a plain-weave

AS4/3501-6 prepreg and an IM7/3501-6 uni-directional carbon fiber tape). The foam core in the D-spar is machined to place tungsten weights along the leading edge, for adjusting the location of the blade center of gravity. The $\pm 45^{\circ}$ orientation plain-weave fabric provides increased torsional stiffness. Rohacell IG31-F closed cell foam is used for the core and FM-300K film adhesive is used to bond the carbon fiber prepreg to the form core. At the blade root, a rectangular aluminum insert is placed onto the form core to provide compressive strength where the rotor blade is clamped in the blade grip of the hub. Figure 3.5 shows a breakdown of the blade laminate lay-up.

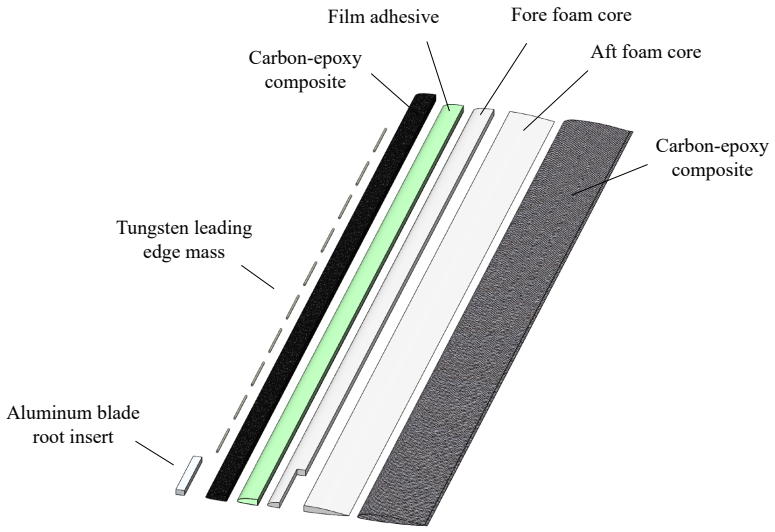

Figure 3.5: An exploded view of the rotor blade composite laminate

3.1.2.4 Rotor hub

The rotor hingeless hub consists of three key components; single-piece central hub structure, blade grip and bearing carrier, and six-component load cell as shown in Fig. 3.6. The single-piece central hub structure is made of aluminum and designed to be directly mounted onto the load cell. There are four ports on the side of the central structure, each corresponding to a rotor blade attachment, i.e., the hub can be configured as a four-bladed rotor system. At each port, a modular blade grip and bearing assembly is attached and used to clamp the rotor blade and allow pitch feathering motion. A cross-section view of the modular blade grip and bearing carrier assembly is shown in Fig. 3.7. The bearing carrier packages three types of bearings; a roller thrust bearing to support high axial (centrifugal) load and two needle roller bearings to support thrust and flap-bending moments.

Below the central hub structure, a custom-modified, six-component load cell (ATI Omega-160) is installed and measures hub loads in the rotating frame for each rotor. Each load cell was modified to include on-board signal conditioning to minimize slip-ring noise when transmitted from the rotating frame to the fixed frame. High sensitivity silicon-based strain gauges allow for stiff construction, resulting in large overload capacity and favorable dynamic response. The resolution of force and moment measurements is 0.75 N and 0.025 Nm, respectively, based on the manufacturer specificaation. In-plane forces are measured with bias accuracies of ± 4 N, while thrust is measured with a bias accuracy of ± 8 N. All moment measurements had bias accura-

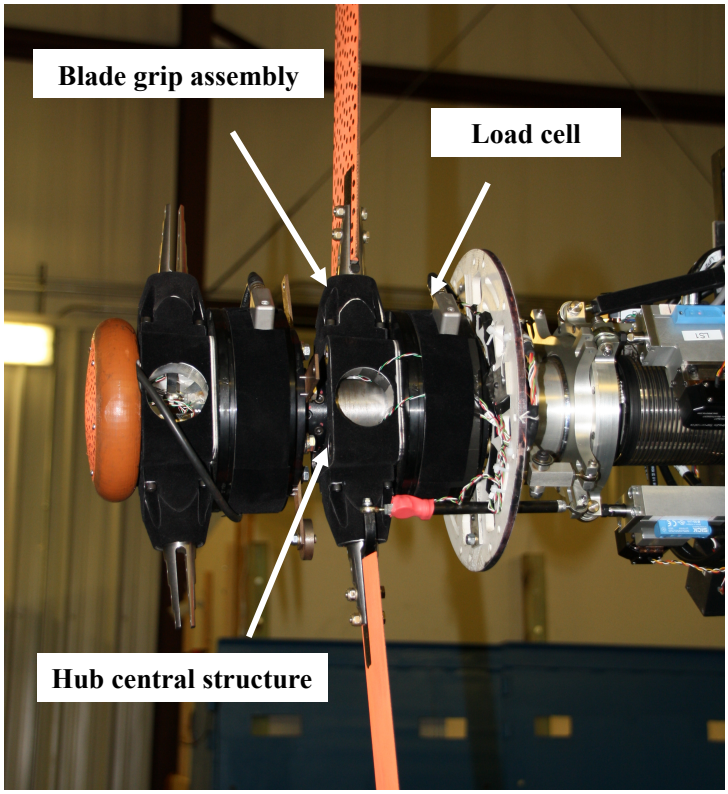

Figure 3.6: Primary components of the rotor hub

cies of ±0.5 Nm. While the isolated load cell has a natural frequency above 1000 Hz, the addition of the hub, blade, and counter-weight significantly modifies the frequency response. An in-situ dynamic calibration was performed on the vertical (F_Z) component of each load cell using a calibrated impact hammer. The resulting transfer functions for the upper and lower rotors are shown in Fig. 3.8. The load cell response remains flat until about 140 Hz, or 7-per-revolution at a rotor speed of 1200 RPM. These transfer functions were

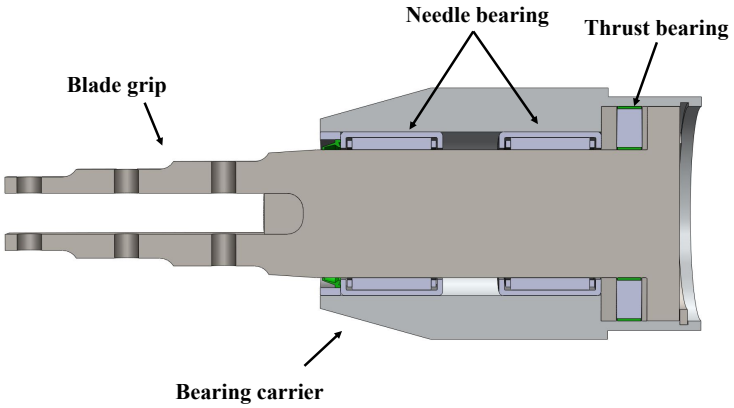

Figure 3.7: A cross-section view of the blade grip assembly

used to correct the measured F_Z hub loads presented throughout the study.

3.1.2.5 Blade root pitch angle sensor

Two different blade root pitch angle sensors were tested: A linear Hall effect sensor (Honeywell SS495A1) and an Anisotropic Magneto-Resistive (AMR) position sensor (KMZ60).

The Hall effect sensor is mounted onto a stationary fixture inside the central hub structure, and two Neodymium magnets are bonded to the bottom surface of the blade grip. This root pitch measurement system operates based on the Hall effect: the sensor measures the variation of magnetic field as the two Neodymium magnets of opposite polarity rotate with the pitching motion of the rotor blade grip. Details of the instrumentation and specification of the Hall effect pitch angle sensor are available in Ref. [70]. The Hall effect sensor

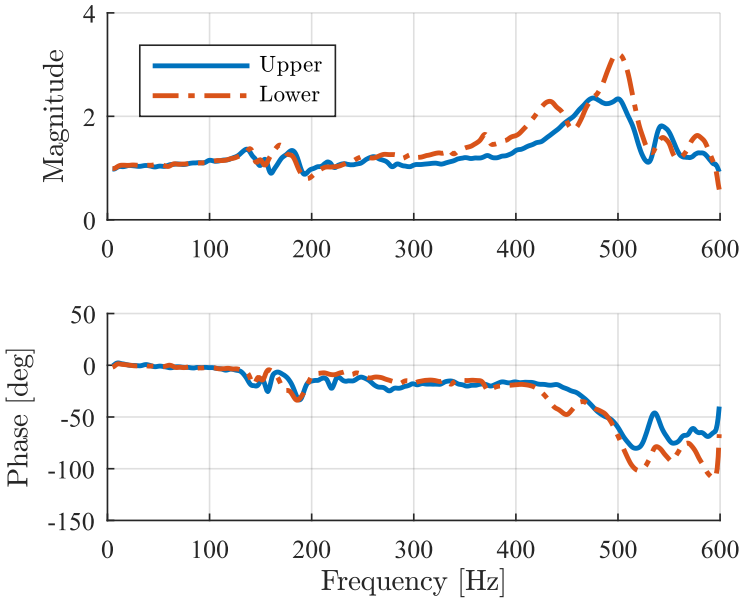

Figure 3.8: Dynamic response of upper and lower rotor load cells

was used for initial tests, however, it was found that the sensor often needed re-calibration.

Fig. 3.9 shows a schematic of the AMR sensor installation on the blade grip assembly. The AMR sensor generally consists of a thin film of ferromagnetic metals such as Ni and Fe. The resistance of the thin film varies according to the strength of the applied magnetic field along a specific direction. The sensor uses the variation of resistance, which results in voltage change. The AMR sensor is held on a stationary plate and a Neodymium magnet is bonded to the face of the blade grip, as shown in Fig. 3.9. The stationary plate is mounted on to the blade grip carrier in a way such that the feathering axis of the blade

grip is aligned to the coordinate system of the AMR sensor. Then by placing the magnet at the center of the blade grip face, the AMR sensor can detect the variation of the magnetic field associated with the feathering motion of the rotor blade.

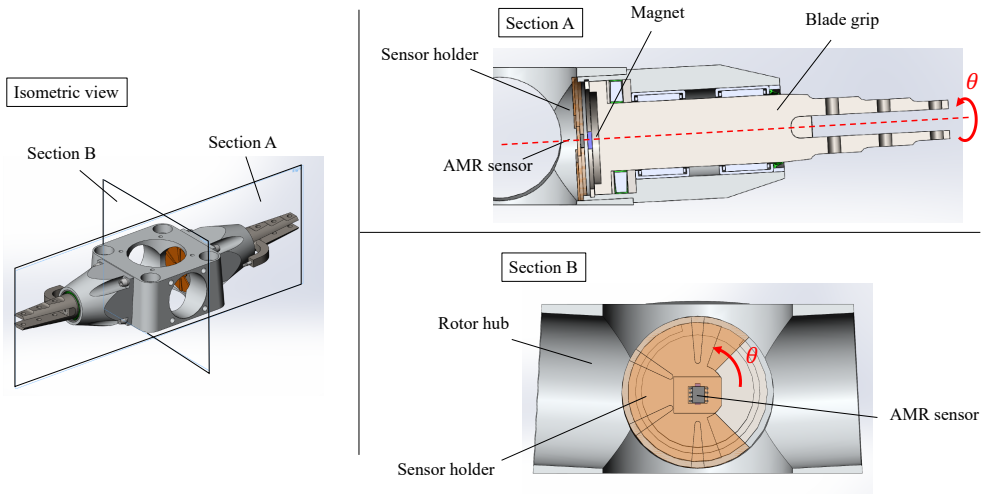

Figure 3.9: A schematic of the AMR sensor installation on the blade grip assembly

The AMR sensor provides ratiometric sine and cosine analog output signals and its calibration is performed using an absolute optical inclinometer (US A2T series). Figure 3.10a shows the variation of the two output voltage signals from the AMR sensor as a function of rotational angle measured by the inclinometer. A rotating magnetic field delivers the two sinusoidal output signals with the double frequency of the mechanical angle between the sensor and magnetic field direction. The angle can be calculated using the following

equation:

$$\alpha = \frac{\arctan\left(V_{SIN}/V_{COS}\right)}{2} \tag{3.1}$$

where α is the angle between the sensor and magnetic field direction, V_{SIN} and V_{COS} are sine and cosine analog output signals, respectively. A sinusoidal function $f(x) = A\sin\left(Bx + C\right) + D$ curve-fitted to the sensor output over the angle range of interest is shown in Fig. 3.10b and the curve-fitting coefficients with 95% confidence are summarized in Table 3.3. The uncertainties based on the standard deviation calculated from three individual repeated measurements are shown as the highlighted area in Fig. 3.10c. The measurement uncertainty was computed to be ± 19 mV and corresponds to approximately 0.38 deg. Note that the current study used only the sine signal due to the number of measurement channels available in the data acquisition system.

Table 3.3: Summary of the curve-fit coefficients to the AMR sensor output signal

$f(x) = A\sin\left(Bx + C\right) + D$	
A	1.456 ± 0.003
B	1.951 ± 0.005
C	0.119 ± 0.002
D	2.506 ± 0.003

3.1.2.6 Control system

The pitch angle control system consists of two independent swashplates actuated by three custom servo actuators used to control collective and cyclic pitch for the upper and lower rotor independently in the CCR rotor configuration. Each swashplate is connected to a pitch horn on the blade grip by a

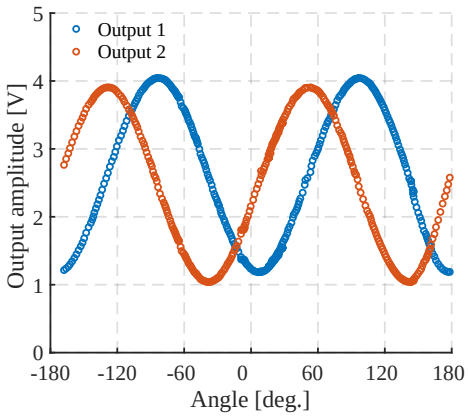

(a) Sine and cosine output signals from the AMR sensor

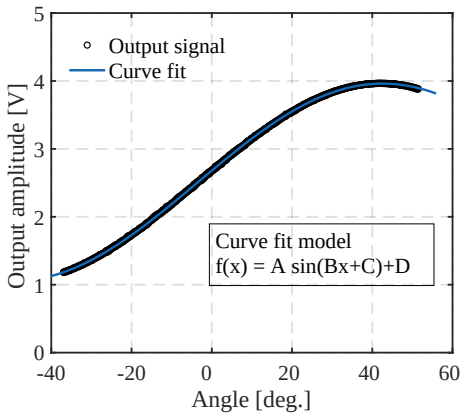

(b) Curve-fit to the voltage variation from the AMR sensor

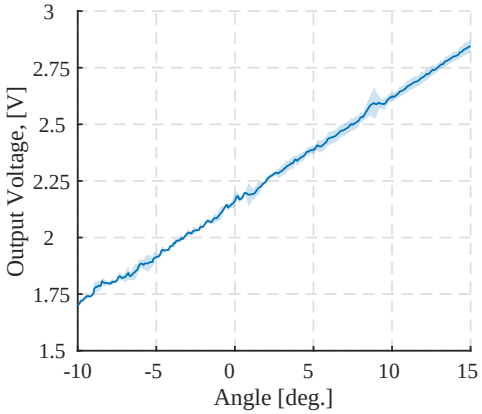

(c) Output voltage signals from the AMR sensor with measurement uncertainty

Figure 3.10: The AMR sensor characteristics

pitch linkage. Due to the unique load path and load cell configuration of the rotor assembly, pitch link loads must be measured and subtracted from load cell measurements for recovering the true rotor hub loads. As such, tension-compression load cells with a full-scale range of ±250 N and an accuracy of ±0.5 N are installed in each pitch link to measure the variation of pitch link forces as a function of blade azimuthal angle and appropriately correct the hub load cell measurements.

There are two different custom-designed servo actuators installed on the rotor stand:

- A lead-screw actuator
- A hydraulic actuator

The first design, a lead screw servo actuator, uses a lead-screw rod, driven by a brushed DC motor through a gear reduction system. The main design target of this servo actuator was to maintain or change the blade pitch angle under severe rotor load conditions with high servo resolution and low compliance. Table 3.4 summarizes the specification of the lead-screw servo actuator, and further details can be found in Ref. [70].

The second servo design, a hydraulic actuator, was designed to achieve dynamic rotor pitch variation. As shown in Fig. 3.11, the hydraulic actuator assembly consists of three components: a main actuator structure, a hydraulic servo valve, and a piston position sensor. The main actuator structure (a

Table 3.4: Specifications of the lead-screw servo actuator

Parameter	**Lead-screw servo**
Resolution [μm]	16
Repeatability [μm]	25
Maximum pitch angle error [deg]	0.05
Maximum pitch angle velocity [deg/s]	7.7
Force at maximum power [N]	1750

piston and a cylinder body) was designed in-house and fabricated by an external manufacturer (SMC Corporation of America). The hydraulic servo valve (KNR Systems) has a capability of operating 5.5 L/min at pressure of 70 bar at a bandwidth above 60 Hz. The piston position feedback sensor (SICK MPS-T position sensor) is mounted on a T-slot outside the cylinder body and continuously detects the variation of the magnetic field generated from a magnet installed on the piston. The whole rotor control assembly with the hydraulic actuation system is shown in Fig. 3.12

A block diagram of the pitch angle control system for the hydraulic actuation is shown in Fig. 3.13. In the pitch control signal line, input commands (collective and cyclic pitch angle position) are first provided to a central control panel. These PWM signals are then sent to a signal distribution panel, which takes 12 V power from a power supply, and the power and signals are distributed to three micro-controllers (Pololu jrk 21v3). Each micro-controller takes a feedback signal from the position sensor and drives the hydraulic servo valve of each actuator for closed-loop control of the piston position.

The hydraulic unit is controlled by a manufacturer-provided (KNR Sys-

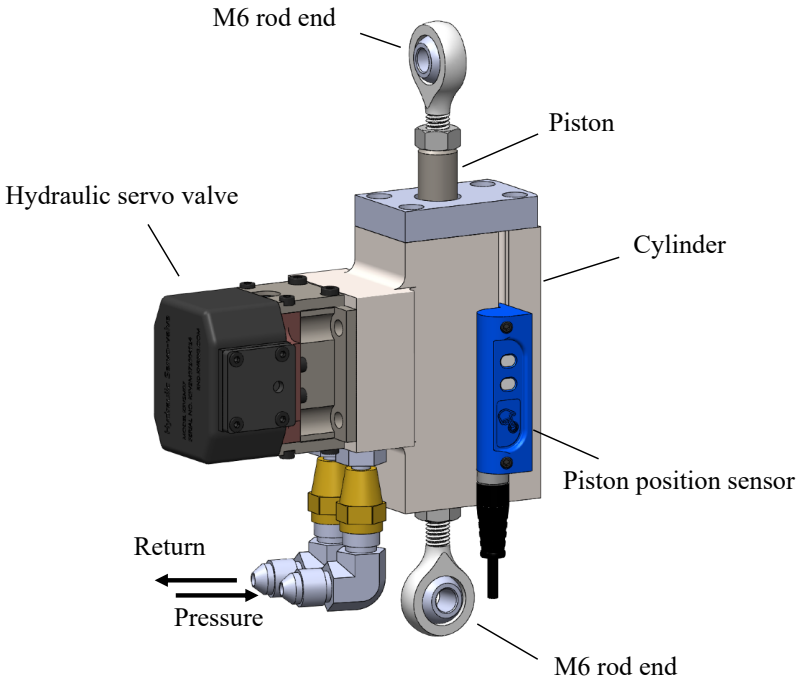

Figure 3.11: A drawing of the hydraulic servo actuator assembly

tems) control software. First, users set a pressure level and hydraulic flow rate on the software and these parameters are sent to a mobile Hydraulic Power Unit (mHPU) that supplies the hydraulic flow at the specified pressure and rate. The fluid flow is distributed by a hydraulic manifold to the three individual actuator assemblies. This hydraulic actuation system allows dynamic variation of rotor blade pitch angle, as compared to the lead-screw servo actuation system.

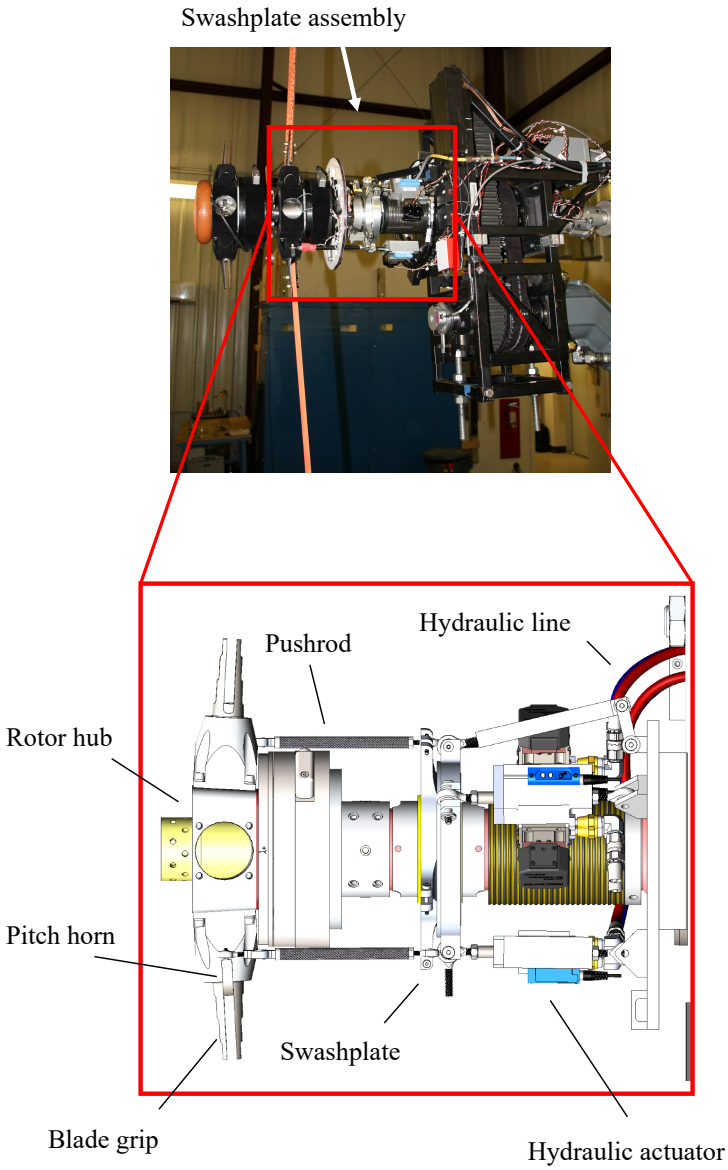

Figure 3.12: Rotor pitch angle control system assembly with the hydraulic servo actuators

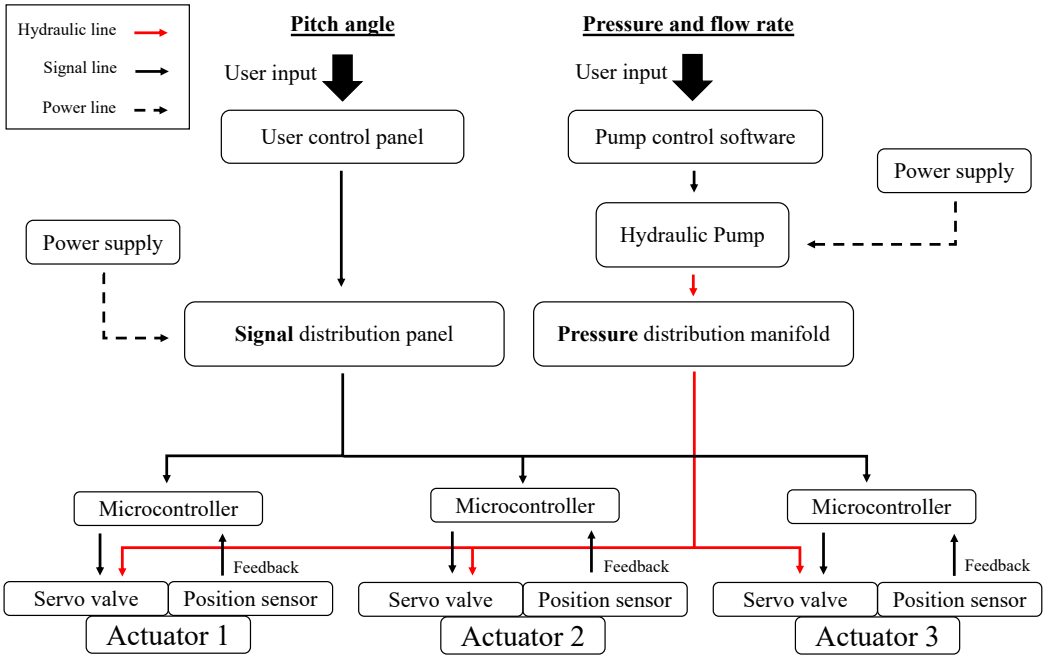

Figure 3.13: A diagram of pitch angle control system for the hydraulic actuation

3.1.2.7 Fixed-frame instrumentation

Fixed-frame instrumentation is designed to monitor several key parameters of the hover test stand for safety, including vibration level of the test stand and bearing temperatures. Also, an optical incremental encoder used for measuring the rotational speed of the rotor is categorized as fixed-frame instrumentation, because it is mounted on the drive shaft and the transmission frame in a stationary manner.

A two-axis MEMS accelerometer (ADXL-330) is mounted onto the

transmission for monitoring the fixed-frame vibration. Data from the accelerometer is also used to analyze the dynamic imbalance of the rotor system before testing, and to monitor dynamic unsteady loads observed during actual hover testing. Four precision integrated-circuit temperature sensors with an output voltage linearly-proportional to the Centigrade temperature (Texas Instruments LM35) are installed onto four bearing housings (two for the main shaft, and two for the drive shaft) to monitor bearing health.

A 4096 count/rev, hollow-bore, optical incremental encoder (US Digital HB6M) is mounted to the drive shaft. This encoder provides the one-per-revolution Z-index signal, in addition to the A and B timing signals. The primary use of the encoder is; blade azimuth angle and rotational speed measurement, timing reference for synchronous averaging of multiple revolutions during data post-processing, and triggering the image acquisition equipment (high-speed cameras and a laser strobe) for the DIC measurements.

To transfer electrical signals from the instrumentation installed in the rotating frame to the fixed frame DAQ system, two slip rings, each corresponding to the upper and lower rotor instrumentation, are used. A 24-channel self-contained slip ring, manufactured by Fabricast is selected for the upper rotor, whereas a 26-channel separate rotor and brush block assembly is used for the lower rotor.

3.1.2.8 Data acquisition

Signal data acquisition (DAQ) from all the instrumentation described above is conducted by a National Instruments (NI) PXI system. NI PXI system generally consists of a PXI chassis and instrument modules; the chassis supplies power, cooling, and a communication bus for the modules, while instrument modules acquire and generate analog/digital signals. The instrument modules can also be used to trigger and synchronize measurement signals. In the current test setup, the chassis houses three multi-function DAQ cards, one PXI-6225 (maximum sample rate = 250 kS/s) and two PXIe-6358 (maximum sample rate = 1.25 MS/s). The PXI-6225 card was mainly used for the data acquisition from the fixed-frame instrumentation (temperature sensors and accelerometers), whereas the PXI-6358 cards were used for the instrumentation in the rotating frame, such as the load cells and root pitch angle sensors.

3.2 DIC Deformation Measurement

3.2.1 Small-scale rotor

DIC blade deformation measurement on the small scale rotor hover test stand (see § 3.1.1) was performed in the test chamber shown in Fig. 3.14 and its schematic is shown in Fig. 3.15. To acquire the time history of the rotor blade deformation, a sequence of digital images over the whole rotor disk must be taken. This was accomplished by mounting high-speed digital cameras on linear camera rails above the rotor plane with their axes oriented approximately 45° with respect to the rotor disk, as shown in Fig. 3.15. The stereoscopic ar-

rangement of two cameras (Phantom Miro M310 with Nikon NIKKOR f/1.8D 35 mm lens) enables measurements of three-dimensional displacement fields on the entire flexible blade. Knowing the positions of two cameras relative to each other and the magnifications of lenses, the stereoscopic DIC algorithm can calculate the absolute three-dimensional coordinates of any point on the blade surface.

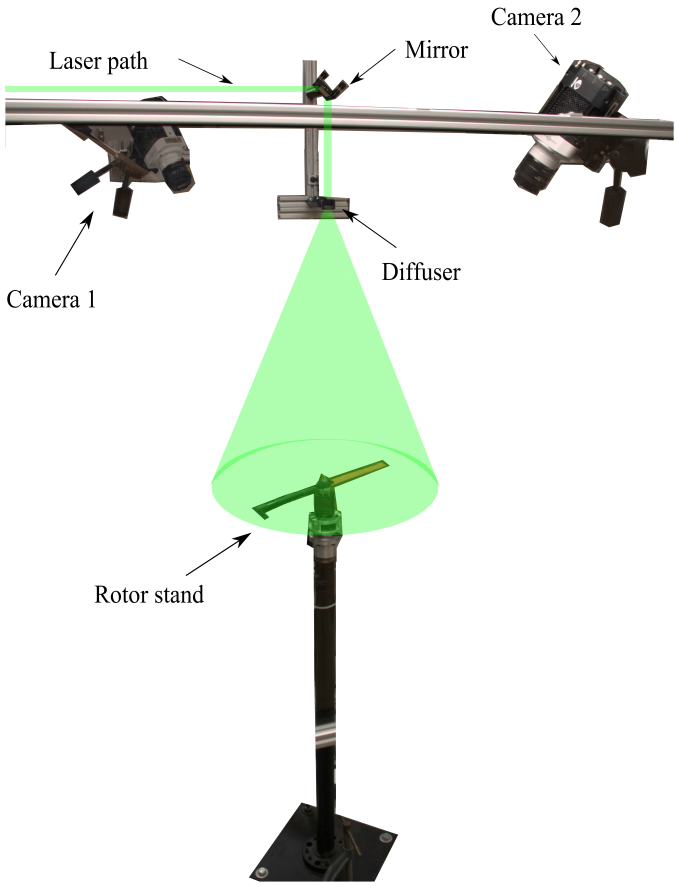

Figure 3.14: The setup for small-scale rotor blade deformation measurement.

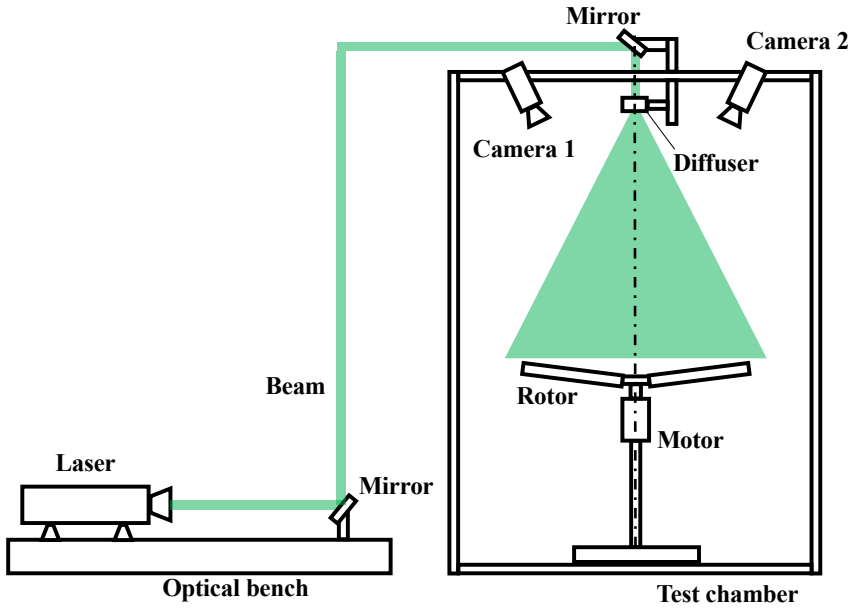

Figure 3.15: A schematic of the small-scale DIC measurement setup

A key step in implementation for a successful DIC measurement is the preparation of the test article, which in this case is the flexible rotor blade. A stochastic, high contrast intensity distribution that deforms with the surface of the structure allows the algorithm to detect the speckle pattern in images, resulting in good cross-correlation between reference and deformed images. One way to obtain high contrast digital images is to enlarge the aperture opening of the cameras to allow more light to reach the CCD image sensors while illuminating the target surface by a bright light source. The resultant images would have high light intensity difference between the surface

of the structure and the environmental background; however, this approach may cause out-of-focus images due to shallow depth of focus inherent to a large aperture setting. Increasing exposure time while maintaining a small aperture value is an alternate approach, however, increased exposure time would cause more blurry images. Thus, the present study makes novel use of two techniques for DIC measurement: fluorescence and pulsed laser illumination.

Fluorescence is a chemical process that emits light at a certain wavelength, triggered by molecular absorption of photons or other electromagnetic radiation. Since the emitted light has a specific wavelength, an appropriate selection of camera lens filters would allow only the light emitted by the fluorescent paint to pass through and reach the camera image sensors. Therefore, if the surface of the target structure is painted with fluorescent paint and a random speckle pattern is painted on the surface with some non-fluorescent color, one can readily obtain high contrast images of the applied speckle pattern; the background area unnecessary for DIC processing can be automatically removed by masking algorithms. Moreover, if a pulsed laser is used as a light source, a very short duration exposure can be achieved to eliminate blur in the images. This visualization technique is called Laser-Induced Fluorescence (LIF) or Laser-Stimulated Fluorescence (LSF); it has been used recently on a variety of materials and structures, such as gossamer, transparent, reflective aluminum-coated, and polymer membranes [71, 72, 73, 74].

As can be seen in Fig. 3.2, orange fluorescent paint was applied on the blade surface and a random pattern of black dots was painted on the

surface. A Photonics dual-head Nd:YLF DM-30 pulsed laser strobe with a wavelength of 527 nm and a pulse energy of 30 mJ/pulse routed through an engineered diffuser was used to illuminate the entire rotor disk at any desired instant of time (as shown in Fig. 3.15). The short duration pulsed laser illumination enabled a high f-number (f/8.0D) and a short exposure time (10μs) for all the images captured for DIC. The optical incremental shaft encoder on the rotor shaft was used to generate a 16-per-revolution pulse train, which triggered laser strobing and image acquisition at 16 evenly-spaced azimuthal locations. Since the maximum rotational speed was set at 25 Hz, the maximum sampling rate was 400 Hz. At each test condition, images were taken over 400 rotor revolutions, yielding 6400 images per camera over 16 seconds. Note that reference (undeformed blade) images for DIC calculations were captured at the same azimuthal locations by rotating the rotor shaft slowly by hand, i.e. at a negligibly small rotational speed, thereby eliminating any aerodynamic forcing. Figure 3.16 shows the unprocessed images of the rotor at 1200 RPM acquired by the high-speed camera at 16-per-revolution, overlaid on each other to illustrate the complete rotor disk; a typical DIC interrogation window is also shown for reference.

After the images were captured by a stereo pair of high-speed cameras, the DIC software (LaVision DaVis 8 Strain Master 3D) was used to calculate the deformation of the blade. The complete image (of size 1280 x 800 pixels) was divided into a number of interrogation windows and one displacement vector was calculated for each interrogation window. The size of the window was

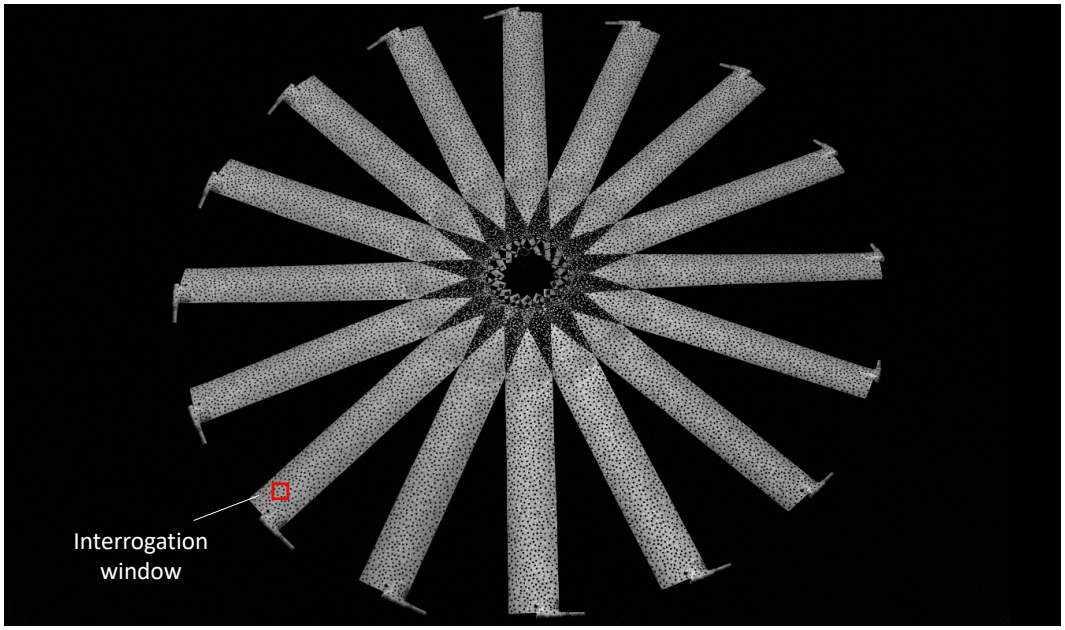

Figure 3.16: Unprocessed images of the rotor strobed at 16 azimuthal locations, showing complete rotor disk at 1200 RPM.

selected as 19 x 19 pixels and the window shift was set to be 5 pixels for mapping the interrogation windows to the whole image, resulting in 54% overlap. The camera scaling factor was approximately 2.24 pixel/mm determined by the geometry of the test setup as well as the camera lens characteristics. Deformations at a total of 988 locations (13 chordwise and 76 spanwise locations) were calculated at each azimuth.

A critical step for obtaining 3D displacements from recorded images is the calibration of the high-speed camera system prior to the measurements. Figure 3.17 shows the calibration process for the cameras, using a standard calibration plate placed at the rotor plane. Information of the size and location

of the calibration plate with respect to the rotor plane enables calculation of a mapping function between the global coordinates and camera image plane coordinates. With the help of mapping functions calculated during the camera calibration process, the two two-dimensional vectors from each camera are combined to yield a three-dimensional vector. The accuracy of the vectors depends on the size of the interrogation window and is estimated to be 0.01%R (0.023 mm), while the spatial resolution of the displacement field is 0.2%R (0.45 mm). A sample processed result for the 30° root pitch rotor, rotating at 1500 RPM, is shown in figure 3.18.

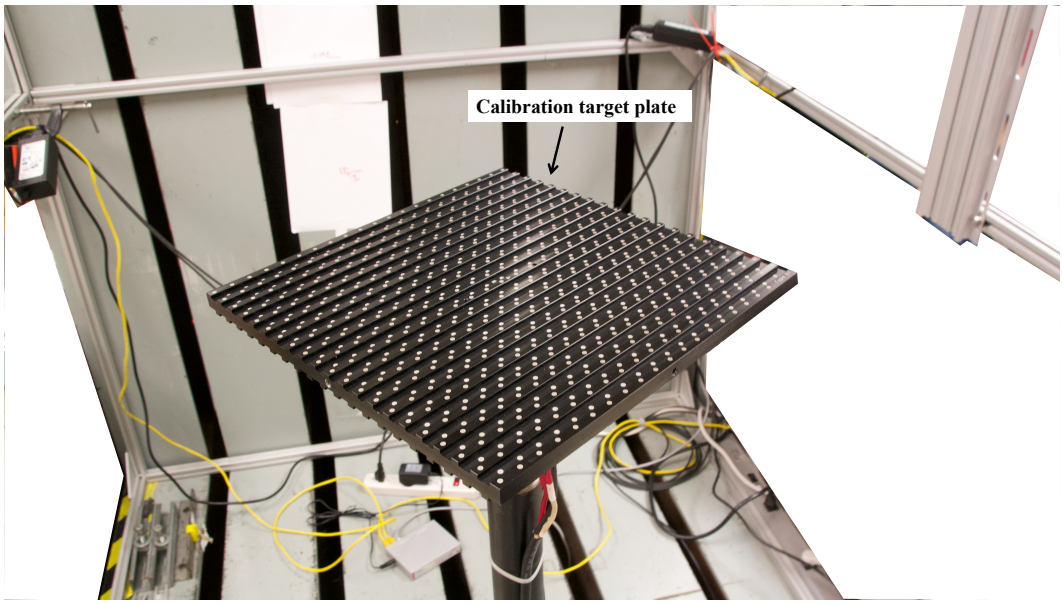

Figure 3.17: Camera calibration target

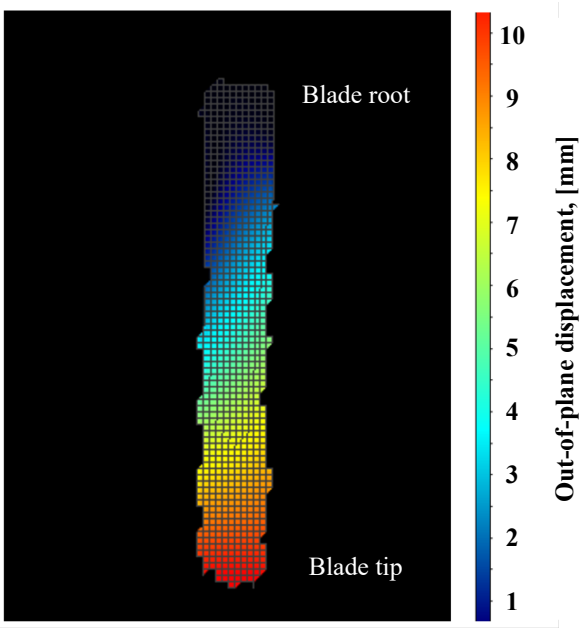

Figure 3.18: Vector map processed by DIC for the 30° root pitch rotor, spun at 1500RPM

3.2.2 Large-scale rotor

In addition to the small-scale rotor measurements, the time-resolved DIC technique with LIF strobing was applied to the large-scale rotor test stand (see § 3.1.2). The basic concept of large-scale DIC is the same as that of small-scale DIC described in § 3.2.1, that is, a stereoscopic camera system captures the whole area of the rotor disk so that the deformation time history of the blade structure can be obtained. However, due to the scale-up of the rotor diameter (from 0.46 m to 2 m), several modifications were required for a successful large-scale DIC blade deformation measurement. One of these modifications was the horizontal orientation of the rotational axis that facilitates

imaging of the whole rotor disk as shown in Fig. 3.3. Other modifications are discussed in this subsection.

Figure 3.19 and 3.20 show one of the stereoscopic camera arrangements used for the large-scale DIC measurement. In the setup, three high-speed cameras were used to image the entire rotor disk. The first and second cameras (Phantom Miro M310 with Nikon NIKKOR f/1.8D 35 mm lenses) were mounted so that each camera captured the entire rotor disk, and the third camera was mounted on a tripod located between the first and the second camera. At some azimuthal locations, images taken by the left and right cameras (Camera No. 1 and Camera No. 3) were distorted due to large parallax. These images were corrected using images taken by the middle camera (Camera No. 2).

As was the case for the small-scale DIC measurement, orange fluorescent paint with stochastic speckle patterns was applied to the blade surface as shown in Fig. 3.21, and the LIF strobing was achieved by a digital pulse train generated from the optical encoder installed onto the drive shaft (see § 3.1.2). A schematic of the whole DIC measurement setup is shown in Fig. 3.22. Camera exposure time was maintained at 10 μs. The short exposure time with laser strobing enables a high contrast (almost pure black and white), blur-free image acquisition. Figure 3.23 shows unprocessed images taken by the three cameras that were triggered at a certain azimuthal angle.

High-speed camera calibration was performed using a calibration plate placed at the rotor plane in order to obtain a mapping function between global

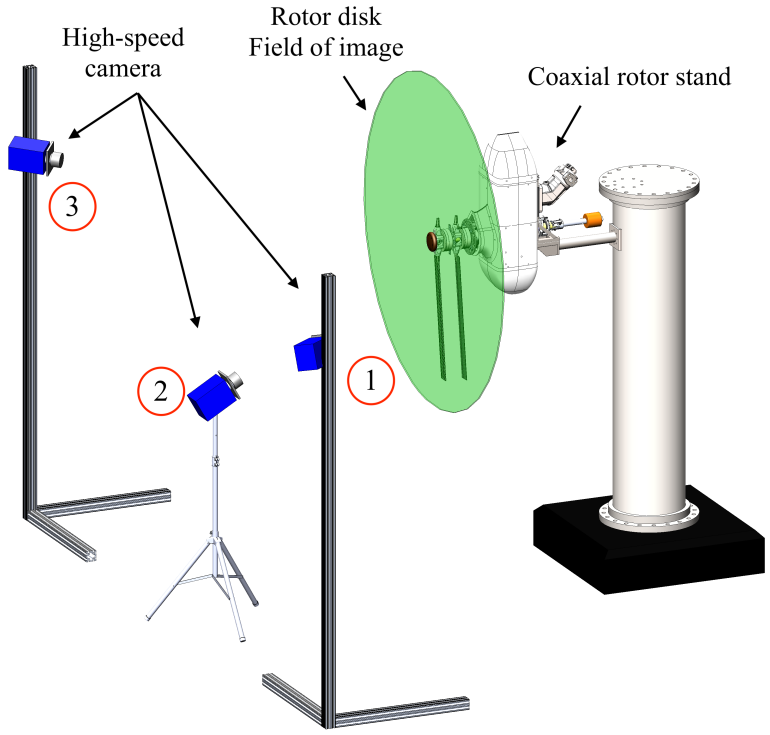

Figure 3.19: A schematic of camera arrangement for the large-scale DIC test

and camera image plane coordinate system. To cover the larger field of interest than that for the small-scale DIC, a large calibration plate was used, as shown in Fig. 3.24. The large calibration plate was moved around to cover the whole area of the rotor disk. The displacement accuracy for the large-scale rotor blade was estimated to be $0.01\%R$ (0.1 mm), and the spatial resolution of the displacement field was estimated to be $0.2\%R$ (2 mm).

Figure 3.20: Stereoscopic camera system for the single-bladed CCR rotor

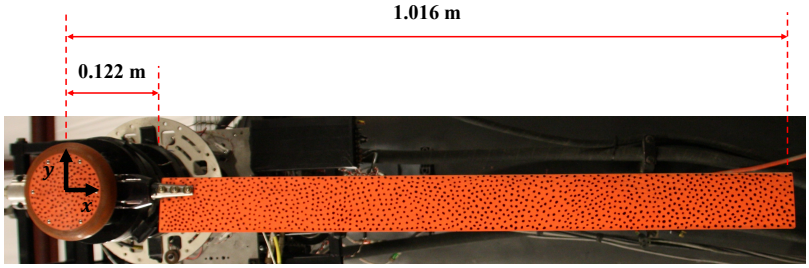

Figure 3.21: Rotor blade painted with orange fluorescent color and black dots

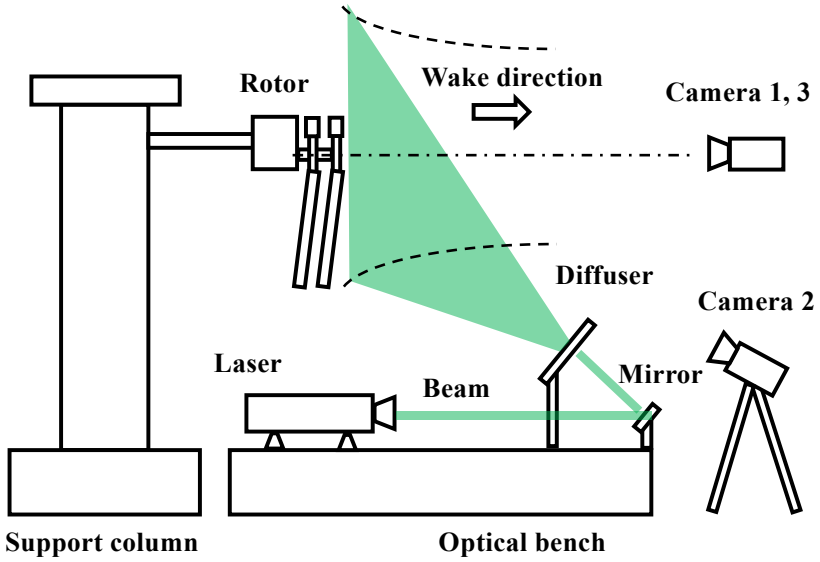

Figure 3.22: A schematic of the DIC measurement setup

3.2.3 DIC post-processing

It should be highlighted here that output data obtained from the commercial DIC software must be post-processed by the analyst to recover the continuous time history of the rotor blade deformation. There are two factors that must be addressed: First, a whole area of each digital image is put into a Cartesian grid and is divided into a number of interrogation windows. Thus, the windows placed over the rotor blade structure do not correspond to the blade-fixed coordinate system, that is, the measurement points are not

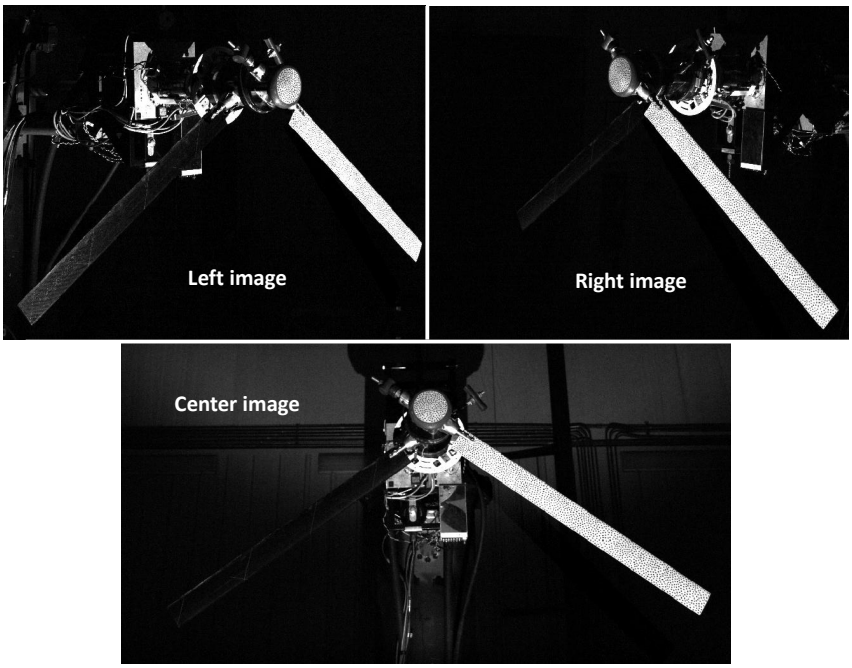

Figure 3.23: Unprocessed images taken simultaneously by the high-speed cameras

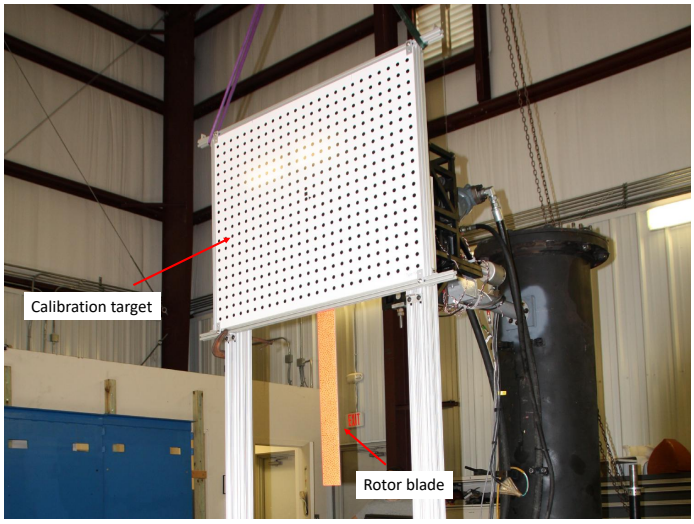

Figure 3.24: Camera calibration setup

uniformly distributed in either chordwise or spanwise direction over the blade structure. Second, output data structure from the software is not organized in time order because the DIC processing in the software is not performed between images taken at different azimuthal locations but performed between images taken at a certain azimuthal location at different time steps. This is because of the fact that in-plane displacements between different azimuthal locations are too large to compute with the DIC algorithm.

To deal with these concerns, output data are first interpolated to a uniform grid over the rectangular blade span with cubic spline function, and the interpolated data structure are reorganized in chronological order. This uniform grid in the blade-fixed coordinate system is used for all the azimuthal locations and time steps. This post-processing enables deformation data analysis from a variety of different perspectives; for example, one can track a single point at the blade tip and plot its displacements as a function of time to examine the temporal trend of the particular point at the tip. Another example could be that the analyst can average the 3D displacements measured at a particular point on the blade over the entire time history to investigate the mean deformation at the point with its standard deviation.

3.3 Test Envelope and Measurement Procedure

With the experimental setups described in § 3.1 and § 3.2, three individual test campaigns were performed in the present study. Test campaign 1 was performed on the small-scale rotor hover test stand, whereas Test cam-

paigns 2 and 3 were performed on the large-scale hover test stand at different rotor configurations and operating conditions. Table 3.5 summarizes the measurement setups of the three test campaigns, and details of each campaign are described in the following subsections.

Table 3.5: Summary of three test campaigns

Campaign	Test scale	Rotor configuration
1	Small	Two-bladed, extremely flexible rotor
2	Large	Single-bladed, single or coaxial rotor
3	Large	Two-bladed, single rotor

3.3.1 Test campaign 1

The main purpose of this campaign was to verify if the methodology of the time-resolved DIC with LIF strobing could be used to measure the small-scale deformation of the extremely flexible rotor blades. The two-bladed flexible rotor was tested at four different blade root pitch angles: 0°, 10°, 20°, and 30°, using the fixed-pitch hubs shown in Fig. 3.1. Additionally, the rotor was spun at four different rotational speeds in each test in order to understand the dynamic behavior of the blade with respect to the rotational speed. For the 0° collective case, the rotor was spun at 600, 900, 1000, and 1500 RPM, whereas for the rest of the test cases the rotor was spun at 600, 900, 1200, and 1500 RPM. The complete test matrix is shown in Table 3.6.

The collective pitch angle was first set by selecting the fixed-pitch hub, and the rotor with the extremely flexible blades was spun at a target rotational speed. Having synchronized the timing of two high-speed cameras and laser

Table 3.6: Summary of the test matrix for Test campaign 1

Condition	Root pitch angle	Ω [RPM]
1	$\theta_0 = 0°$	600, 900, 1000, 1200
2	$\theta_0 = 10°$	600, 900, 1200, 1500
3	$\theta_0 = 20°$	600, 900, 1200, 1500
4	$\theta_0 = 30°$	600, 900, 1200, 1500

strobe, 6400 images were continuously taken at 16 azimuthal locations at each rotational speed. This procedure was repeated for different collective pitch angles. After the collective pitch and rotational speed sweep, undeformed images were taken by rotating the motor by hand slowly (approximately 60 RPM) and used as reference images for the DIC deformation calculation process.

3.3.2 Test campaign 2

During Test campaign 2, the time-resolved DIC blade deformation and rotor loads measurements were performed on the large-scale rotor hover test stand (see § 3.1.2) at several operating conditions. The primary objectives of Test Campaign 2 were: (1) to expand the scale of the time-resolved DIC technique with laser strobing, (2) to simultaneously measure the blade deformation and rotor loads, and (3) to correlate these experimental results with a numerical model. First, the single-bladed, isolated single rotor balanced by a counter-weight was tested at a slightly negative collective pitch angle to produce almost zero mean thrust. In this condition, the wake was in close proximity to the rotor blades so that the force on the rotor blade was dominated by unsteady random excitation, which is one of the conditions needed for

operational modal parameter identification. Then, the single-bladed isolated rotor was tested at a moderate thrust, where the rotor produced 70 N corresponding to a blade loading coefficient of $C_T/\sigma = 0.07$. For all test conditions, the rotational speed Ω was set at 900 RPM.

Additionally, the single-bladed CCR rotor system, shown in Fig. 3.3a, was tested at a mean thrust of the lower rotor of 90 N ($C_T/\sigma = 0.09$). This rotor configuration was also spun at 900 RPM and the coaxial system was trimmed to maintain torque balance. Note that a mean torque of both rotors was set to be approximately 9.0 N-m and a mean thrust of the upper rotor was 124 N at this operating condition. For all of the test cases, both the blade deformation and rotor loads were simultaneously measured in the rotating frame. Three-dimensional deformation of the rotor blade was calculated at a total of 2020 (20 chordwise and 101 spanwise) locations with the size of the interrogation window being 21 pixels $\times$ 21 pixels. Since the digital pulse train for triggering camera shutter was downsampled to 32/rev and the nominal rotational speed was 900 RPM (15 Hz), the sampling rate of the time-resolved DIC measurement was 480 Hz. At each test condition, images were continuously recorded over 300 rotor revolutions yielding 9600 images per camera over 20 seconds. Due to the geometrical constraints of the experimental setup, the blade deformation measurement was performed on the lower rotor only. All the operating conditions tested during the Test campaign 2 are summarized in Table 3.7.

Table 3.7: Summary of operating conditions for Test campaign 2

Condition	Rotor	C_T/σ	Ω [RPM]
1	Isolated single	0	900
2	Isolated single	0.07	900
3	CCR	0.09 (lower rotor)	900

3.3.3 Test campaign 3

Test campaign 3 was an extension of the second test campaign. The main purpose of this test campaign was to apply a variety of rotor pitch angle control inputs to the 2 m-diameter, large-scale rotor in hover and evaluate if the rotor loads estimation methodology developed in the dissertation could be used in different operating (loading) conditions. To achieve the goal, several improvements were made on the rotor configuration, pitch angle control system, and DIC measurement setup.

While the single-bladed, single or CCR rotor with the lead-screw pitch actuation system was used during the second test campaign, the two-bladed, isolated single rotor with the hydraulic pitch actuation system was used during Test campaign 3. The two-bladed rotor stand and its hydraulic actuation system are shown in Fig. 3.3b and 3.12, respectively. The hydraulic servo actuators enabled three different rotor pitch control inputs: (1) a steady collective pitch input at a blade loading (C_T/σ) of 0.125, (2) a lateral cyclic pitch input ($\theta_{1C} = 2°$), and (3) a collective step pitch input (2° step function). For all of these conditions, the rotor was spun at 900 RPM. As was the case of Test campaign 2, the blade deformation time history and rotor loads were simul-

taneously measured at each operating condition. These three test conditions are summarized in Table. 3.8.

Table 3.8: Summary of operating conditions for Test campaign 3

Condition	C_T/σ	Trim	θ_0	θ_{1c}
1	0.125	Constant pitch	9°	-
2	0.125	1/rev pitch	9°	2°
3	-	Step pitch	9° + 2° step	-

Regarding the DIC measurement setup, a new stereoscopic camera system was used for Test campaign 3 as shown in Fig. 3.25. The major difference from the second test campaign was the orientation of the laser beam with respect to the rotational axis. As compared to the schematic of the DIC measurement during Test campaign 2 (see Fig. 3.22), the center axis of the diffused laser beam was aligned to the rotational axis of the rotor stand, resulting in a uniform distribution of the illumination intensity over the whole rotor disk which improved the quality of images and DIC post-processing.

Multiple independent experiments were performed to assess repeatability for each test condition. Data obtained during the tests 1 and 2 can be phase-averaged over revolutions because the rotor was controlled by a steady collective pitch input or a lateral 1/rev periodic pitch input. This phase-averaging process is based on the assumption that the mean of each revolution is treated as a statistically independent measurement sample. The standard deviation of the sample is used to compute precision uncertainty of measured quantities.

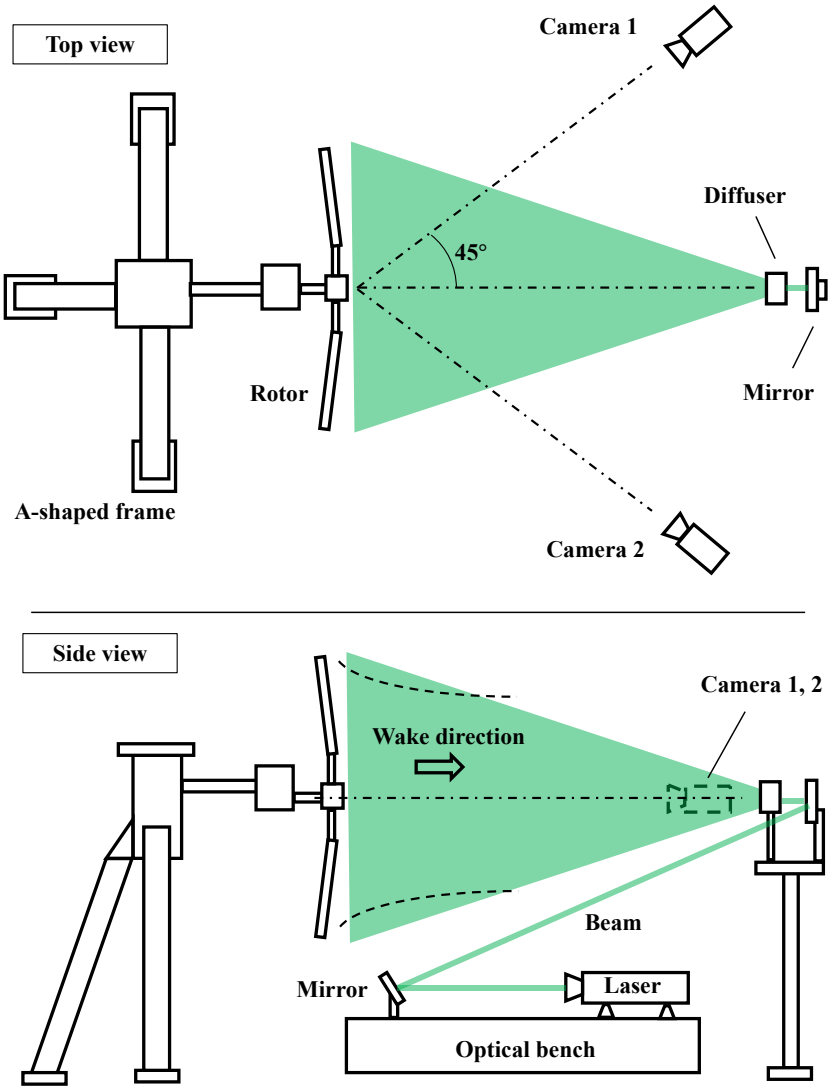

Figure 3.25: A schematic of stereoscopic camera arrangement used during Test campaign 3

On the other hand, three independent data sets were obtained for the test condition 3, each recorded with the digital pulse triggering the step pitch

actuation. The initial intention was to use the trigger as a reference point for phase-averaging data sets taken from multiple individual experiments; however, the pitch angle responses were not consistent over the three experiments. Figure 3.26 shows the pitch angle variations, measured by the AMR root pitch angle sensors, for three independent measurements. The rise time of the collective increase and the time lag between the trigger and blade pitch increase were calculated to be approximately 200 and 75 milliseconds for all the three different experiments, respectively. However, the magnitudes of the pitch angle response were not consistently maintained; for example, the blade pitch was changed from 9.5° to 11.5° during the first experiment, whereas the pitch angle was changed from 9.5 ° to 11.0° during the second experiment as shown in Fig. 3.26. Hence, phase-averaging was not performed on the measured quantities for the test condition 3, and results from the first experiment at which the blade pitch successfully responded to the 2° collective step pitch input will be primarily discussed in this dissertation.

Table 3.9: Summary of the design parameters for digital low-pass filters

Parameter	Low-pass filter
Type	IIR
Domain	Time
Passband ripple	0.5 dB
Design method	Chebyshev type I

Instead of phase-averaging, data measured during the step pitch input operation were processed by digital low-pass filters. The design parameters for the low-pass filter are summarized in Table 3.9. Different cut-off frequen-

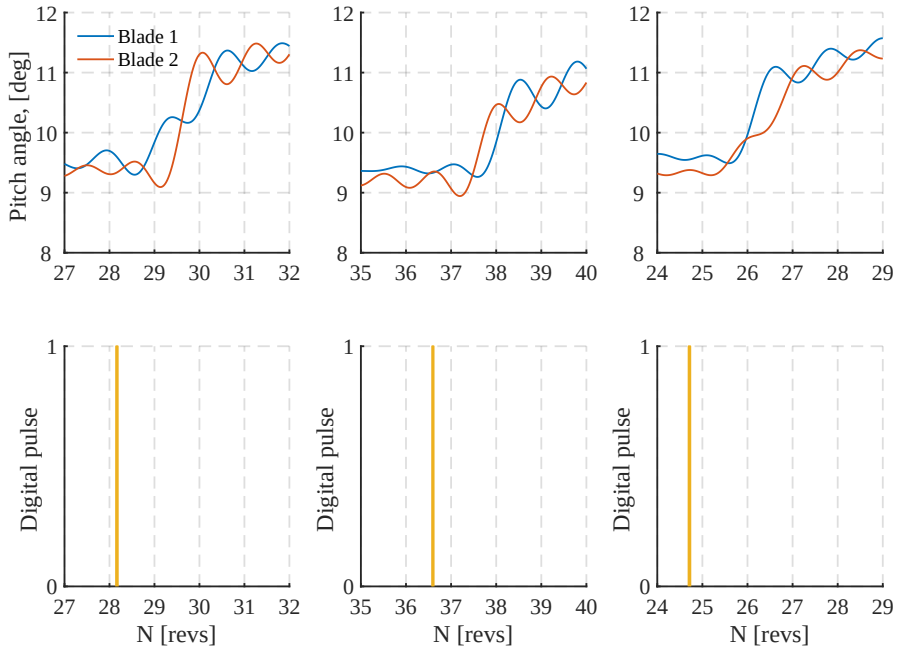

Figure 3.26: Pitch angle variations and the initial digital trigger timing obtained from the three independent measurements

cies were selected for each measured quantity, thus, the actual frequencies used for this filtering process will be described along with experimental results in the next chapter. Since an IIR low-pass filter introduced a frequency-dependent delay and phase shift between input and output signals, a specific post-processing algorithm was applied to the output signal in time domain to compensate for the delays. The algorithm essentially applies the digital low-pass filter to the input data in both the forward and backward directions in time to remove the delay.

In summary, this chapter covered the details of the hover test stands,

the blade deformation measurements using the time-resolved DIC, the rotor loads measurements, and the test envelopes and procedures for the small- and large-scale rotor configurations.

Chapter 4

Results and Discussion

This chapter discusses the results of the rotor blade deformation measurements, the operational modal identification, and the rotor loads estimation for several different rotor systems and operating conditions. First, the results of the time-resolved DIC deformation measurements performed on the small- and large-scale rotor test rigs (see chapter 3) are discussed in § 4.1. Second, the rotor blade modal characteristics identification with several OMA algorithms based on the blade deformation time history are described in § 4.2. Finally, the results of the rotor loads measurements and estimation are summarized in § 4.3. A block diagram shows the organization of this chapter in Fig. 4.1.

4.1 Rotor blade deformation measurement

Results of blade deformation measurements are presented in the following order: (1) the small-scale DIC measurement on the 0.45 m-diameter,

Portions of this chapter were previously published as "Blade Passage Loads and Deformation of a Coaxial Rotor System in Hover" [57] in the AIAA Journal of Aircraft and "Full-field optical deformation measurement and operational modal analysis of a flexible rotor blade" [75] in the Journal of Mechanical Systems and Signal Processing. All writing and figures included in this chapter are the original work of the author, incorporating computational data from Dr. Roland Feil and Dr. Juergen Rauleder, with editing by Dr. Jayant Sirohi.

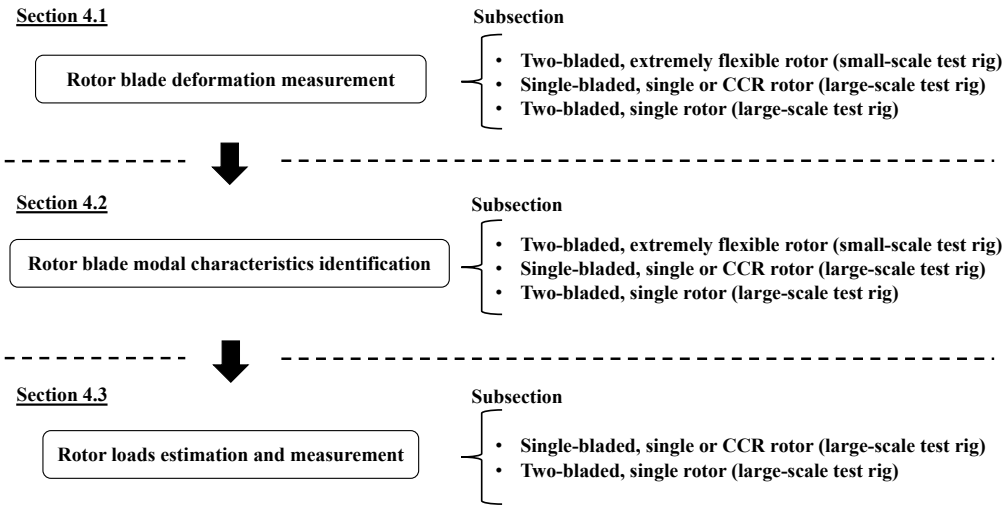

Figure 4.1: A diagram of the organization of this chapter

two-bladed, extremely flexible rotor in § 4.1.1 and (2) the large-scale DIC measurement on the 2.0 m-diameter, single-bladed or two-bladed, single or coaxial rotor in § 4.1.2. The goals of these measurements were to verify and validate if the time-resolved DIC technique with laser strobing and fluorescence paint, developed in the dissertation, could be applied to different measurement scales, rotor configurations, and operating conditions. Note that the correctness of the 3D DIC deformation in static, non-rotating frame has been proved by comparing results with those obtained by a laser displacement sensor, as thoroughly described in [70].

4.1.1 Small-scale rotor

Figure 4.2 and Table 4.1 shows a recap of the rotor setup and test matrix used for this small-scale DIC test, respectively. The blade deformation measurements were performed at four different blade root pitch angles and rotational speeds during Test campaign 1 (see in § 3.3).

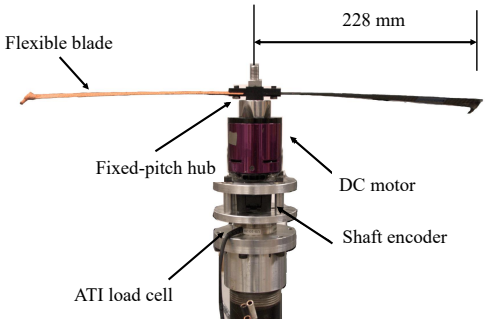

Figure 4.2: Recap: Side view of the rotor test article

Table 4.1: Recap: Summary of the test matrix for Test campaign 1

Condition	Root pitch angle	Ω [RPM]
1	$\theta_0 = 0°$	600, 900, 1000, 1200
2	$\theta_0 = 10°$	600, 900, 1200, 1500
3	$\theta_0 = 20°$	600, 900, 1200, 1500
4	$\theta_0 = 30°$	600, 900, 1200, 1500

Figure 4.3 shows the flap bending deformation of the rotor blade at 30° root pitch angle spun at 1200 RPM over one revolution. Note that images were continuously taken over 400 revolutions at 16 evenly-spaced azimuthal locations, yielding 6400 images per camera at each test condition. The variation of the blade flap bending over one revolution shown in Fig. 4.3 was obtained

by three steps: (i) The time history of blade deformation over 400 revolutions was phase-averaged to yield the mean blade bending deformation as a function of radial station at each of the 16 azimuthal locations. (ii) Displacement vectors along the quarter-chord axis were extracted from the phase-averaged data set. (iii) Data was interpolated between adjacent azimuthal angles, yielding the out-of-plane bending deformation over the entire rotor disk; note that the phase-averaging process eliminates most of the stochastic noise in the measurement.

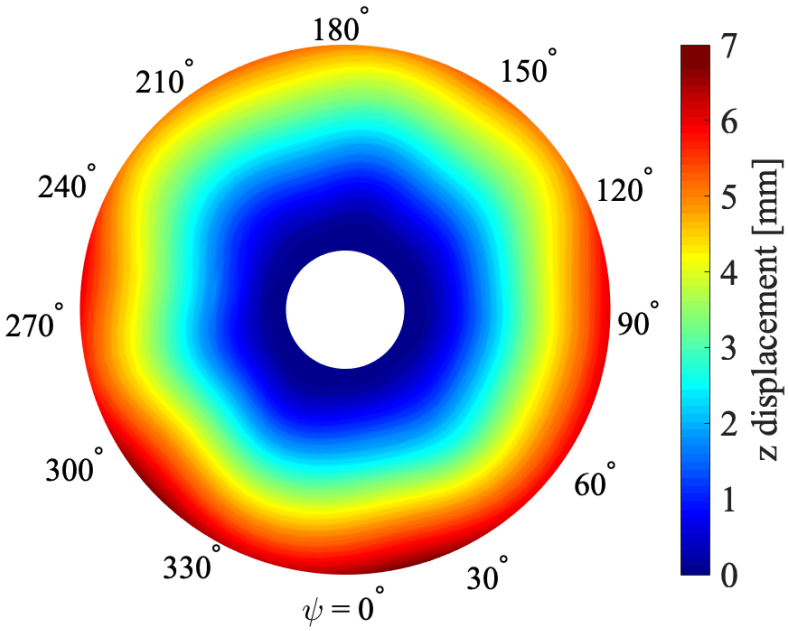

Figure 4.3: Flap bending deformation over the rotor disk at $\theta_0 = 30°$

The rotor blade at a root pitch angle of 30° experienced a positive flap bending deformation, increasing along the radial direction, and reached approximately 7 mm at the blade tip. The contour plot shown in Fig. 4.3 clearly

presents the azimuthal variation of the blade flapping motion, regardless of the fact that blade pitch angle was fixed at the root. Over the range between $\Psi = 0^\circ$ and 180°, the blade continuously flapped down from 7 mm to 4.5 mm measured at the tip and started flapping up during the other half of the revolution. This 1/rev motion was possibly caused by the combination of three major factors: (i) the extreme torsional flexibility of the rotor blade structure, (ii) no active stabilization mechanism, and (iii) some mean asymmetric air flow in the test chamber due to flow recirculation. Although there was a passive stabilization control system (i.e., a blade tip mass inducing propeller moment as shown in Fig. 3.2), the rotor blade experienced significant elastic twist due to the low blade torsional rigidity, resulting in azimuthal variation of blade sectional angle of attack.

From the phase-averaged deformation over one revolution, the mean flap bending, lead-lag bending, and torsional deformation at the blade quarter-chord were calculated; these correspond to the static equilibrium deformation of the rotor blade. While the flap bending and lead-lag bending were measured from the (non-rotating) reference state of the blades, the torsional deformation was obtained by calculating slopes of the blade chord between deformed and undeformed images at each spanwise measurement channel (76 spanwise locations). Figure 4.4a to 4.4c shows the static deformation of each degree of freedom of the rotor blade at 30° root pitch angle, spinning at four rotational speeds. As the rotational speed increased, the magnitude of both flap and lead-lag bending increased, which was due to the increase in lift and drag, re-

spectively. The negative twist along the rotor blade increased with rotor speed due to the centrifugal moments on the tip mass; at 600 RPM, the blade had a spanwise nose-down twist of about 1°, whereas at 1500 RPM it increased to a nose-down twist of nearly 10°. The increase in pitch angle at the blade tip is due to the presence of the tip mass. The shaded area in Fig. 4.4a to 4.4c represents the estimated DIC measurement uncertainty based on the standard deviation and the size of interrogation window as specified in the software documentation.

During the hover testing, instabilities were observed at some operating conditions. Figure 4.5 shows the pitch angle displacement at the tip of the blade as a function of time, measured at different operating conditions. At 600 RPM, the amplitude of pitch angle displacements at $\theta_0 = 0°$ and 30° are much greater than at the other two root pitch angles, indicating the flutter-type instability that occurred at these operating conditions. On the other hand, as shown in Fig. 4.5b, the amplitudes of the tip pitch angle variation at 1500 RPM for all three cases are small, indicating stable regimes.

As described in chapter 3, the current study upgraded the conventional DIC technique for rotating rotor blade deformation measurement by combining the following features: expansion of camera field of images to the entire rotor disk, Laser-Induced Fluorescence (LIF) technique to obtain high contrast images, and camera shutter and laser strobing synchronization using a rotary encoder. The results shown in this subsection prove that the new, time-resolved DIC technique developed in this dissertation can be used to measure

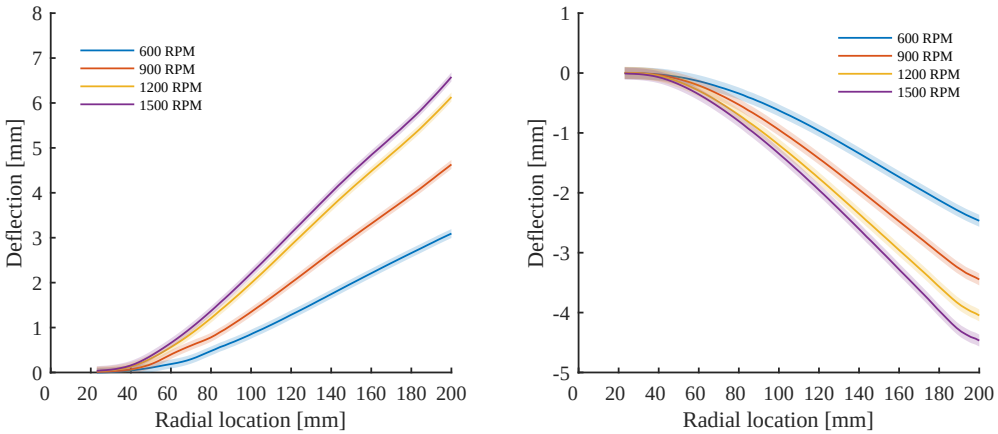

(a) Flap bending deformation

(b) In-plane deformation

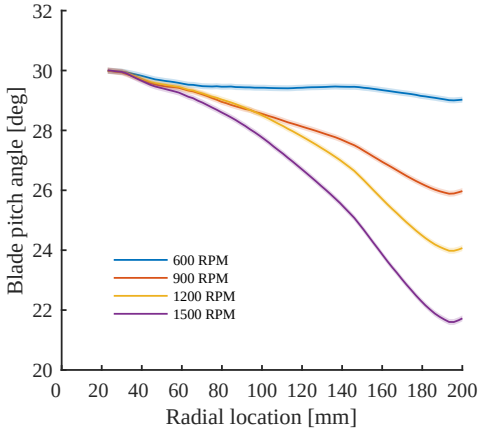

(c) Sectional blade pitch angle

Figure 4.4: Static blade deformations of each degree of freedom, along the blade quarter-chord axis at 30° root pitch and different rotational speeds

deformation time history of the small-scale (0.46 m-diameter) rotor blade at different operating conditions on the order of a few millimeters.

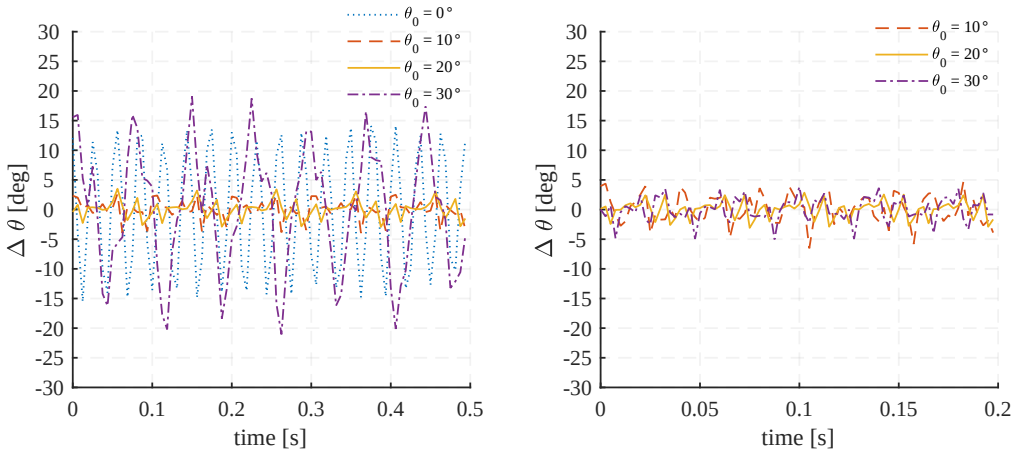

(a) Rotor spun at 600 RPM

(b) Rotor spun at 1500 RPM

Figure 4.5: Time history of the pitch angle displacement at the blade tip for different root pitch angles

4.1.2 Large-scale rotor

Now, to expand the applicability of the time-resolved DIC technique, several measurements were performed on the large-scale rotor hover test rig at different rotor configurations and operating conditions. The large-scale (2 m-diameter) test rig can be configured to the single-bladed or two-bladed, isolated single or CCR rotor system as shown in Fig. 3.3.

First, the results of the blade deformation measurements performed on the single-bladed CCR rotor during Test campaign 2 are presented along with numerical predictions provided from research collaborators at the Technical University of Munich; these predictions are described in detail in Ref. [57]. The primary goal of the testing was to verify if the time-resolved DIC technique developed in this dissertation can be applied to the large-scale rotor blade

deformation measurements, by comparing the experimental results with the numerical predictions. Note that the blade structural properties (the bending and torsional stiffness) used in the numerical modeling were obtained from multiple DIC deformation measurements in the non-rotating frame, resulting from static loadings in out-of-plane, in-plane, and torsional degrees of freedom. Further details of the structural characteristics identification can be found in Ref. [70].

Next, results from additional measurements performed on the two-bladed isolated single rotor during Test campaign 3 are discussed. The purpose of the additional measurements was to apply a variety of pitch angle control inputs to the large-scale rotor and demonstrate if the DIC technique is able to capture the dynamic resultant motion of the rotating blade responding to different rotor loading conditions. Measurement procedures and test envelopes on the large-scale test rig are summarized in § 3.3.

4.1.2.1 Single-bladed CCR rotor (Test campaign 2)

The single-bladed CCR rotor system, shown in Fig. 4.6 as a recap, was tested at a mean thrust of the lower rotor of 90 N ($C_T/\sigma = 0.09$). The DIC deformation measurements were carried out only on the lower rotor of CCR system (the orange-painted blade shown in Fig. 4.6), due to the geometrical limitation of experimental setup. This rotor was spun at 900 RPM and the coaxial system was trimmed to achieve torque balance, that is, the total yaw moment was trimmed to be zero.

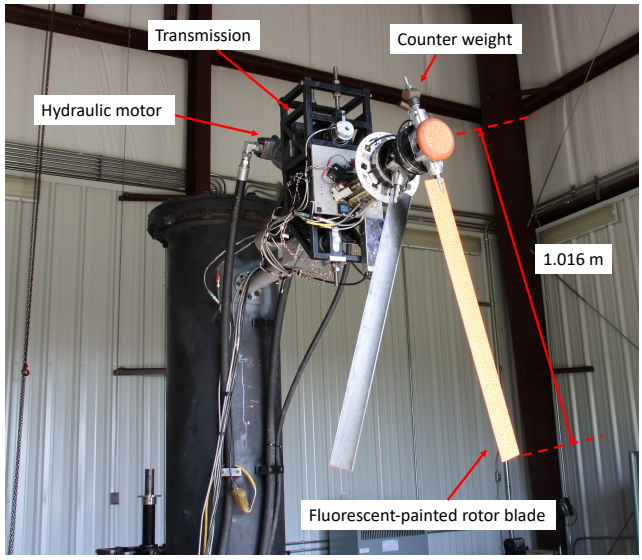

Figure 4.6: Recap: Single-bladed, CCR rotor configuration

The measured and predicted out-of-plane lower rotor blade deformation over the entire rotor disk at a blade loading of 0.09 ($C_T/\sigma = 0.09$) are shown in Fig. 4.7a and 4.7b, respectively. Figure 4.7a were obtained by the same processing method as the contour plot shown in Fig. 4.3 in the small-scale DIC measurement. Overall, there was excellent agreement between the measured and predicted flap bending (out-of-plane) deformation. The blade tip deflection reached 75 mm, which is approximately 10 times larger than the tip deflection that the small-scale, 0.46 m-diameter rotor experienced. Considering the fact that the radius of the large-scale rotor is 1.016 m, which is also 4.45 times larger than that of the small-scale rotor, the time-resolved DIC successfully demonstrates its capability of measuring out-of-plane deformation time history of a rotating blade at different measurement scales.

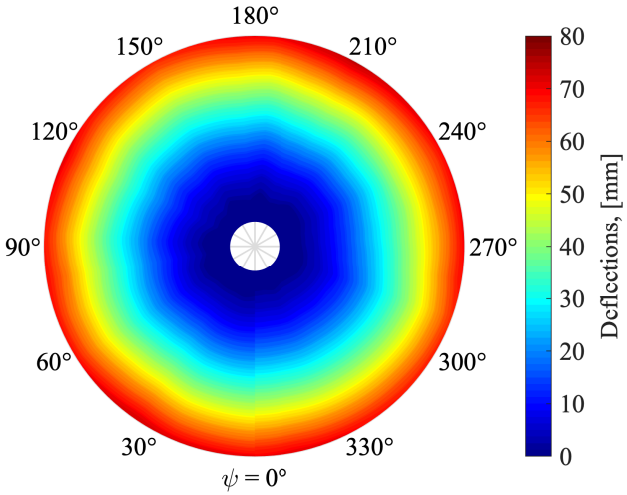

(a) Measured CCR lower rotor blade flap bending deformation

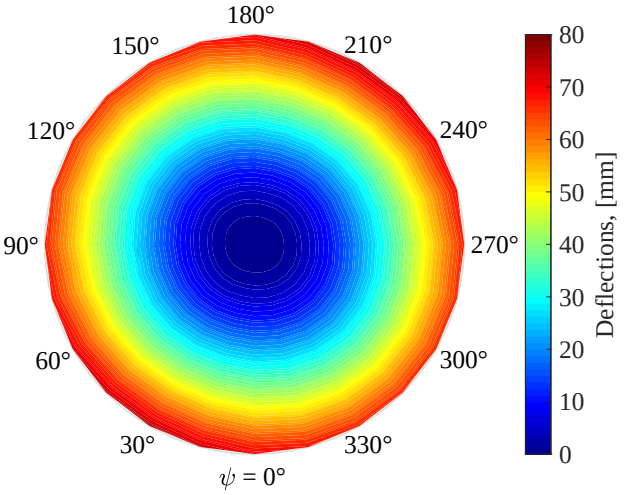

(b) Predicted CCR lower rotor blade flap bending deformation

Figure 4.7: Flap bending deformation of the CCR lower rotor blade at $C_T/\sigma = 0.09$

Figure 4.8 shows the measured and predicted CCR lower rotor blade tip displacement extracted at the blade quarter chord location as a function of azimuthal angle at $C_T/\sigma = 0.09$. The trend revealed the significant 2/rev characteristics, that are associated with the blade crossings located at $\psi = 0°$ and 180°. This 2/rev characteristic reflects the lower rotor blade response to the transient loads generated by the upper–lower rotor blade crossing. For this investigated thrust level (i.e., a blade loading coefficient of $C_T/\sigma = 0.09$), vibrations around the mean deflection of 69.6 mm occurred with a maximum deflection of 74.6 mm and a minimum deflection of 66.4 mm. The maximum peaks of blade tip deflection were seen at approximately $\psi = 30°$ and 210°, whereas the minimum peaks were observed at approximately $\psi = 150°$ and 290°. The 2/rev half-peak-to-peak magnitudes of 4.1 mm corresponded to 5.9% of the mean deflection. Predicted results correlated satisfactorily with these measurements in both magnitude and phase. The numerical predictions showed that the upper rotor blade had a greater mean deformation, which is consistent with its greater thrust share compared to the lower rotor in a torque-balanced trim condition.

Figure 4.9 shows the measured and predicted blade deformation of the lower rotor in the coaxial system along the blade quarter-chord axis as a function of radial station. The two lines correspond to the azimuthal locations of maximum and minimum tip deflection that were previously determined from Fig. 4.8. There was excellent agreement between the measured and predicted flap bending (out-of-plane) deflection, with the largest discrepancy limited to

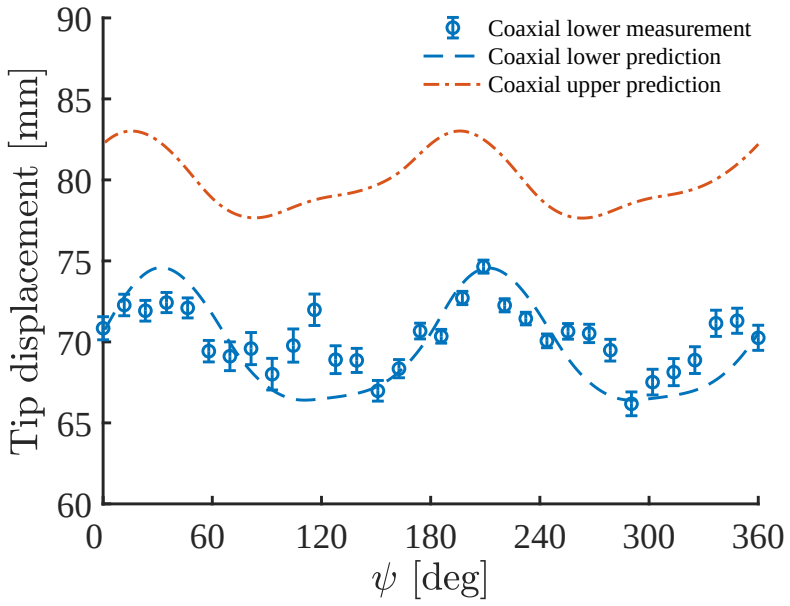

Figure 4.8: Lower rotor blade tip displacement comparison between measurement and prediction

less than 3% (2.5mm) at the approximately 55% of the radial station on the minimum deflection curve. Those errors were also more apparent over the inboard portion due to smaller magnitude deflections.

The phase lag between the maximum and minimum deflection and the blade crossings (i.e., $\psi = 0°$ and 180°), shown in Fig. 4.8, can be explained by the influence of rotor blade bound circulation. As the upper and lower rotor blades approach each other, the bound vortex on one blade induces interactional upwash on the other blade, resulting in an increase in effective angle of attack of the other blade, as shown in Fig. 4.10. The increase in angle of attack causes a 2/rev flap bending deflection of the rotor blade. Aerodynamic

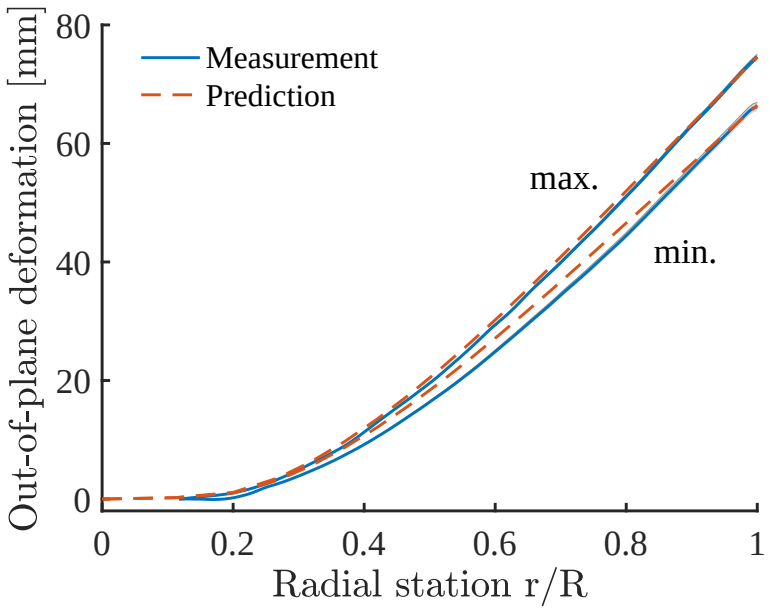

Figure 4.9: Maximum and minimum flap bending deformation of the lower rotor blade as a function of blade radial station at $C_T/\sigma = 0.09$

angles of attack increase up to the azimuthal angle of blade crossing, reach a peak just before crossing, and eventually drop to a minimum after blade passage due to the change in sign of interactional induced velocity (upwash to downwash). These blade deformation measurements indicate that the transient vibration of the coaxial rotor system is due to the interaction mechanism of blade bound circulation.

Over all, the large-scale time-resolved DIC measurements were successfully carried out on the single-bladed coaxial lower rotor with good agreement between the experimental and numerical results. Additionally, the measurement data revealed the significant 2/rev, transient response of the rotor blade

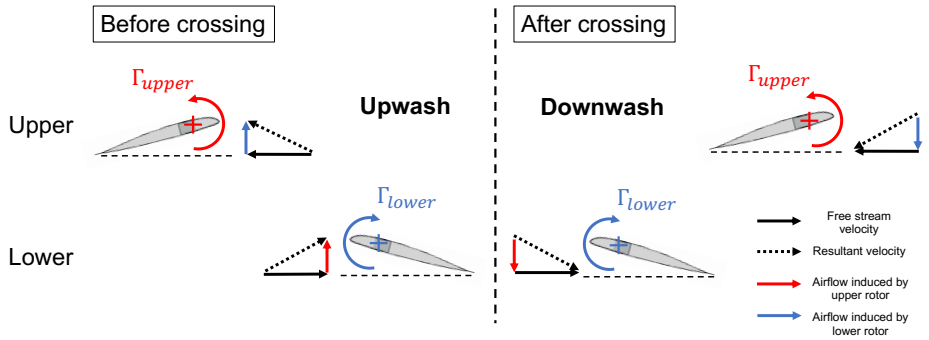

Figure 4.10: Interaction of blade bound circulation in the CCR rotor system

due to the blade crossings in the CCR rotor system, which could only be identified by analyzing the continuous time history of the blade deformation.

4.1.2.2 Two-bladed single rotor (Test campaign 3)

In addition to the blade deformation measurements on the single-bladed coaxial rotor system as described above, the time-resolved DIC technique was used to measure the blade responses to a variety of rotor loading conditions during Test campaign 3. The large-scale rotor was reconfigured to the two-bladed, isolated single rotor with the hydraulic actuation system as shown in Fig. 4.11 as a recap from chapter 3. The hydraulic servo actuators enabled three different rotor pitch control inputs: (1) a steady collective pitch input at a blade loading (C_T/σ) of 0.125, (2) a lateral cyclic pitch input ($\theta_{1C} = 2°$), and (3) a collective step pitch input (2° step function). For all of these conditions, the rotor was spun at 900 RPM. Details of the hydraulic, high-speed rotor pitch actuation system are available in § 3.1.2.

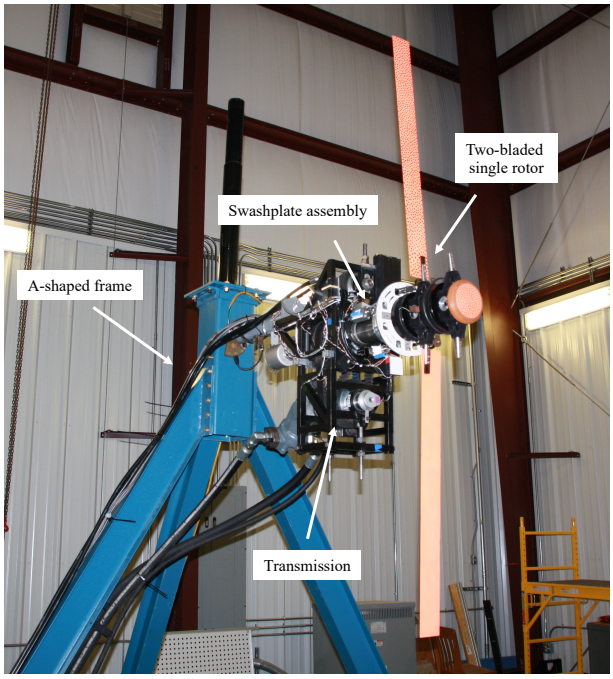

Figure 4.11: Recap: Two-bladed, isolated single rotor configuration

The first operating condition tested on the two-bladed single rotor was a steady collective pitch input ($\theta_0 = 9°$) at a blade loading C_T/σ of 0.125. The deformation measurement was carried out on one of the two rotor blades during this test campaign. Note that the deformation data shown in the current section were computed based on the averaged reference image taken at the blade root pitch angle of 0°, spun at the same rotational speed of 900 RPM.

First, the out-of-plane blade deformation over the entire rotor disk is shown in Fig. 4.12. The flap bending deflection reached nearly 90 mm at the blade tip with little azimuthal variation. The axisymmetric trend represents

the fact that the constant collective pitch angle of 9° was properly applied to the rotor and steady-state loading over the rotor disk was achieved. The phase-averaged blade tip displacement over one revolution was then extracted from the contour plot and is shown in Fig. 4.13, representing the data both from the 32 measurement points and from the spline interpolation. A slight fluctuation over the entire range was clearly observed in Fig. 4.13, especially over the range from 60° to 180° where a large rise-and-fall between 85 mm and 95 mm occurred. One possible cause of this dip is that one of three hydraulic servo actuators might have had non-ideal free-play in the linkage path, such as a rod end, resulting in the ± 5 mm fluctuation that periodically occurred over the range.

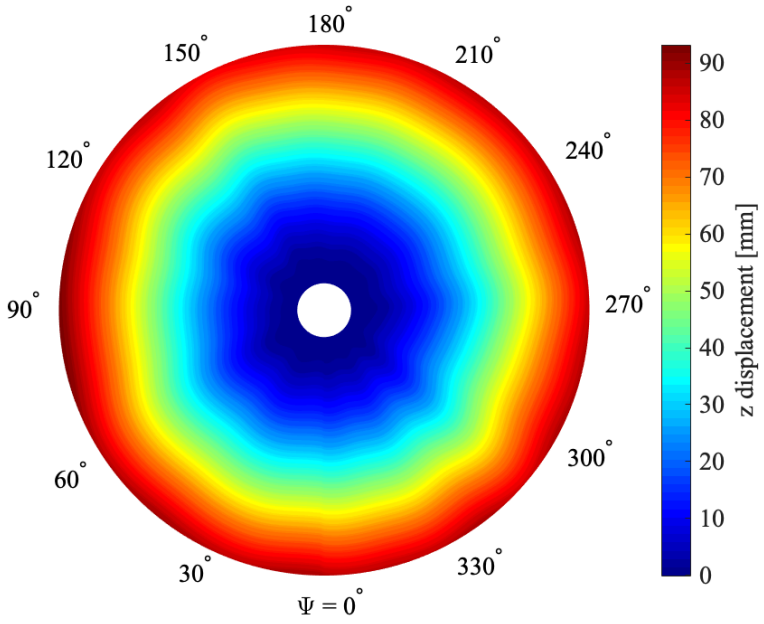

Figure 4.12: Out-of-plane blade deformation over the entire rotor disk

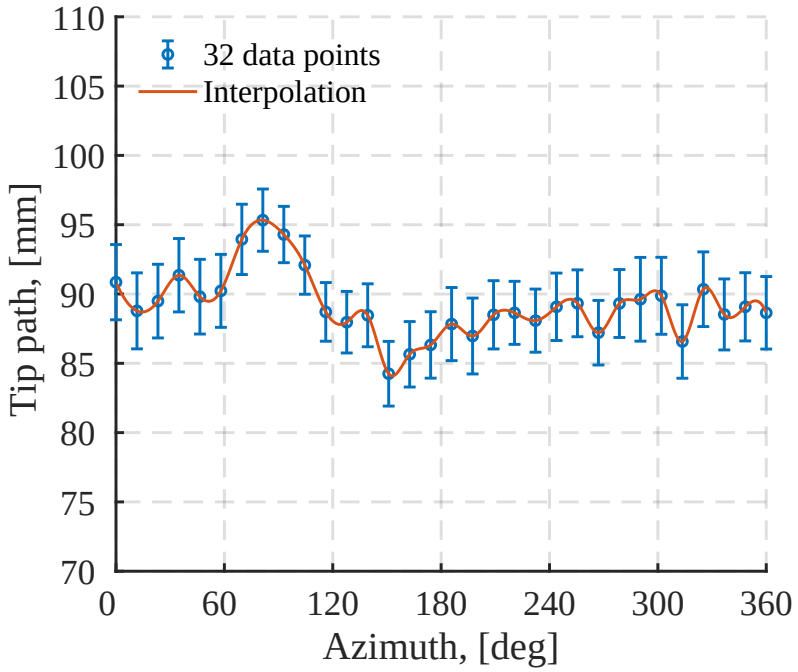

Figure 4.13: Blade tip displacement as a function of azimuthal angle

Recall that one of the advantages of the DIC technique is that it can measure the three-dimensional (3D) full-field deformation on the surface of a target structure. Figure 4.14 shows the 3D static deformation distributed over the blade span. This 3D deformation with high spatial resolution cannot be obtained if conventional on-blade sensors, that can only perform pointwise measurements, are used. From the 3D plot, deformations of each degree of freedom (flap, lead-lag, and torsion) along the quarter-chord axis were extracted and plotted in Fig. 4.15.

The spanwise variations of the blade flap and lag deformation shown in Fig. 4.15a and 4.15b represent the out-of-plane and in-plane static deflection at

the given rotor pitch angle and rotational speed, respectively. One can clearly see a flap-up and lagging motion corresponding to increase in lift and drag forces as the blade angle of attack increases. While the flapwise and chordwise deformation along the blade quarter-chord axis was directly interpolated from the 3D distributed plot, the sectional blade pitch angle, shown in Fig. 4.15c, was obtained based on the 1st-order polynomial fitting to the 3D surface height distribution at each spanwise station. The relationship between the sectional pitch angle and the slope of the fitting is as follows:

$$\begin{aligned} w_i(y_i) &= P_1 y_i + P_0 \\ \theta_i &= \arctan P_1 \end{aligned} \tag{4.1}$$

where w_i, y_i, and θ_i are out-of-plane displacement, chordwise location, and local torsional deformation at a spanwise station i, respectively. P_1 and P_0 represent the slope and y-intercept of the 1st-order polynomial fit.

As can be seen in Fig. 4.15c, the elastic twist of the rotor blade was small, considering the fact that the blade root pitch was trimmed to the mean collective angle $\theta_0 = 9°$ measured in real time using the AMR sensor (see § 3.1.2). There was a dip observed in regions of the blade tip, however, its magnitude was within a fraction of a degree and on the same order of measurement uncertainty. Note that highlighted areas in these plots represent uncertainties of each measured quantity.

For the second operating condition employed during Test campaign 3, the rotor was trimmed at a steady collective pitch + a lateral cyclic pitch.

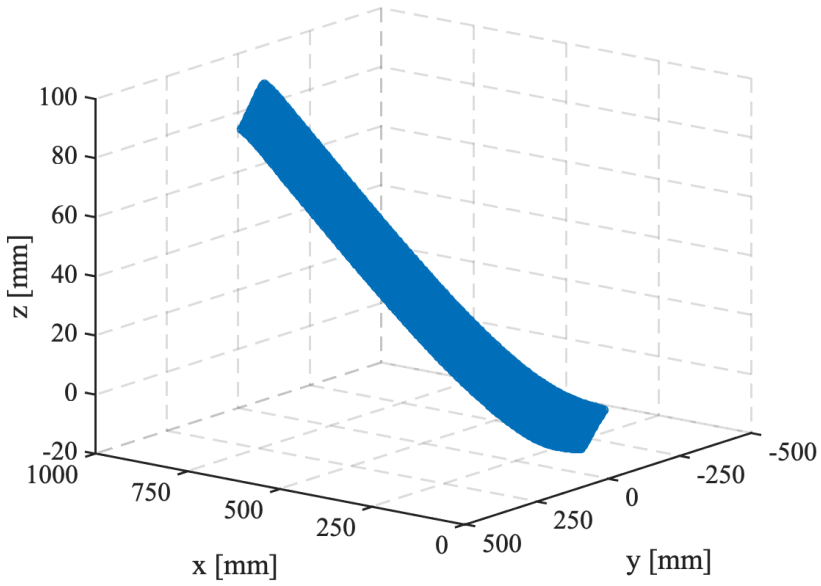

Figure 4.14: 3D static deformation distributed over the entire blade span

The collective pitch was adjusted so that the mean blade loading of this test condition remained the same as for the first operating condition ($\theta_0 = 9°$). The lateral cyclic pitch θ_{1C} was set to be $\pm 2°$, by introducing a swashplate inclination with the hydraulic-driven actuators. Rotor track was achieved using the real-time hub loads measurement, specifically hub pitching and rotating moment in the rotating frame.

The contour plot in Fig. 4.16 shows the phase-averaged flap bending deformation over one revolution. Due to the lateral pitch input and the gyroscopic phase shift, the whole rotor disk tilted in the lateral direction. This behavior was more pronounced in the blade tip displacement, as shown in Fig. 4.17. The sinusoidal motion over one revolution as well as the phase shift

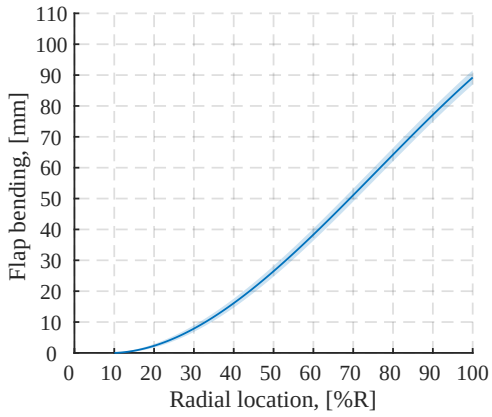

(a) Out-of-plane deformation

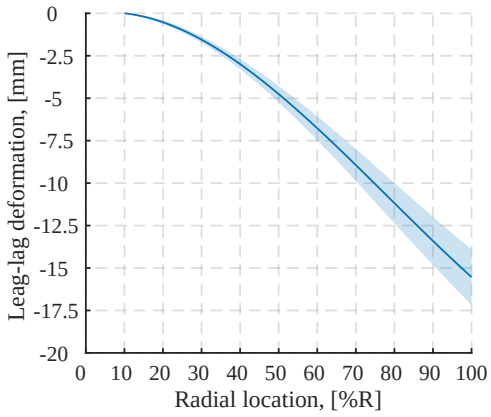

(b) In-plane deformation

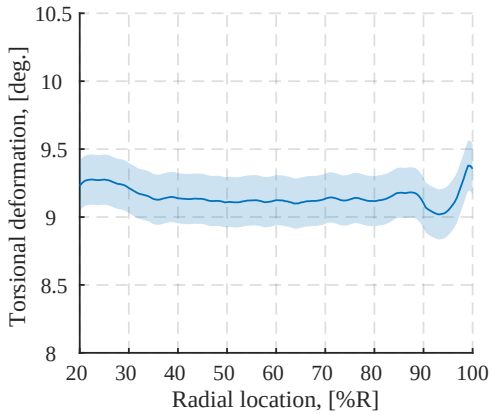

(c) Torsional deformation

Figure 4.15: Static blade deformations of each degree of freedom, along the blade quarter-chord axis

can be clearly seen in the tip displacement.

In Fig. 4.17, the maximum flap bending deflection occurred at the azimuthal angle of 250°, whereas the minimum occurred at 60°. The tip deflection difference between the maximum and minimum reached approximately 75 mm. In other words, it was demonstrated that this large sinusoidal oscillatory

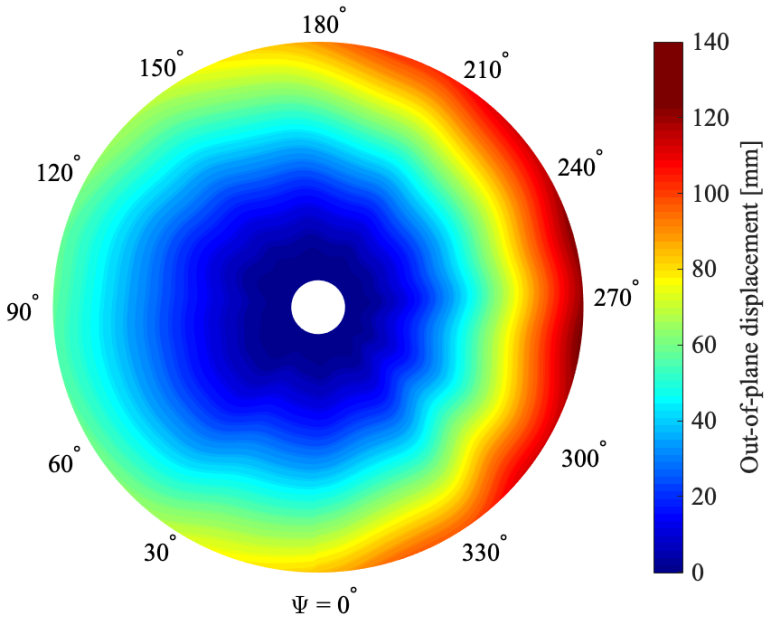

Figure 4.16: Out-of-plane blade deformation over the entire rotor disk for the lateral pitch angle input

motion of the 2 m-diameter rotor at 1/rev frequency (15 Hz) was successfully captured by the DIC technique.

The last operating condition tested during Test campaign 3 was a collective step change input. The rotor pitch angle was first set to be at a constant collective angle $\theta_0 = 9°$, corresponding to the blade loading (C_T/σ) of 0.125. Once the rotor reached a steady-state condition, the collective pitch was rapidly increased by approximately 2° to examine the rotor transient responses to the dynamic pitch control from an aeroelastic perspective. This type of step (practically ramp) pitch input excites the structure such that the responses at different modal frequencies could be studied, and may help to extract higher

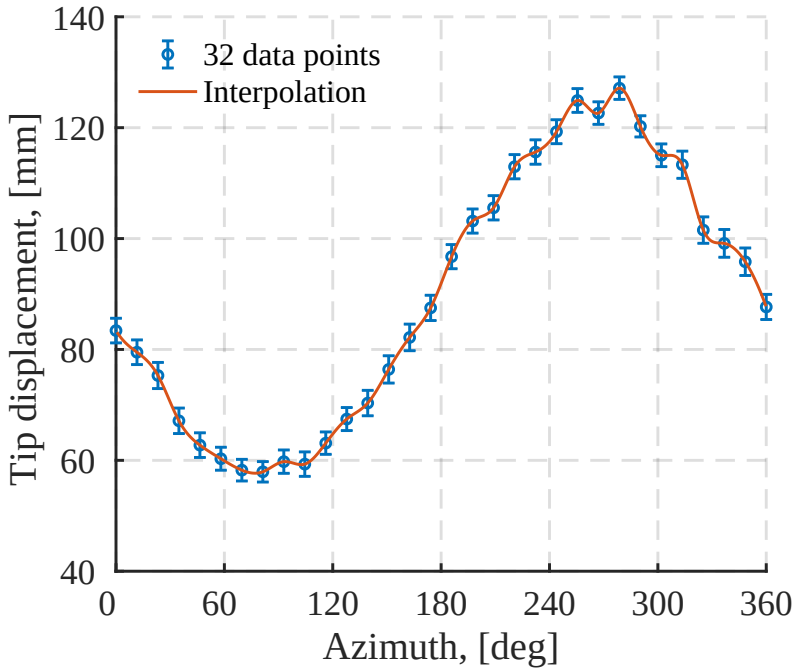

Figure 4.17: Blade tip displacement as a function of azimuthal angle for the lateral pitch angle input

modes with the operational modal analysis. As for the other test conditions, the time history of the rotor blade deformation during the collective step pitch input was measured using the time-resolved DIC technique.

Figure 4.18 represents the rotor blade deformation of each degree of freedom (flapwise, chordwise, and torsional deformation) measured at the tip as a function of the number of revolution. To clearly observe the effect of the step input on the blade dynamics, a low-pass filter was applied to the measured blade deformation with a 3dB cutoff frequency of 13 Hz. Note that the cutoff frequency was manually selected by trial-and-error process. These responses

were initiated during the 28th revolution and the rise time of the blade flap, lag, and torsion was computed to be about 280 milliseconds (4.2 revolutions) from Fig 4.18a to 4.18c.

Due to the step change, the resultant flapwise deflection at the blade tip increased by 20 mm and reached nearly 115 mm in Fig. 4.18a. The step response in chordwise degree of freedom due to the pitch angle change was also observed, and the change was approximately 10 mm according to Fig. 4.18b. Additionally, the local pitch angle at the blade tip was computed using Eq. 4.1 and is shown in Fig. 4.18c as a function of the number of revolution. First, the local twist at the blade tip was settled at approximately 9°, then increased to 11.5° at maximum immediately after the step change, and stabilized at nearly 11°.

In summary, the time-resolved DIC technique developed in this dissertation successfully measured the blade deformations in the following rotor configurations and operating conditions: (i) the small-scale, extremely flexible rotor at four different root pitch angles and rotational speeds, (ii) the large-scale, single-bladed, coaxial lower rotor at a blade loading of 0.09 with good agreement to numerical simulations, (iii) the large-scale, two-bladed, isolated single rotor with a constant collective pitch input, a 1/rev periodic pitch input, and a collective step pitch input.

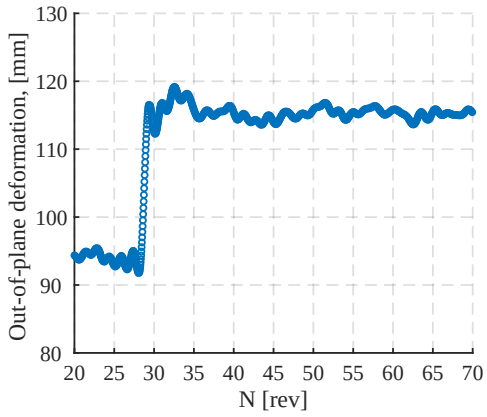

(a) Out-of-plane deformation

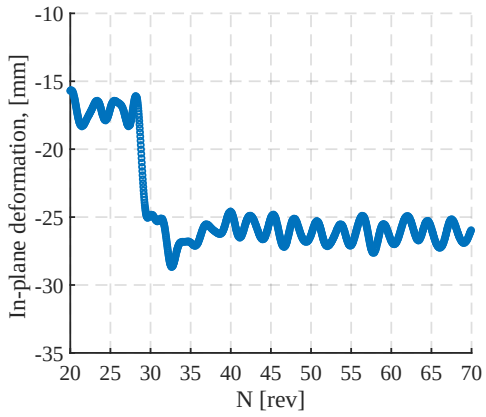

(b) In-plane deformation

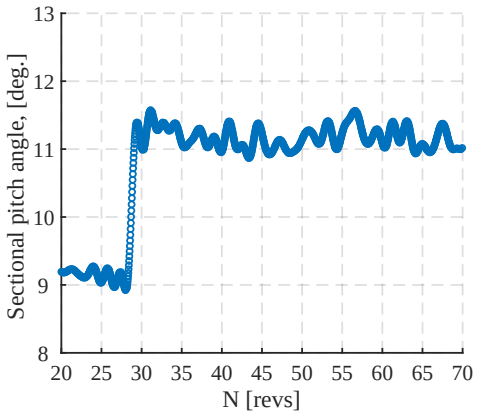

(c) Torsional deformation

Figure 4.18: Blade tip deformations of each degree of freedom as a function of time

4.2 Rotor Blade modal characteristics identification

Based on the rotor blade deformations measured by the DIC technique as described in the previous section, modal properties of the small- and large-scale rotor blade in the rotating frame were identified using several OMA algorithms. Figure 4.19a and 4.19b show the fluorescence-painted small- and

large-scale rotor blade, respectively. Results of the modal parameters identification on the 0.46 m-diameter rotor blade are first presented in § 4.2.1, and results of the OMA analysis on the large-scale rotor blade are discussed in § 4.2.2.

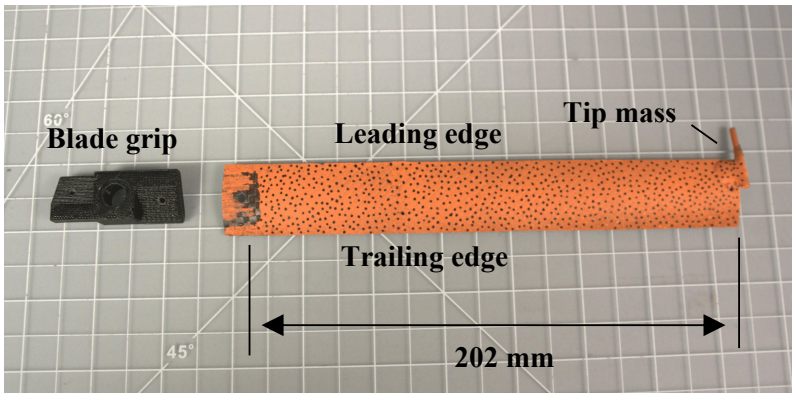

(a) Recap: Small-scale rotor blade

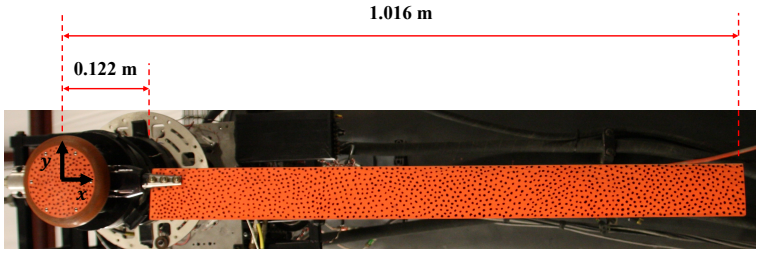

(b) Recap: Large-scale rotor blade

Figure 4.19: Rotor blades with fluorescent paint and random speckle pattern

4.2.1 Small-scale rotor blade characteristics

Modal identification deals with three parameter: natural frequencies, mode shapes, and damping ratios. The OMA algorithms used for the small-

scale rotor blade characteristics were the combined NExT-ERA approach and CP algorithm. Each parameter of the small-scale rotor blade at different operating conditions extracted by OMA processing will be separately addressed in this section.

Additionally, an aeroelastic analysis of the flexible rotor blade was performed using a finite element based numerical model; details of this analysis can be found in Ref. [76]. This computational prediction tool numerically solves non-linear aeroelastic equations of motion including coupled axial elongation, lead-lag (in the rotor plane) bending, flap (normal to the rotor plane) bending and torsional degree of freedom. The aerodynamic part of the analysis includes unsteady terms based on two-dimensional strip theory. The modal frequencies and mode shapes identified by OMA are compared to predictions from this numerical model.

The primary objectives of this process were: (1) to examine how many modes can be identified using the OMA algorithms based on deformation data measured by the time-resolved DIC technique, (2) to compare the results identified by the OMA algorithms, with numerical simulations, and (3) to evaluate the NExT-ERA and CP algorithm regarding accuracy, usability, and robustness of each identification process.

4.2.1.1 Modal frequency

First, identification of the rotating frame natural frequencies is discussed. Before proceeding to the operational modal analysis, the time history

and frequency spectrum of the local pitch angle displacement measured at the blade tip for $\theta_0 = 30°$ case, rotating at 1200 RPM, were first plotted in Fig. 4.20a and 4.20b. The time history of the pitch angle variation at the tip shows periodic motion, corresponding to the oscillation at 1/rev frequency. It can be seen that in this operating condition the spectrum peaks are clear enough to identify which peaks are associated with operating frequencies or modal frequencies. The first peak right next to the 1/rev and second peak between 2/rev and 3/rev harmonics correspond to the first and second modal frequencies as shown in Figure 4.20b. Even if the excitation to the system is random, there are always 1/rev harmonics on any rotating system.

Figure 4.21 shows the frequency spectrum of the blade tip out-of-plane displacement in frequency domain (non-dimensionalized by the rotor frequency), in log scale. This is basically another way of looking at the data taken at 30° root pitch angle spun at 1200 RPM. It appears that the tip displacement variation was a combination of random and periodic motion as also observed in both Fig. 4.20b and 4.21. There were obvious peaks observed in the frequency spectrum, corresponding to the harmonics of rotational speed (i.e., 1200 RPM) as well as the rotating natural frequencies of the rotor blade. Note that the presence of harmonic components might be an issue if the eigen-frequencies of the test specimen are quite close (on the order of 0.1 Hz) to the harmonic excitation, which is not the case in this study. If the frequency of input harmonic excitation is close enough to a natural frequency of the structure to cause failure of the OMA-based modal identification, one would need

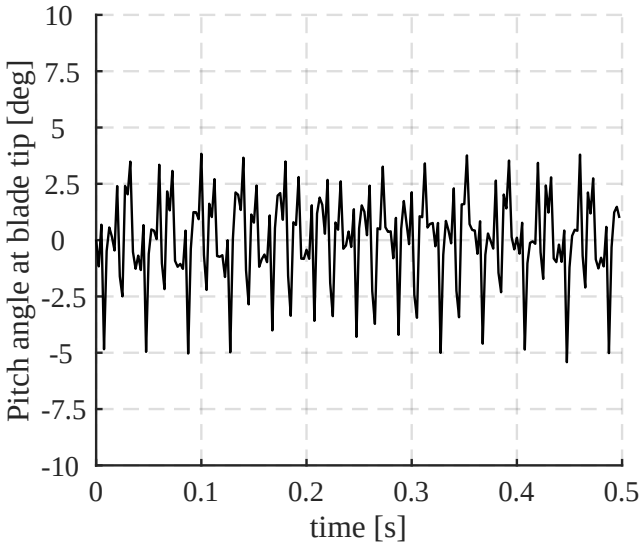

(a) Time domain

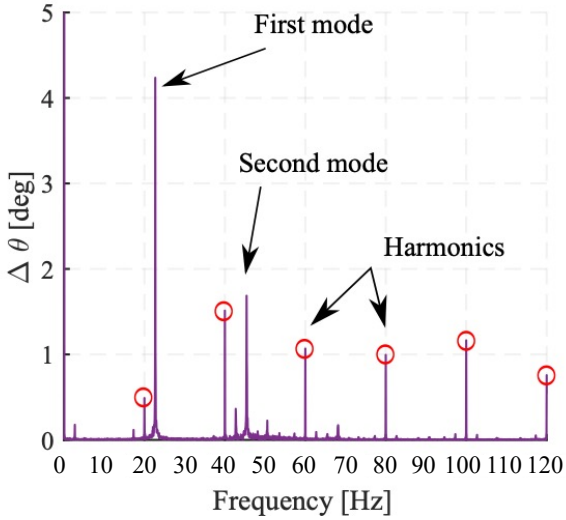

(b) Frequency domain

Figure 4.20: Pitch angle displacement at the tip for $\theta_0 = 30°$, $\Omega = 1200$ RPM

special treatments to account for the harmonic components; see Mohanty and Rixen [77].

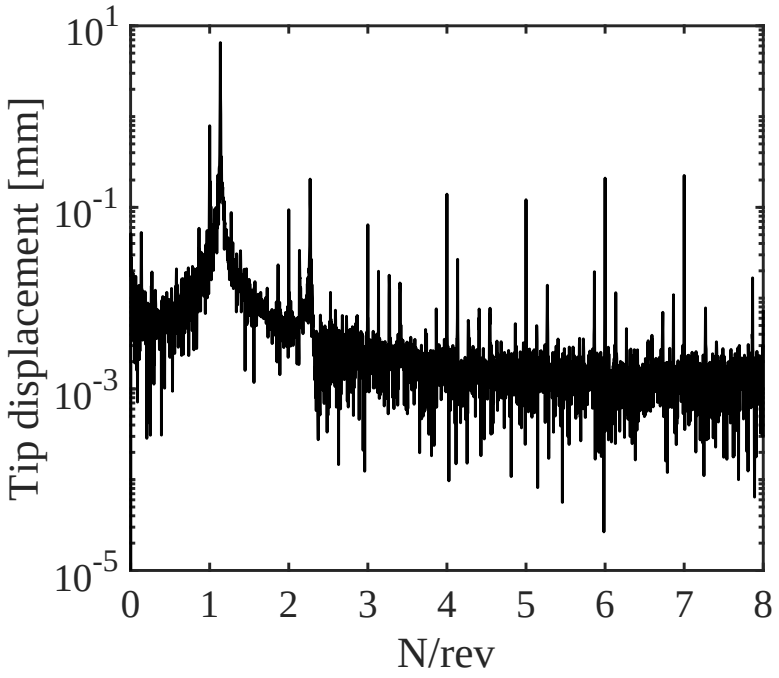

Figure 4.21: Log-scale frequency spectrum of the out-of-plane displacement measured at the blade tip for $\theta_0 = 30°$, $\Omega = 1200$ RPM

Figure 4.22 and 4.23 show the modal frequencies identified by the OMA algorithms as a function of rotor speed; these plots are known as fan plots. In addition, the fan plot for $\theta_0 = 30°$ shows the comparison between these experimental results and predictions from the aeroelastic numerical analysis. Note that these fan plots are presented based on measured data in air, i.e., aerodynamic damping is included. Predictions for $\theta_0 = 0°$ were not available because the numerical model could not converge for this root pitch angle. One

possible explanation for the divergence is instability of rotor blade motion with zero-root pitch angle; during measurements, unstable behaviors of the rotor blade were observed for all the rotational speeds. However, instability analysis is beyond the scope of the current study.

There was good agreement between the CP and NExT-ERA up to the second mode for $\theta_0 = 0°$ and $\theta_0 = 30°$ over a range of different rotational speeds; the extracted modal frequencies for $\theta_0 = 30°$ also agreed well with numerical predictions. These results indicate that this measurement methodology, that is, the DIC deformation measurement in conjunction with OMA algorithm, is quite a useful tool for identifying the modal frequencies of a rotating rotor blade without any input excitation.

4.2.1.2 Mode shapes

Mode shapes of the entire rotor blade, extracted by the CP algorithm, at $\theta_0 = 30°$ spinning at 1200 RPM are plotted in Fig. 4.24 and 4.25. Figure 4.24 corresponds to the first mode and Fig. 4.25 shows the second mode, respectively. The first mode shape was mainly dominated by the flap bending while the second mode was influenced by the torsional deformation. This bending coupling is because the sectional center of gravity and the elastic center are not coincident over the entire span of the rotor blade.

Figure 4.26 and 4.27 shows the components of each degree of freedom along the blade quarter-chord line for the first and second mode shapes, for $\theta_0 = 0°$ and $\theta_0 = 30°$ root pitch angles at 1200 RPM, respectively. The

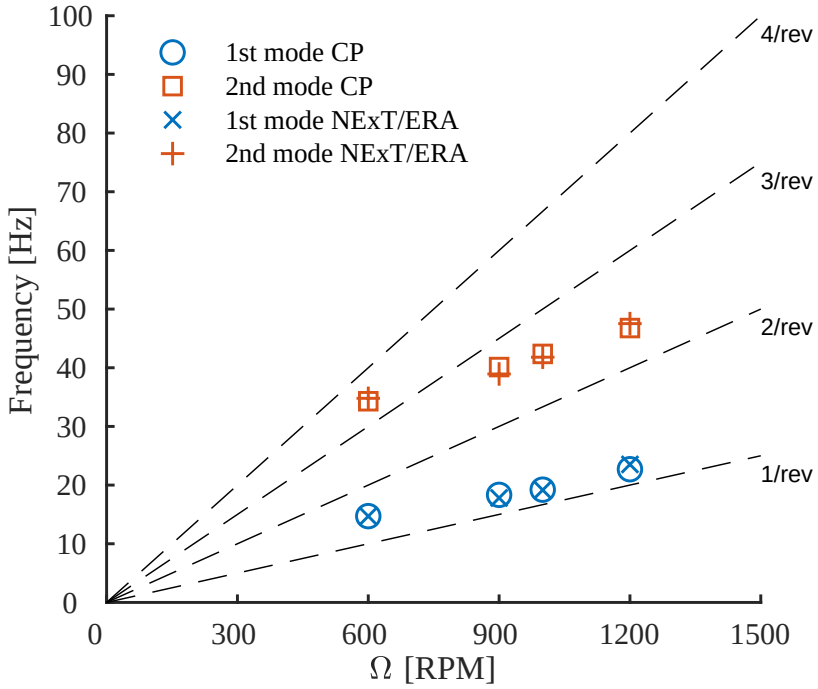

Figure 4.22: Fan plot for $\theta_0 = 0°$, comparing natural frequencies extracted with the CP and NExT-ERA algorithms

amplitudes of the mode shapes are normalized by the maximum value among the flap, lead-lag, and torsional degrees of freedom, to identify the contribution of each degree of freedom to each mode.

It can be seen that at $\theta_0 = 0°$, the lead-lag bending degree of freedom contributed to the first mode shape much less than the flap and torsion degrees of freedom. The contribution of lead-lag bending for the second mode at this same root pitch angle case was also small compared to the other two degrees of freedom, which suggests that the first and second modes of the rotor blade

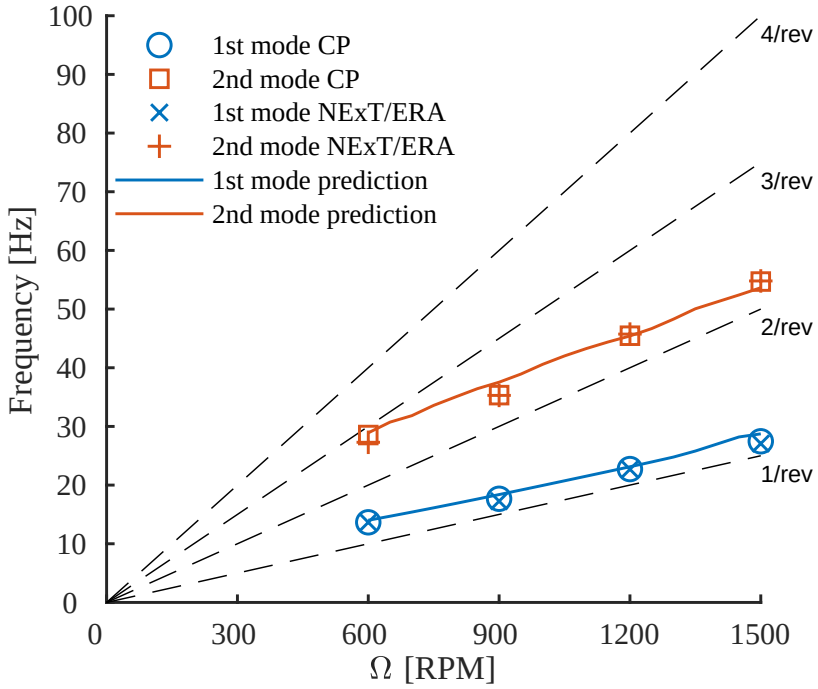

Figure 4.23: Fan plot for $\theta_0 = 30°$, comparing natural frequencies extracted with the CP and NExT-ERA algorithms, along with numerical predictions

mainly consisted of coupled flap and torsional deformations. Now comparing the amplitude of the flap mode to that of the torsional mode, the largest contribution for the first mode was the flap bending while that for the second mode was the torsional deformation. The trend of the mode shapes for $\theta_0 = 0°$ and $\theta_0 = 30°$ was almost the same, except for the amplitude of tip deflection of the second flap mode.

The mode shapes extracted using the two different OMA algorithms are compared to the numerically-predicted results for $\theta_0 = 30°$, operated at

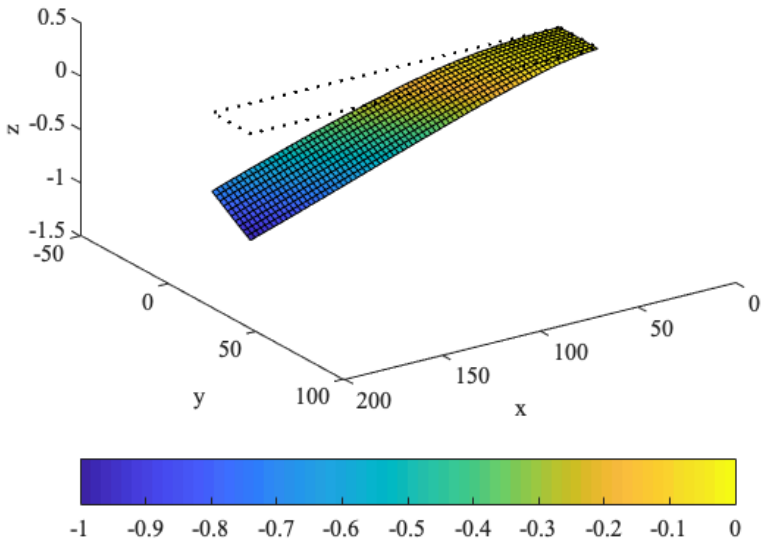

Figure 4.24: The first mode shape of the rotor blade for $\theta_0 = 30^\circ$ at 1200 RPM

1200RPM. Figures 4.28 and 4.29 show the first and second mode shapes of all three degrees of freedom, identified by CP, NExT-ERA, and the computational prediction tool, respectively. For the first mode shown in Fig. 4.28, the lead-lag and torsional mode shapes identified by the CP algorithm appear to be in excellent agreement with those predicted by the numerical model; however, there is a minor discrepancy between the flap mode shape obtained by CP and the computational tool. On the other hand, the mode shapes obtained by the NExT-ERA algorithm are quite different from those predicted by the numerical model for all the degrees of freedom. For the second mode shown in

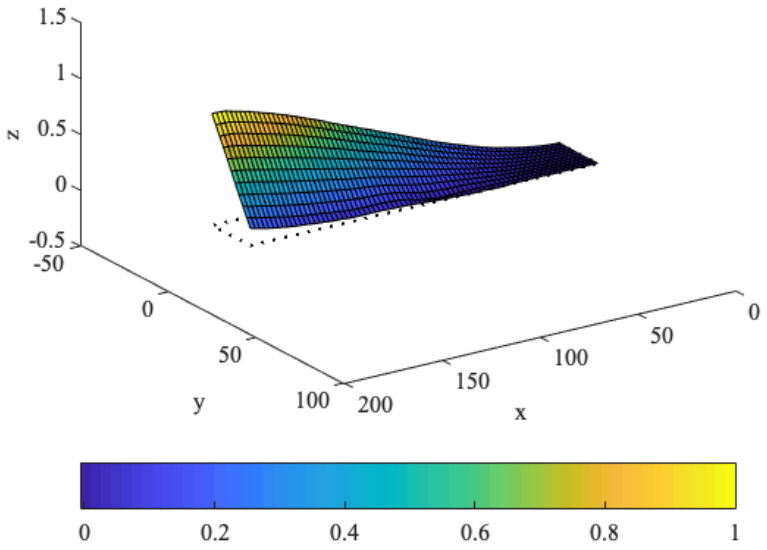

Figure 4.25: The second mode shape of the rotor blade for $\theta_0 = 30°$ at 1200 RPM

Fig. 4.29, the CP-based mode shapes of all three degrees of freedom agree quite well with the numerical results, as was observed for the first mode comparison. However, the mode shapes obtained by the NExT-ERA process are not well correlated with the numerical prediction, except for the lead-lag degree of freedom.

To quantify the differences between the shapes identified by the OMA algorithms and the numerical model, the Modal Assurance Criterion (MAC) was used in this study; details can be found in Ref. [78]. The MAC is one of

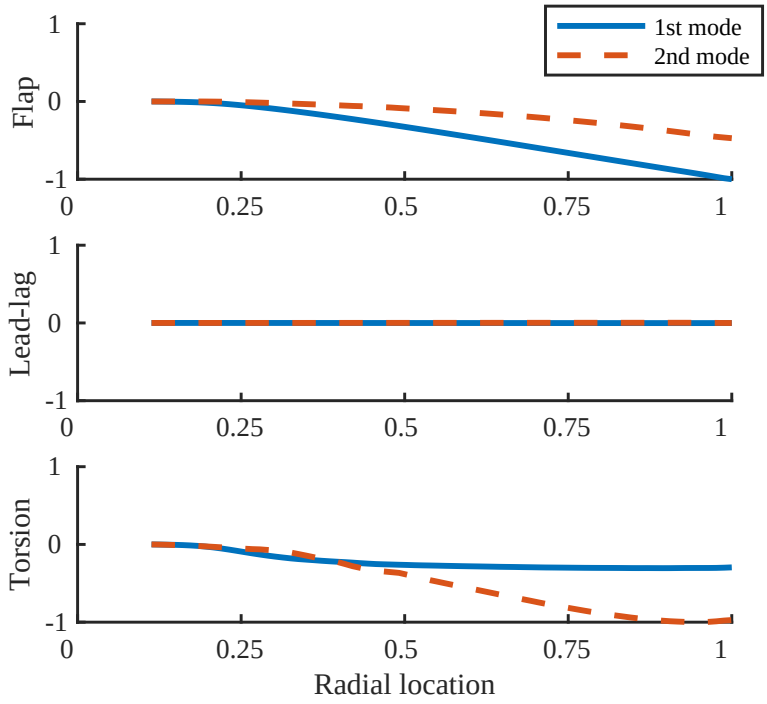

Figure 4.26: The first and second mode shapes along the quarter-chord axis, for $\theta_0 = 0°$

the most common tools for the quantitative comparison of two modal vectors and is defined in terms of the normalized scalar product of the two vectors $\{\varphi_1\}$ and $\{\varphi_2\}$ as:

$$MAC = \frac{|\{\varphi_1\}^T\{\varphi_2\}|^2}{(\{\varphi_1\}^T\{\varphi_1\})(\{\varphi_2\}^T\{\varphi_2\})}. \tag{4.2}$$

The MAC is calculated for two types of comparisons: (1) between the NExT-ERA and the numerical model, and (2) between the CP and the numerical model. Table 4.2 summarizes the MAC values calculated from the mode

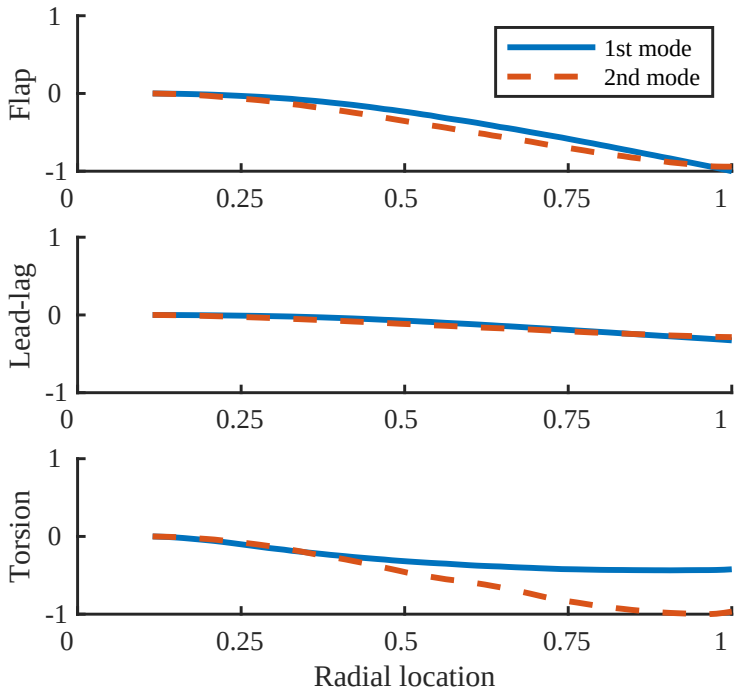

Figure 4.27: The first and second mode shapes along the quarter-chord axis, for $\theta_0 = 30°$

shapes identified by the OMA algorithms and the mode shapes predicted by the numerical model. These mode shapes were obtained from the operating condition where the blade root pitch angle was 30°. Based on the MAC values, the mode shapes extracted by the CP algorithm correlated quite well with the predicted mode shapes (MAC values larger than 0.9 indicate consistent correspondence between two modal vectors). However, the low MAC values between mode shapes extracted by NExT-ERA and predicted mode shapes indicate poor resemblance of these two mode shapes, except for the

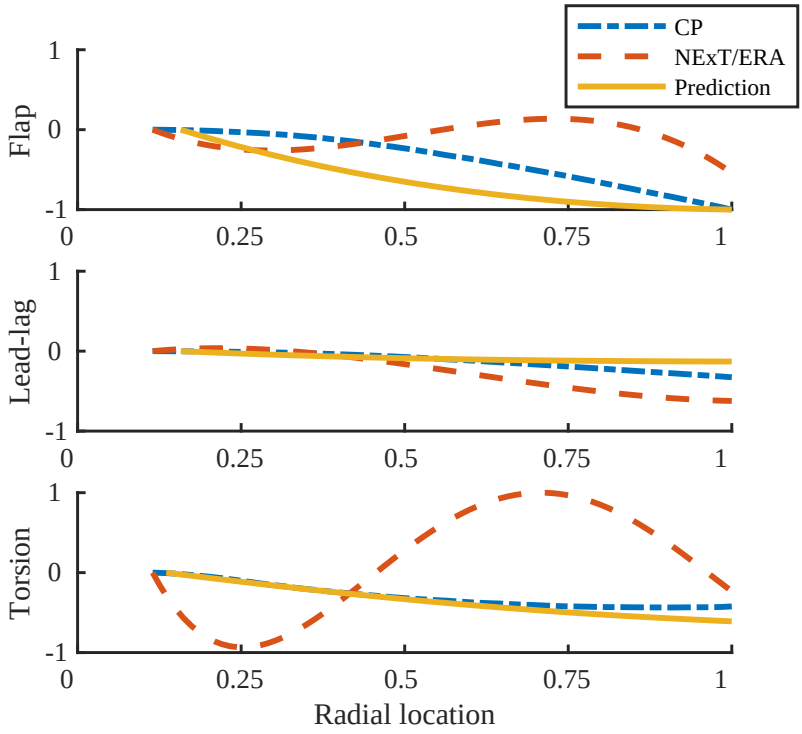

Figure 4.28: Comparison of the first mode shapes estimated by the CP and NExT-ERA as well as numerical prediction for $\theta_0 = 30°$ at 1200 RPM

1st and 2nd lag modes. Note that this study uses Partial Modal Assurance Criterion (PMAC) where only a selected degree-of-freedom from a complete modal vector is used to compute the consistency of identified modes. In this way, linearity of a mode shape of each degree-of-freedom can be evaluated.

The discrepancies between the mode shapes identified by NExT-ERA and the numerical model are mainly associated with the difference in the number of inflection points. For example, for the first torsional mode shape, there are two inflection points on the NExT-ERA result, whereas there is no inflec-

Table 4.2: Summary of the MAC values calculated from the measured and predicted mode shapes, obtained at $\theta_0 = 30°$

	1st mode			2nd mode		
	Flap	Lag	Torsion	Flap	Lag	Torsion
CP	0.874	0.855	0.991	0.932	0.942	0.956
NExT-ERA	0.117	0.835	0.226	0.041	0.586	0.022

tion point on the CP and numerically-predicted results. One possible reason of the poor mode shape estimation by NExT-ERA is that the fictitious and real mode obtained by NExT-ERA analysis were so close to each other in fre-

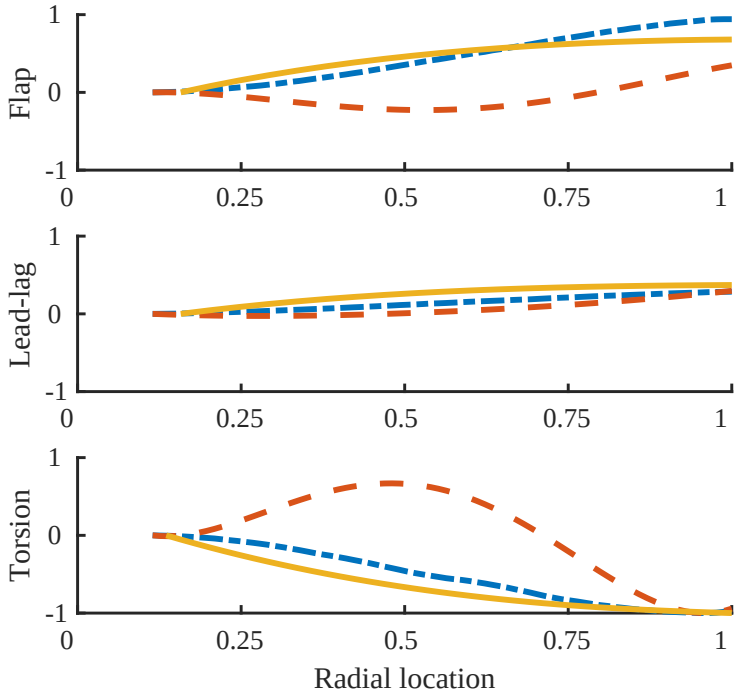

Figure 4.29: Comparison of the second mode shapes estimated by the CP and NExT-ERA as well as numerical prediction for $\theta_0 = 30°$ at 1200 RPM

quency domain that the real mode could not be properly extracted. Another possible reason is that the mode shape extraction by means of NExT-ERA requires a number of parameters and post-processing steps that must be chosen by an analyst, such as applying polynomial fits or removing outliers; these post-processing manipulations could result in poor mode shape identification. A block diagram in Fig. 2.5 shown in § 2.2 summarizes the advantages and disadvantages of these two OMA algorithms. In contrast, the mode shapes identified by CP algorithm without any post-processing showed good correlations with the numerical prediction results.

4.2.1.3 Modal damping

Modal damping has been reported to be the most difficult value among the modal parameters to be estimated with OMA approaches [79, 80]. The present study calculated the damping ratios using a curve fit based on a single-degree-of-freedom impulse response to the auto-correlation function of the separated source signal. Table 4.3 summarizes the estimated modal damping of the rotor blade at a root pitch angle of $\theta_0 = 0°$ for different rotational speeds. For all the cases, the values of modal damping were too small if considering the influence of aerodynamic damping on the rotor blade motion. Table 4.3 also shows the estimated damping values by NExT-ERA [81]. All the damping values from the NExT-ERA analysis were also less than 3% as is the case of the CP analysis.

One of the typical sources of poor damping extraction is the presence

of harmonic excitations on a target structure, as discussed by Mohanty and Rixen [77]. If the harmonic frequency is very close to the modal natural frequency, the OMA algorithm may select this harmonic component of the structural response as one of the eigenvalues. In the current study, however, each mode was selected after excluding the sources with frequencies that were integer multiples of once-per-revolution frequency, as well as the corresponding mode shape. Thus, the identified mode should not be associated with the harmonic excitations, and the cause for the low modal damping is still unclear. These results imply that the modal damping identification process must be further refined to improve accuracy.

Table 4.3: Summary of modal damping ratios for different rotational speeds at 0° root pitch angle

Ω [RPM]	600	900	1000	1200
Modal damping, CP [%]	2.88	0.37	0.11	0.16
Modal damping, NExT-ERA [%]	1.01	0.83	0.75	0.54

In summary, there are three key conclusions from this modal identification processing based on the small-scale rotor blade deformation measurement: (1) The first two modes were identified including the natural frequencies, mode shapes, and modal damping ratios. (2) Modal parameters identified by CP algorithm showed good agreement with the results provided from the numerical model. (3) Identification process with CP algorithm was more efficient and user-friendly, as compared to that with the combined NExT-ERA algorithm. Only the first two modes were identified; this could be because

higher-frequency deformations tend to be small and might approach the noise floor of the DIC technique itself. Increasing the signal-to-noise ratio of the DIC measurements is essential to enable identification of higher modes. The conclusions (2) and (3) are somewhat related, that is, the complicated manual steps with NExT-ERA algorithm resulted in poor quality of modal parameter identification.

4.2.2 Large-scale rotor blade characteristics

Modal parameter identification based on the small-scale rotor blade responses measured by the DIC technique was completed in the previous section. Now, it must be verified if this combined DIC-OMA approach is applicable to the large-scale rotor blade characteristics identification before the ultimate goal of this current study is pursued, i.e., rotor loads estimation based on blade deformation and modal properties. Considering the lessons learned from the small-scale rotor blade characteristics identification, CP algorithm was used to identify the modal parameters for the large-scale rotor blade. As was the case of rotor blade deformation discussed in § 4.1.2, experimental results are compared to numerical predictions provided from Ref. [57].

To extract the modal parameters, two different types of excitation to the rotor blade were tested: (i) random excitation at zero thrust and (ii) collective step input excitation. The former was applied to the single-bladed, single rotor during Test campaign 2, whereas the latter was applied to the two-bladed, single rotor during Test campaign 3. This section describes and

compares the results of each test case with the numerical model.

4.2.2.1 Random excitation (Test campaign 2)

Random vibration tests were performed on the single-bladed, isolated single rotor rotating at 900 RPM. Measured random responses were processed with CP algorithm to extract modal parameters of the rotor blade. The random forcing was obtained by setting a slightly negative rotor collective pitch to achieve almost zero mean thrust with random fluctuations. This would meet the assumption for the OMA algorithm, that is, the deformation input to the algorithm should be the response to random excitation.

Before discussing the OMA results, frequency content of the measured rotor thrust and blade tip displacement are examined. Figures 4.30a and 4.30b show the rotor thrust variation in time and frequency domain, respectively. It appeared that the thrust variation was random in the time domain. However, there were obvious peaks observed in the frequency spectrum. These peaks corresponded to the harmonics of N-per-revolution frequencies, which is inherent to any rotating system and is exacerbated by the presence of a counter-weight (see Fig. 4.6), i.e., dissimilar rotor blades. Importantly, the magnitude of the thrust increased with frequency and was fairly constant at high frequencies, which lends confidence to the assumption of random excitation.

The tip displacement in time and frequency domain, shown in Figs. 4.31a and 4.31b, also exhibited a trend similar to that for the rotor thrust response. The harmonic components of the rotating frequency were the significant con-

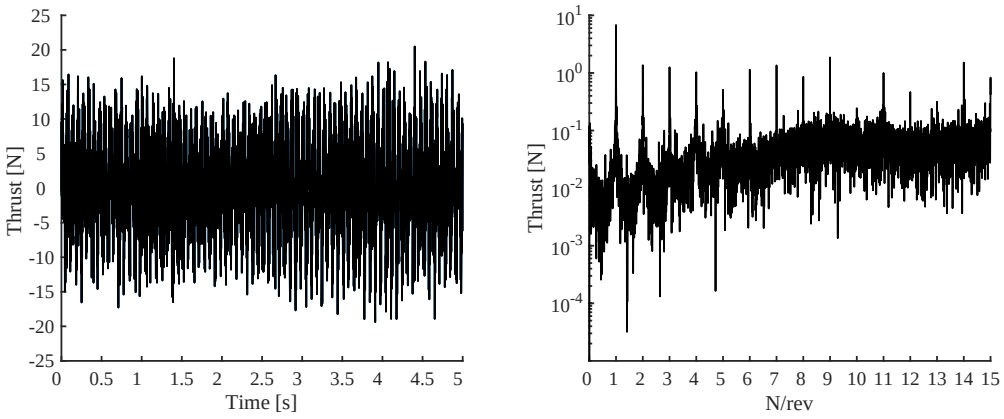

(a) Time domain (b) Frequency domain

Figure 4.30: Thrust measured on the single-bladed single rotor at zero mean thrust

tributors to the response, as observed in the results of the hover testing on the extremely flexible rotor system; (see § 4.2.1). However, since the modal frequencies were not close to the harmonic excitations (on the order of 0.1 Hz), no special treatment was required.

Now, the CP algorithm was used to extract the rotating natural frequencies and mode shapes of the rotor blade. The fan plot in Fig. 4.32 shows the natural frequencies identified by the CP algorithm (at the nominal rotational frequency of 900 RPM) along with numerical predictions. Note that the natural frequencies at 300 RPM, 600 RPM, and 1200 RPM were obtained in previous experiments by Cameron et al. [35], who used a different modal identification algorithm on the same experimental setup. It can be seen that the extracted natural frequencies agree well with the numerical predictions as well as with previous measurements over different rotational frequencies.

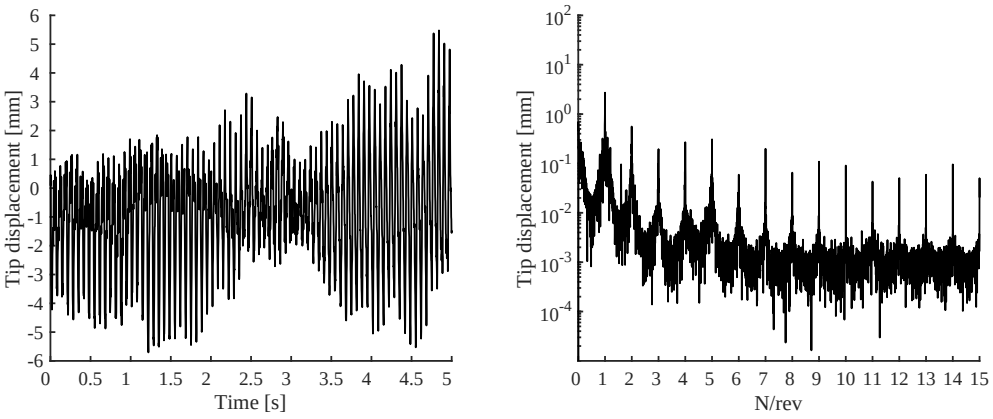

(a) Time domain (b) Frequency domain

Figure 4.31: Measured variation of tip displacement on the single-bladed single rotor at zero mean thrust

Figure 4.33 to 4.35 shows the first flap, the first lag, and the second flap rotating mode shapes compared to predicted results, respectively. There was good agreement between the numerically predicted characteristics and the results obtained by the CP algorithm for all three mode shapes. The MAC was also used for the results of the large-scale rotor blade modal parameter identification, to quantify the differences between the measured and predicted mode shapes; see Eq. 4.2. Table 4.4 summarizes the MAC values of the mode shapes as well as the rotating frame natural frequencies for both identified and predicted parameters. This excellent agreement between the CP-derived and numerically-obtained modal parameters indicates that the DIC deformation measurement in conjunction with the CP algorithm can also be used to identify the rotating frame natural frequencies and modes shapes of the large-scale rotor blade.

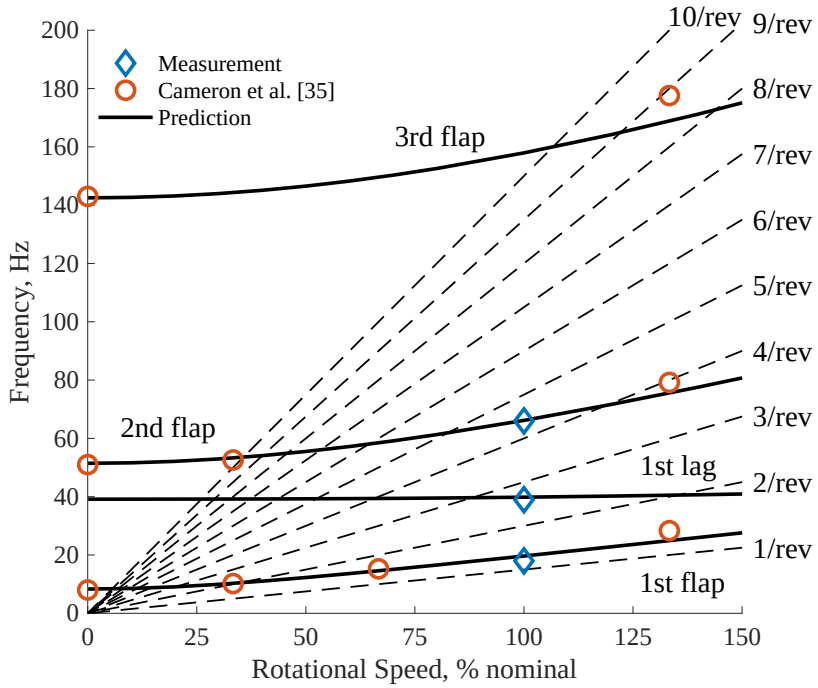

Figure 4.32: Fan plot with measured natural frequencies (100% = 900 RPM), compared with numerical predictions

Table 4.4: Summary of the rotating natural frequencies and MAC values calculated from the measured and predicted mode shapes.

	1st Flap		1st Lag		2nd Flap	
	Freq., Hz	MAC	Freq., Hz	MAC	Freq., Hz	MAC
Measurement	17.9	0.999	39.0	0.998	66.0	0.992
Prediction	19.6		39.8		66.2	

4.2.2.2 Step function excitation test (Test campaign 3)

Although the combined DIC-OMA approach was able to extract modal parameters from the random response obtained during the Test campaign 2 as described above, the identified modes were limited to only the first flap,

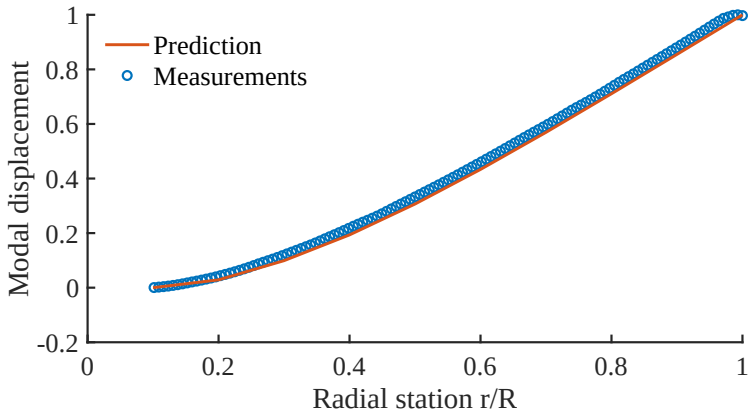

Figure 4.33: Measured rotating mode shapes of the first flap mode at nominal rotational speed (900 RPM) compared with numerical predictions

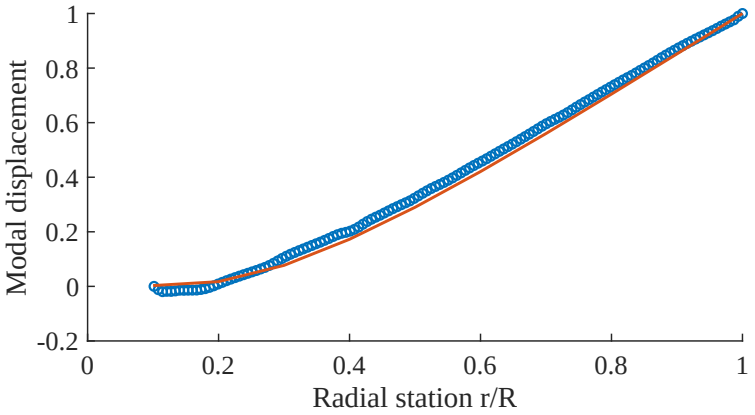

Figure 4.34: Measured rotating mode shapes of the first lag mode at nominal rotational speed (900 RPM) compared with numerical predictions

the first lag, and the second flap bending mode. This was the motivation of performing modal parameter identification based on another data set, which was the blade response to the step function excitation.

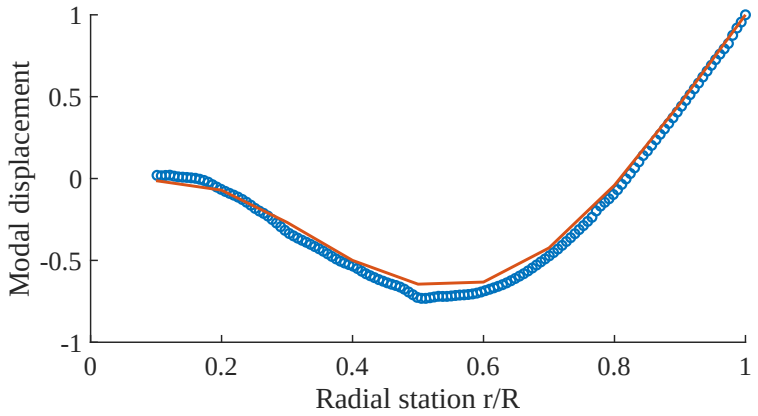

Figure 4.35: Measured rotating mode shapes of the second flap mode at nominal rotational speed (900 RPM) compared with numerical predictions

First, frequency spectrum analysis was conducted to examine the frequency components of the blade structural responses to the 2° collective step pitch input. As a set of data samples for this analysis, the time history of the out-of-plane deformation measured at the trailing-edge point of the rotor blade tip was extracted and is shown in Fig. 4.36. The data set was then divided into three periods: (i) before the step pitch input was applied, (ii) during the transient response, and (iii) after the response settled down to the steady-state condition.

Figure 4.37 shows the frequency spectrum of the three different time periods up to 120 Hz (8/rev). The overall trend commonly observed in the spectra was the dominant periodic peaks corresponding to the integer multiples of rotational frequency. There were some smaller peaks between those multiples of rotational frequency, however, it was challenging to distinguish

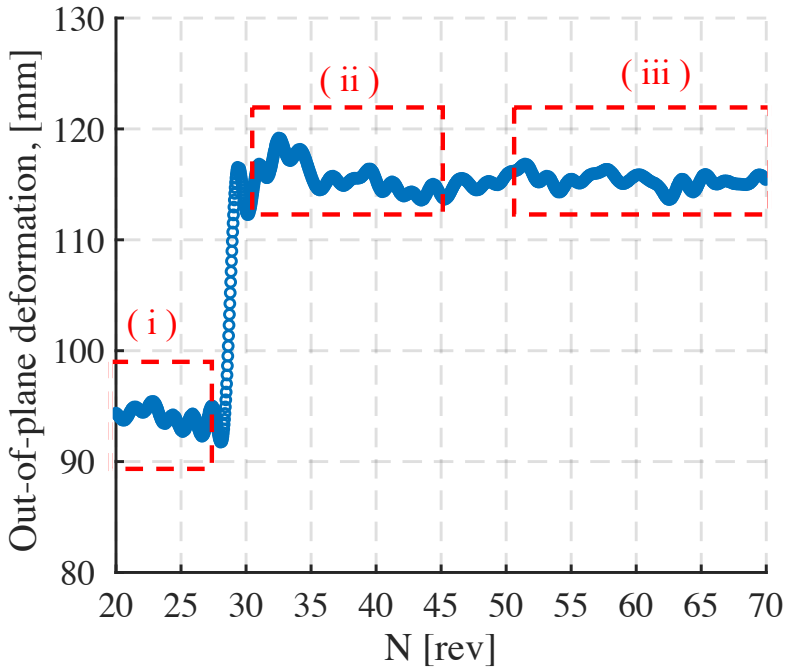

Figure 4.36: Time history of the out-of-plane deformation measured at the trailing-edge point of the rotor blade tip

which peaks were associated with fictitious noise or the actual rotating frame natural frequencies. Since the time period (iii) had the largest number of samples, the frequency spectrum (iii) in Fig. 4.37 has a higher resolution in the frequency domain than in the spectra in cases (i) and (ii).

Noise level of each time period seems to be different in Fig. 4.37, however, that is due to the number of sample sizes used for the Fourier Transform. Since the time period (iii) had a largest amount of samples, the frequency spectrum (iii) appears to contain more noise than the other two sets of data.

To address this challenge, another analysis approach in frequency do-

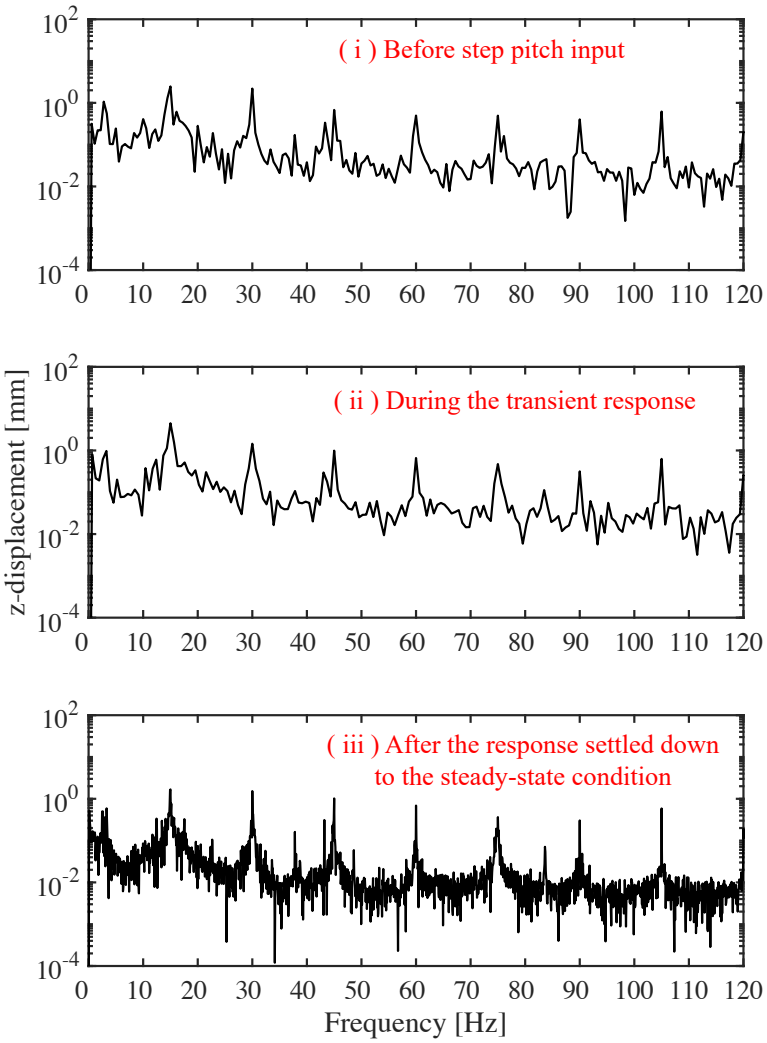

Figure 4.37: Frequency spectra of the three different time periods

main, called spectrogram, was used and applied to the same data set. A spectrogram is defined as a visual representation of frequency spectrum of a time-dependent signal and can estimate the time-localized frequency contents

using the short-time Fourier transform. The signal is typically divided into several segments for windowing, so that one can see how frequency components in the signal change in time. Figure 4.38 shows the spectrogram of the same signal analyzed in Fig. 4.37. The parameters used for the spectrum are summarized in Table 4.5. Note that the sampling rate of the DIC measurement was 15 Hz (rotational speed) $\times$ 32 azimuthal resolution = 480 Hz. At regions where the step change occurred (around 2.5 s) in the spectrogram, wide-bandwidth vibration was propagated in the power contour and it immediately died out after the step change. This frequency content can be interpreted as a proof of the successful excitation to the blade structure. On the other hand, the periodic harmonic components attributed to the integer multiples of the rotational frequency (15 Hz) remained constant over the entire measurement period.

Table 4.5: Parameters used for the spectrogram analysis

sample size	8000
sample rate	480 Hz
length of each segment	500
segment overlap	490
windowing function	Hamming
data points for FFT	500

With these spectrum analyses completed, the complexity pursuit algorithm was applied to the blade response. Table 4.6 summarizes the modal parameters identified based on the responses to two different excitations, along with the numerical model. The OMA algorithm only extracted the first two

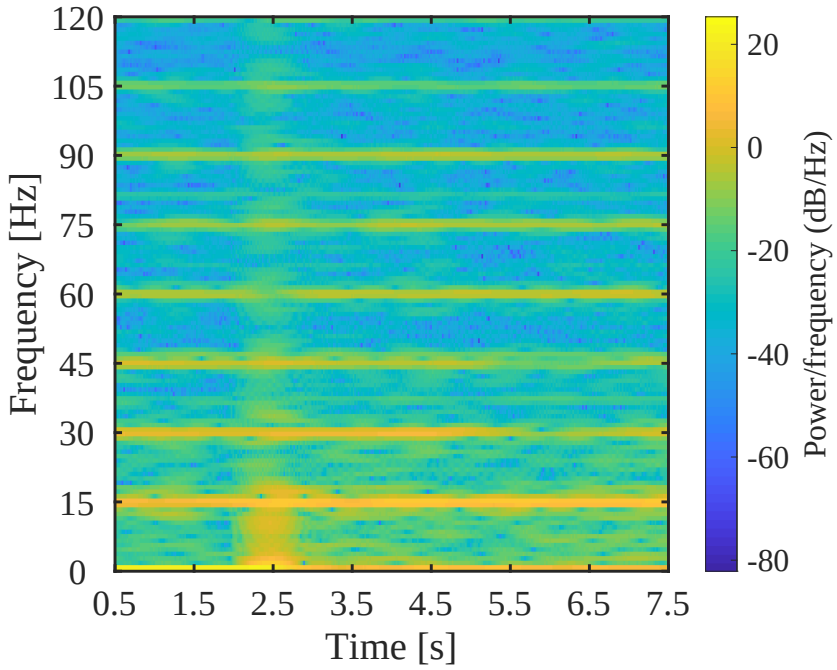

Figure 4.38: Spectrogram of the flap response measured at the trailing edge point of the blade tip

flap modes, which was less than the number of modes identified during the Test campaign 2. Additionally, the MAC for the second flap mode identified during Test campaign 3 was low, indicating that the second mode shape was not well correlated with either the numerical prediction or the mode shape extracted during Test campaign 2. The original intention of this test condition was to excite the rotor blade structure by the rapid collective pitch change (step function as an excitation source), so that the resultant response might contain a large number of structural modes at higher amplitudes as compared to the response to the random, turbulence-driven, ambient aerodynamic load-

ing achieved during Test campaign 2.

Table 4.6: Summary of the experimentally and numerically obtained modal frequencies and MAC values calculated from the measured and predicted mode shapes for Test campaign 2 and 3

	1st Flap		1st Lag		2nd Flap	
	Freq., Hz	MAC	Freq., Hz	MAC	Freq., Hz	MAC
Test campaign 2	17.9	0.999	39.0	0.998	66.0	0.992
Test campaign 3	17.8	0.992	-	-	66.3	0.641
Prediction	19.6	N/A	39.8	N/A	66.2	N/A

There could be several reasons why the OMA processing of the data measured in this test condition failed to extract the higher structural modes: First, the sampling rate was not large enough to capture the step-induced oscillation whose decay rates were so large as shown in the spectrogram (see in Fig. 4.38). In other words, the decay of the transient response to the collective step change was to rapid to capture with the current sampling rate (480 Hz). Second, the magnitude of the step change (corresponding to 2° increase) was not strong enough to excite the higher modes of the blade structure during rotation. These results of the modal parameter identification must be investigated further in future work.

4.3 Rotor loads measurement and estimation

Results of rotor loads measurements and estimation are presented in this section. The current study focused on the large-scale rotor loads measurement and estimation based on the blade deformations and modal parameters discussed in § 4.1 and § 4.2. This section is divided into two subsections:

In § 4.3.1, measured thrust and pitch link force of the CCR lower rotor are compared with the numerical model provided from Ref. [57], and measured rotor loads are compared with results of loads estimation process for the three different operating conditions (a constant collective input, a periodic 1/rev, and a collective step input) in § 4.3.2.

4.3.1 CCR rotor loads measurement

The blade deformation and rotor loads were simultaneously measured during the Test campaign 2 on the single-bladed CCR rotor system at a high blade loading coefficient that was still below stall limits ($C_T/\sigma = 0.09$). The frequency spectrum of the vibratory thrust on the lower rotor of the CCR rotor system is shown in Fig. 4.39a up to 9/rev. It can be seen that the 1/rev component of ±20 N was the largest contributor to the coaxial lower rotor thrust. Although 2/rev harmonics are the dominant characteristic of vibratory loads associated with blade passage as shown in Fig. 4.10, a contribution from odd harmonics can also be seen.

Figure 4.39b shows the measured lower rotor thrust as a function of rotor azimuthal angle compared to numerical predictions. The shaded area corresponds to measurement uncertainty. Overall, it can be seen that the thrust increased as the upper and lower rotor blades approached each other, and it decreased after the blade passage. This can be explained by the mechanism of bound circulation interaction that is shown schematically in Fig. 4.10. That is, upwash induced by the upper rotor blade on the lower rotor blade

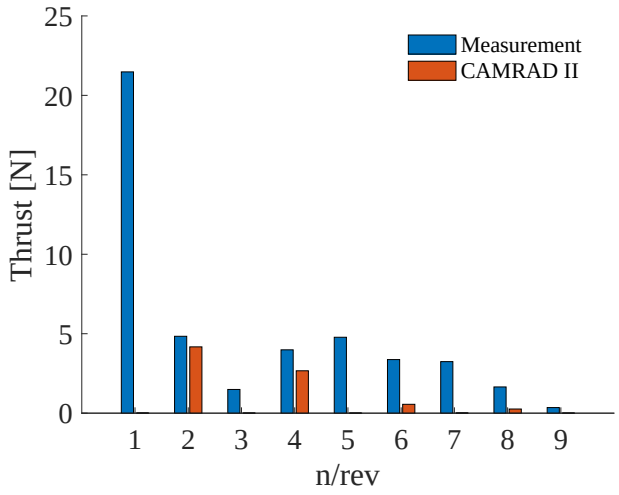

(a) Frequency domain

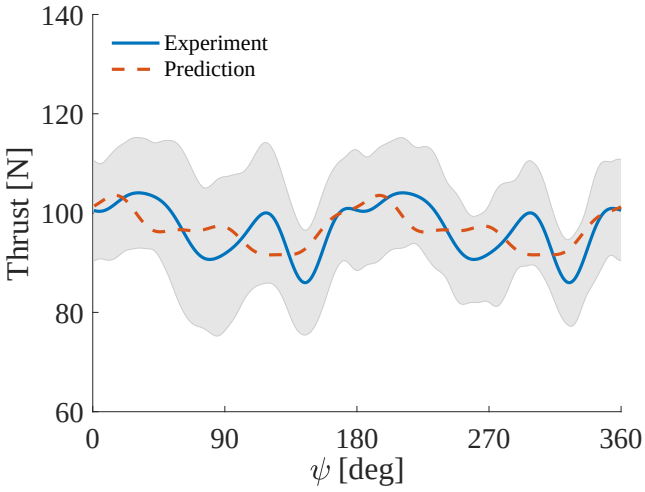

(b) Azimuthal domain

Figure 4.39: Reconstructed (filtered) thrust of the CCR lower rotor, compared to predictions at $C_T/\sigma = 0.09$

increased the effective angle of attack of the lower rotor blade, resulting in the increase in rotor thrust, and vice versa. While the magnitude of the predic-

tions correlated well with the measurements, there was some discrepancy in the phase. For the first blade passage, peaks occurred at about $\psi = 15°$ and $\psi = 30°$ for prediction and measurement, respectively, whereas for the second blade passage, peaks occurred at about $\psi = 195°$ and $\psi = 210°$ for prediction and measurement, respectively. Recall that the blades crossed each other at $\psi = 0°$ and $\psi = 180°$.

Figure 4.40a shows the amplitudes of each harmonic component of measured pitch link loads, revealing a large 1/rev component similar to the thrust variation. Figure 4.40b compares the measured and predicted pitch link loads as a function of blade azimuthal angle. Good correlation of magnitude between measurement and prediction was observed, whereas a phase shift of $\psi = 60°$ between the measured and predicted trends was also observed.

Overall, the vibratory thrust was approximately 10% of the mean thrust, which is consistent with previous studies by Cameron et al. [35, 82] where the vibratory thrust was 11% of the mean thrust in hover. More significantly, the vibratory pitch link load was found to be nearly 30 % of the mean pitch link load, which can have a profound impact on the design of the rotor control system. Thus, for the large-scale rotor hover test rig, it is concluded that the three major components of measured quantities for the rotor loads estimation methodology proposed in the dissertation, i.e., blade deformation, blade modal properties, and rotor loads, were captured well by the numerical prediction.

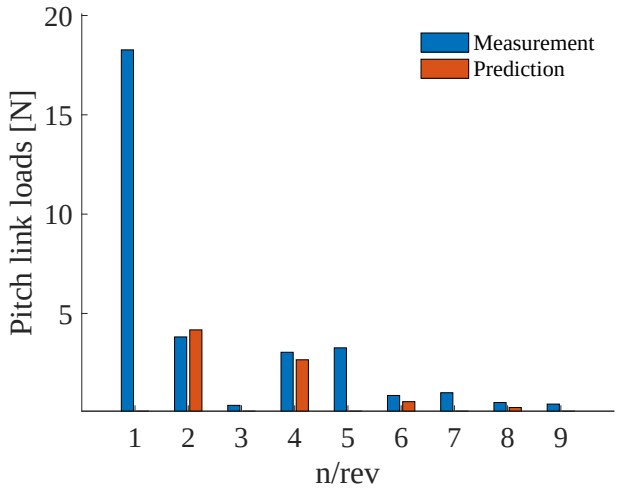

(a) Frequency domain

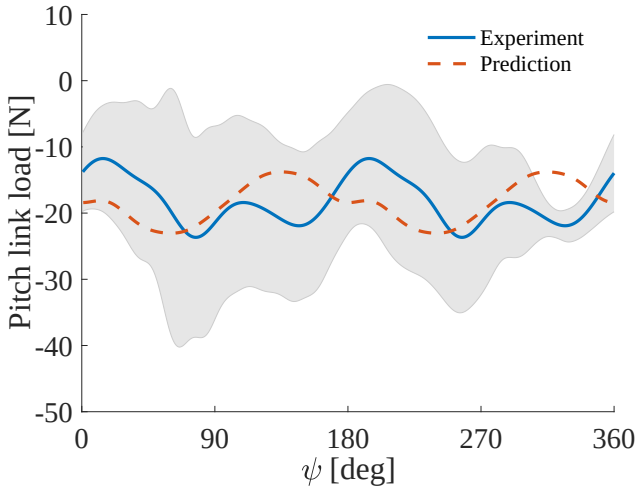

(b) Time domain

Figure 4.40: Reconstructed (filtered) pitch link load of the CCR lower rotor, compared to predictions at $C_T/\sigma = 0.09$

4.3.2 Two-bladed single rotor loads measurement and estimation

With the success of validation process between the experimental results and numerical simulations during Test campaign 2, the final step of the current study is to estimate rotor loads based on the blade deformation measured by the DIC technique and the blade modal parameters identified by OMA processing. Rotor loads include the spanwise lift distribution along the blade and the integrated hub loads. To verify if the proposed approach for rotor loads estimation holds in a variety of loading scenarios, three different operating conditions were tested during Test campaign 3 and summarized in Table 4.7. Note that among the three modes identified through the OMA processing, only the first and second flap modes were used to reconstruct the rotor loads because the lag modes does not contribute to the out-of-plane force.

Table 4.7: Recap: Summary of operating conditions for Test campaign 3

Condition	C_T/σ	Trim	θ_0	θ_{1c}
1	0.125	Constant pitch	9°	-
2	0.125	1/rev pitch	9°	2°
3	-	Step pitch	9° + 2° step	-

4.3.2.1 Test condition 1

The first operating condition tested on the two-bladed single rotor was a constant collective pitch input at a blade loading C_T/σ of 0.125. Measured quantities include: hub loads, pitch link loads, and blade root pitch angles.

The rotor thrust variation, measured by the six-component load cell

and phase-averaged over 250 revolutions, is shown in time (azimuthal) and frequency (non-dimensionalized by the rotational frequency, 15 Hz) domain in Fig. 4.41a and 4.41b, respectively. Note that all the loads variations in this section are measured in the rotating frame. The frequency spectrum clearly represents the general relationship between the mean and vibratory components of hub loads, that is, vibratory loads of a single rotor in hover are much smaller than the steady mean component of rotor loads. In this test case, there was little vibration in hub loads (less than approximately 1% of the mean thrust), since a constant collective pitch input was applied to the rotor.

A similar trend can be seen in the rotor torque; the variation in time and frequency domain are shown in Fig. 4.42a and 4.42b, respectively, with an oscillatory behavior at the 3/rev harmonic visible in both domains. The magnitude ratio of the 3/rev component to the mean torque is approximately 8.5%, which is relatively large compared to a typical vibration level in hover. The 3/rev variation can also be seen in more profound manner in the rotating frame rolling moment, as shown in Fig. 4.43. One possible reason for this large 3/rev vibration is the proximity of the 1st lag mode frequency to the 3/rev blade crossing (see the fan plot shown in Fig. 4.32).

Pitch link loads were measured using the axial tension-compression load cell for both blades. Pitch link force measurements enable investigation of rotor blade pitch moment dynamics, as well as determination of maximum allowable blade loading for safe operation during hover testing. Figure 4.44

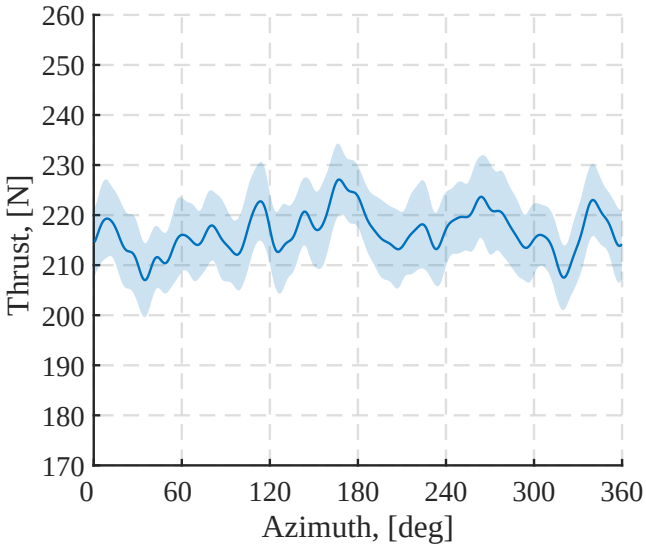

(a) Time domain

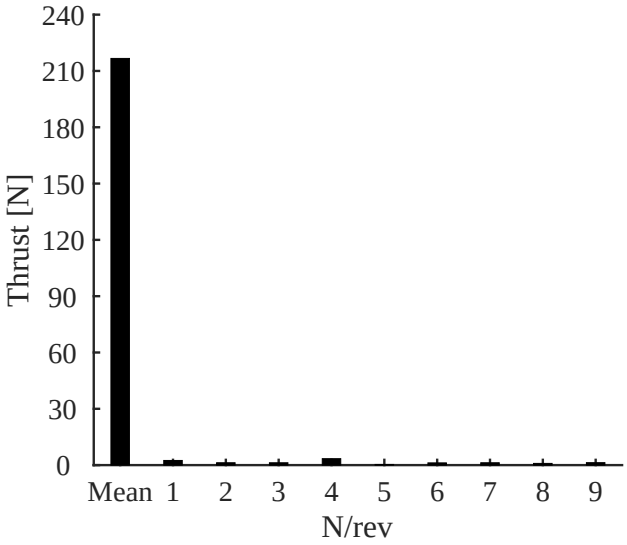

(b) Frequency domain

Figure 4.41: Phase-averaged thrust variation as a function of blade azimuthal location for the steady collective pitch input

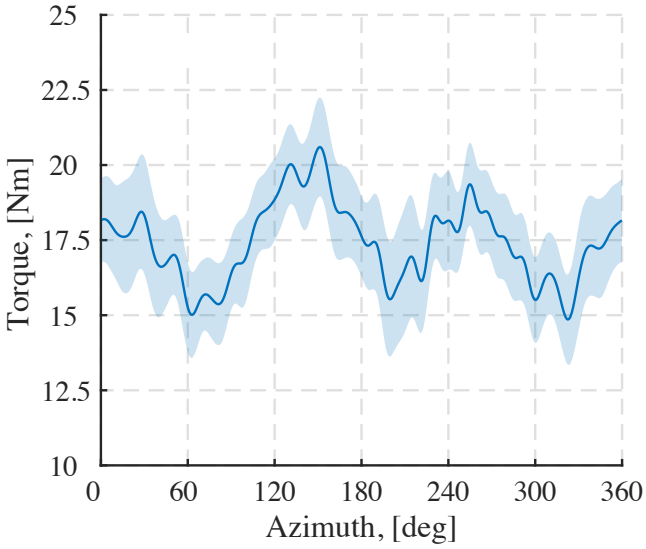

(a) Time domain

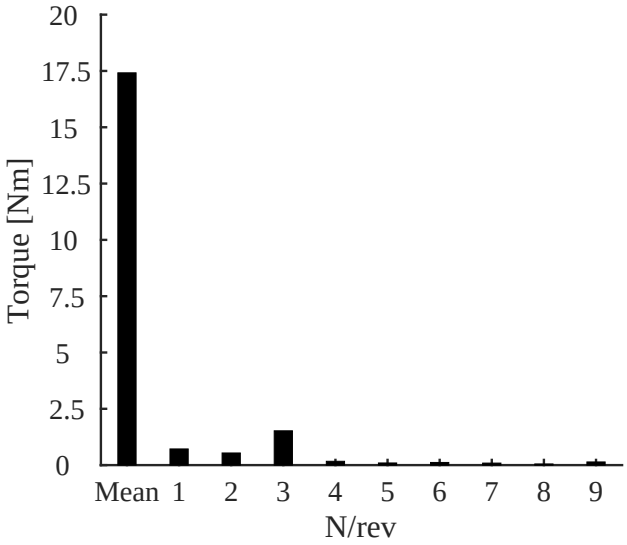

(b) Frequency domain

Figure 4.42: Phase-averaged torque variation as a function of blade azimuthal location for the steady collective pitch input

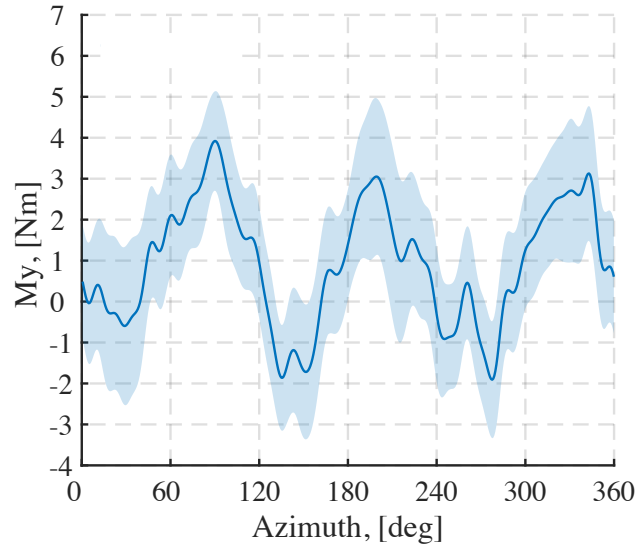

(a) Time domain

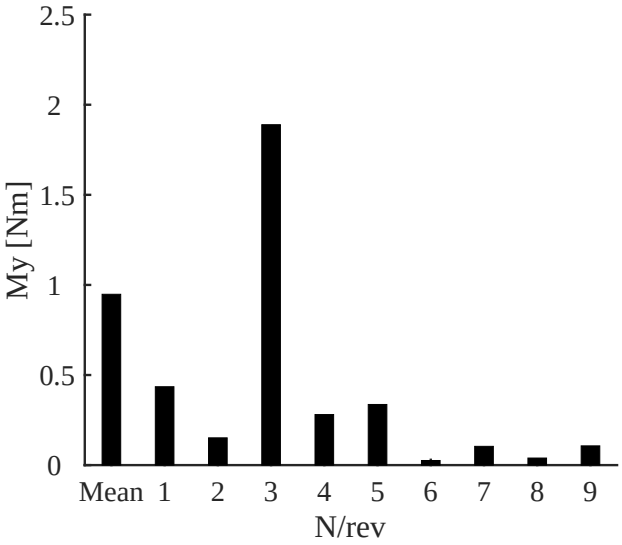

(b) Frequency domain

Figure 4.43: Phase-averaged pitching moment variation as a function of blade azimuthal location for the steady collective pitch input

shows the azimuthal variation and its frequency spectrum of pitch link loads for both blades. In Fig. 4.44a, there was a clear phase difference of nearly 180° between the pitch link (blade) 1 and 2, implying that there might exist a slight inclination of the swashplate that caused the out-of-phase pitch moment variation for the two blades. Most of the vibratory components were contained in the first three harmonics for both blades, with a 1/rev component as the largest contributor to the pitch link force variation as shown in Fig. 4.44b. A possible source of the slight magnitude difference of the 1/rev harmonic component was the presence of viscous damping in the bearing mechanism (grease lubrication) for rotor feathering motion.

Blade root pitch angles for both rotor blades were measured using the Anisotropic Magneto-Resistive (AMR) sensors installed on the blade grips (see § 3.1.2 for more details). The real-time measurement of root pitch angles enables trimming the rotor at a target operating condition during hover testing.

Figure 4.45 shows the phase-averaged root pitch angle of both blades as a function of azimuthal position over one revolution. The overall trend of the blade pitch 1 corresponds to the trim target of this test condition 1 (a steady, mean collective pitch $\theta_0 = 9°$). However, there was a large fluctuation in the blade pitch 2 measurement over the range of 60 to 180 deg, possibly due to the free play of the corresponding pitch link or needle bearings that hold the blade grip. It is interesting to note that the mean component of root blade pitch 1 (about 9.27° from Fig. 4.45a) was nearly the same as the torsional

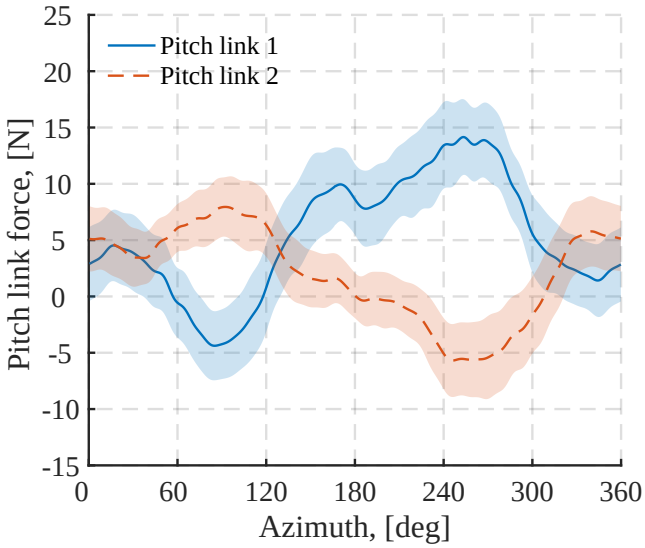

(a) Time domain

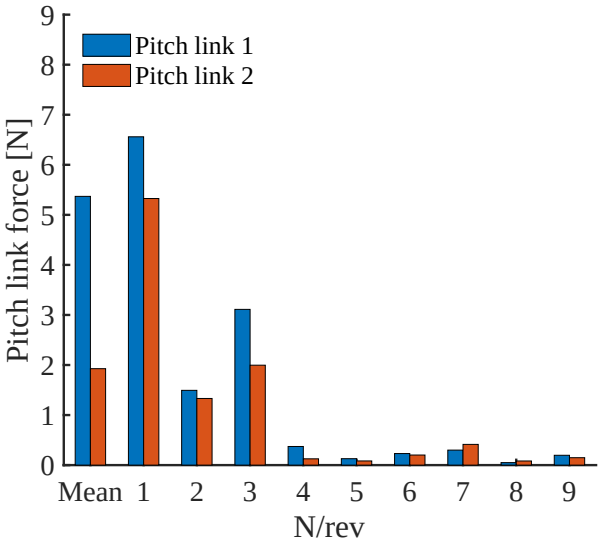

(b) Frequency domain

Figure 4.44: Phase-averaged pitch link force variation as a function of blade azimuthal location for the steady collective pitch input

displacement over the blade span calculated using the DIC results shown in Fig. 4.15c. This result implies that the rotor blade used for this hover testing experienced little elastic twist at this blade loading condition, and the DIC measurement agrees well with the results measured by the AMR pitch angle sensor.

The frequency spectrum of the pitch angle variations is shown in Fig 4.45b, revealing that the observed fluctuation on the pitch angle measurement 2 was associated with the 1/rev frequency component. The normalized amplitude of the vibratory component was less than 2% of the mean collective pitch, thus it is fair to say that the intended rotor trim control was achieved for the test case A.

Now the results of rotor loads estimation for the test condition 1 are discussed. Rotor loads include the spanwise lift distribution along the quarter-chord blade axis, and the hub loads (thrust) obtained by numerical integration of the lift distribution in spanwise direction. For rotor load estimation, the first and second flap modes identified from Test campaign 2 (see § 4.2.2) were used.

Figure 4.46a shows the estimated sectional lift distribution as a function of blade radial and azimuthal location. This plot was obtained by applying the rotor load estimation methodology to the phase-averaged blade flap deformation over one revolution, and only illustrates the variation of the airload of one rotor blade, whose deformation was measured using the DIC technique (Recall that one of two blades on the two-bladed rotor was used as a test spec-

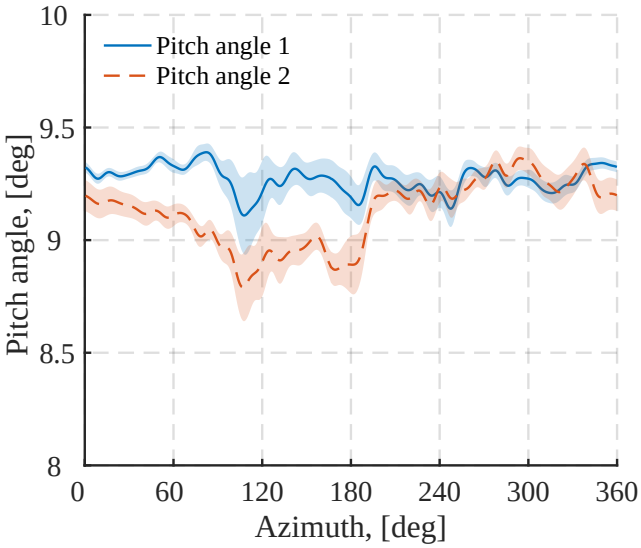

(a) Time domain

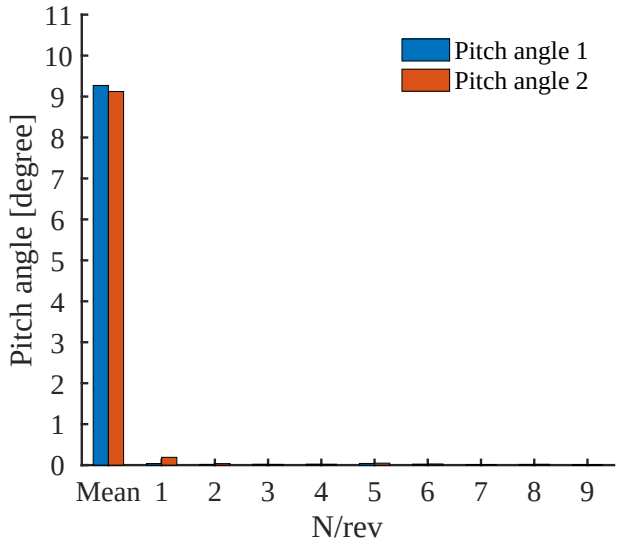

(b) Frequency domain

Figure 4.45: Phase-averaged pitch angle variation as a function of blade azimuthal location for the steady collective pitch input

imen for the DIC deformation measurement). As expected from the numerical experiment, the sectional load monotonically increased up to the blade tip without capturing the decrease (tip loss) due to the influence of tip vortices (see Fig. 2.12). The lack of participating modes (only two modes) was the primary cause for the poor estimation at the blade tip. On the other hand, the integrated hub load, shown in Fig. 4.46b appeared to be well correlated to the directly-measured thrust, especially for the steady, mean component of the thrust variation. Although the vibratory loads seemed to have a slight discrepancy, the mean thrust difference was observed within 5%.

4.3.2.2 Test condition 2

For the test condition 2, the rotor was trimmed at a constant collective plus a lateral cyclic pitch angle. The collective pitch θ_0 was set to be 9° so that the mean blade loading remained the same as for the test condition 1. The periodic 1/rev lateral pitch θ_{1C} was set to be ±2°. Measured quantities are the same as the previous test condition, including hub loads, pitch link loads, and root pitch angle variation.

The phase-averaged thrust variation in the rotating frame as a function of blade azimuthal location and its frequency spectrum are shown in Fig. 4.47a and 4.47b, respectively. The 2/rev vibratory load can be clearly seen in azimuthal domain as compared to the steady thrust for the test condition 1 (steady collective pitch input), and the relative magnitude of the component normalized by the mean thrust was calculated to be nearly 3.2%. Figure 4.48a

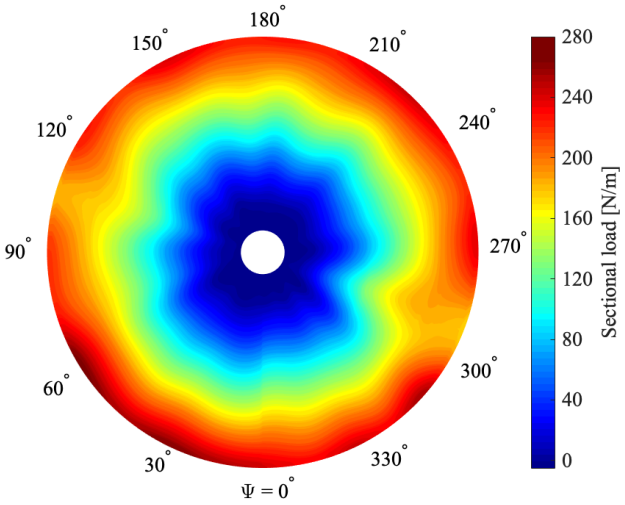

(a) Estimated lift distribution over one revolution

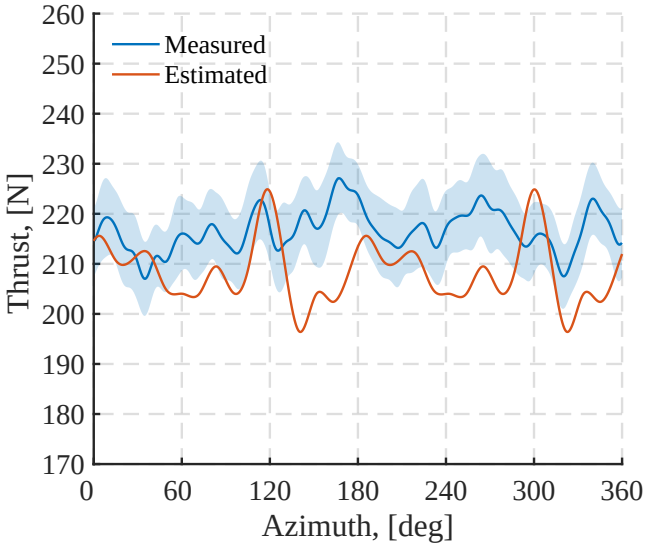

(b) Comparison between the estimated and measured rotor hub loads

Figure 4.46: Estimated rotor loads for the steady collective pitch input

and 4.48b show the torque variation, revealing the large 3/rev vibratory component (relative amplitude of 11%) that was also observed for the test condition 1. The presence of the 3/rev harmonics is consistent with both the test condition 1 and 2, indicating that the source of this vibration might depend on the rotor blade modal parameters, as discussed in the previous test condition.

The primary difference between the test condition 1 and 2 was found in the rotating frame rolling moment M_y as shown in Fig. 4.49. Due to the asymmetric lift distribution over the rotor disk, the rotor experienced the large variation in the rolling moment over one revolution. The clean sinusoidal trend at the 1/rev frequency corresponds to the lateral cyclic pitch input ($\theta_{1C} = 2°$) to the rotor control. As can be seen in Fig 4.16, the tilting motion of the rotor disk was consistently associated with the trend of the rolling moment, meaning that the tilting direction of the rotor disk appropriately reflected the sign change of the rolling moment.

The frequency spectrum shown in Fig. 4.49b helped to identify that the 1/rev vibratory component was the largest contributor to the moment variation, which was consistent with the trend in azimuthal domain shown in Fig. 4.49a. Note that comparing the vibratory loads for this condition 2 to that for the condition 1, the magnitudes of the 3/rev harmonic component were on the similar order of 2 Nm, implying that this 3/rev vibratory load consistently observed in most of the loads data was possibly attributed to a common source in the experimental setup.

The pitch link force variation for both rotor blades is shown in Fig 4.50.

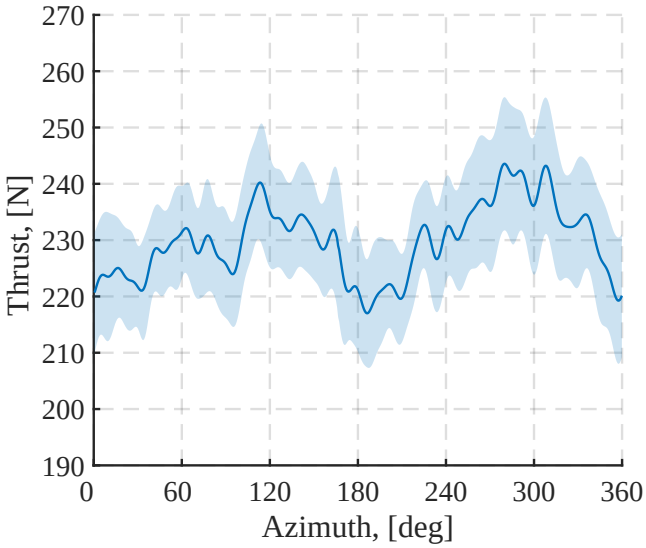

(a) Time domain

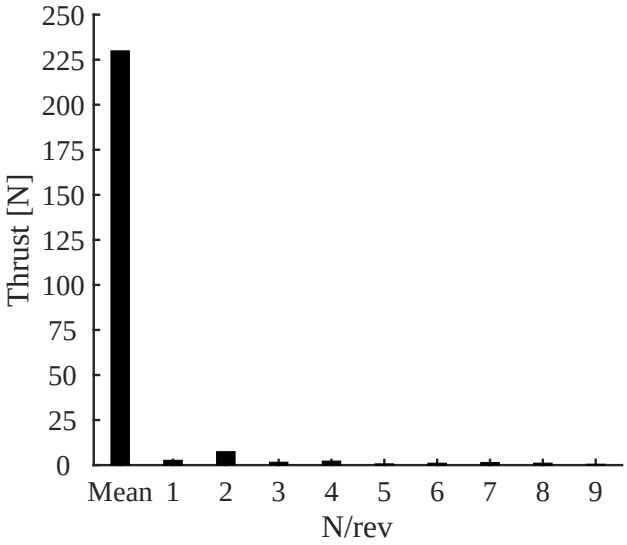

(b) Frequency domain

Figure 4.47: Phase-averaged thrust variation as a function of blade azimuthal location for the lateral cyclic pitch input

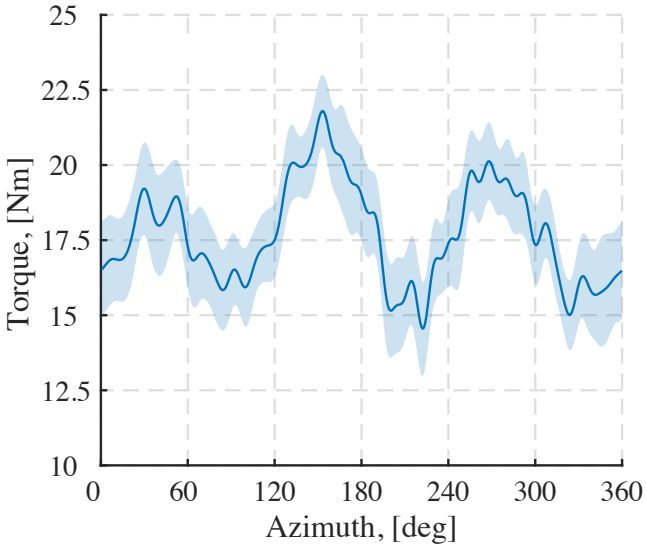

(a) Time domain

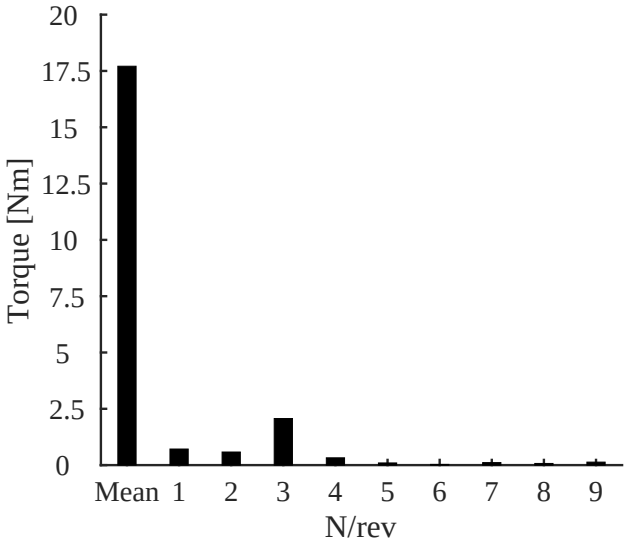

(b) Frequency domain

Figure 4.48: Phase-averaged torque variation as a function of blade azimuthal location for the lateral cyclic pitch input

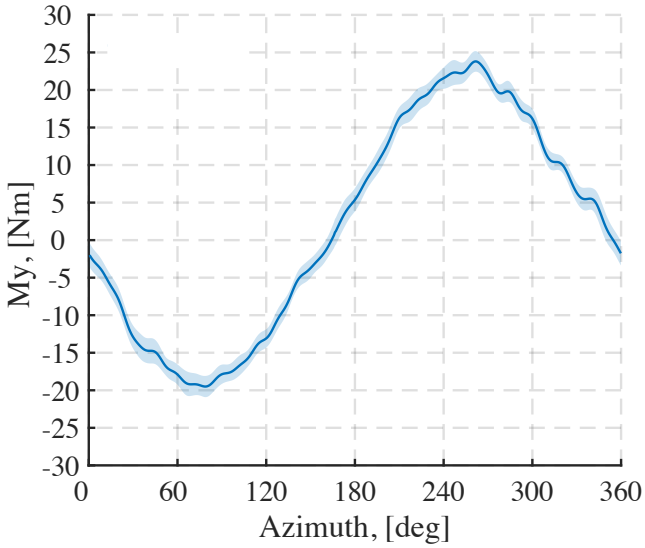

(a) Time domain

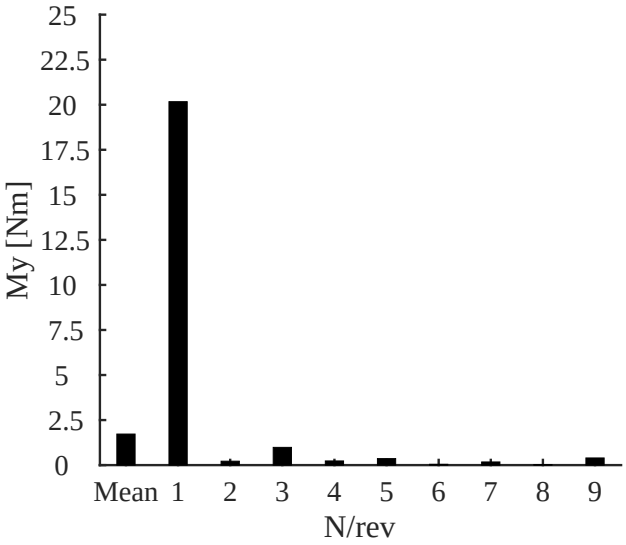

(b) Frequency domain

Figure 4.49: Phase-averaged pitching moment variation as a function of blade azimuthal location for the lateral cyclic pitch input

Figure 4.50a presents a significant 1/rev sinusoidal trend for both pitch links and the clear azimuthal phase offset of approximately 180° between the two rotor blades. The 1/rev vibratory component directly corresponds to the variation of the blade pitching moment due to the swashplate inclination corresponding to the lateral cyclic pitch. On the other hand, Fig. 4.50b compares the vibratory components of the two pitch link loads in frequency domain. The magnitudes of the 1/rev component for the pitch link 1 and 2 were respectively 19.4 N and 15.7 N, which were the dominant component consistently for both linkages; however, the values were shown to have a discrepancy of approximately 5 N. The mean, steady component seems to have a difference on the same order of magnitude as well. The constant offset between two linkages can also be seen in Fig. 4.44 for the test case condition 1, indicating that there must be some common source of this difference, regardless of rotor trim condition, such as free-play in rod ends or grease lubrication in the feathering bearings.

The phase-averaged blade root pitch angle variations are shown in Fig. 4.51a and 4.51b in blade azimuthal and frequency domain, respectively. This demonstrates successful pitch control using the swashplate and servo-actuators; the collective (mean) pitch θ_0 was set to be equal to 9°, and the cyclic pitch θ_{1C} was set to be $\pm 2°$.

The spanwise distribution and integrated hub load for the test condition 2 were estimated and compared to the measured data. For the test condition 2, the rotor was trimmed at the steady collective pitch $\theta_0 = 9° +$ the lateral

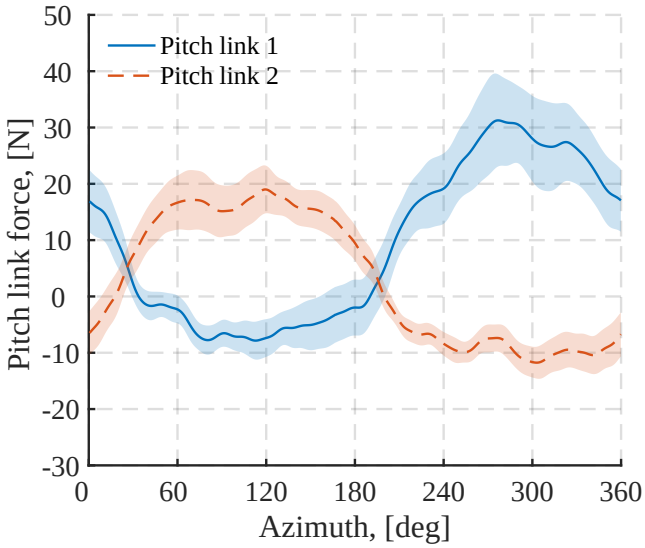

(a) Time domain

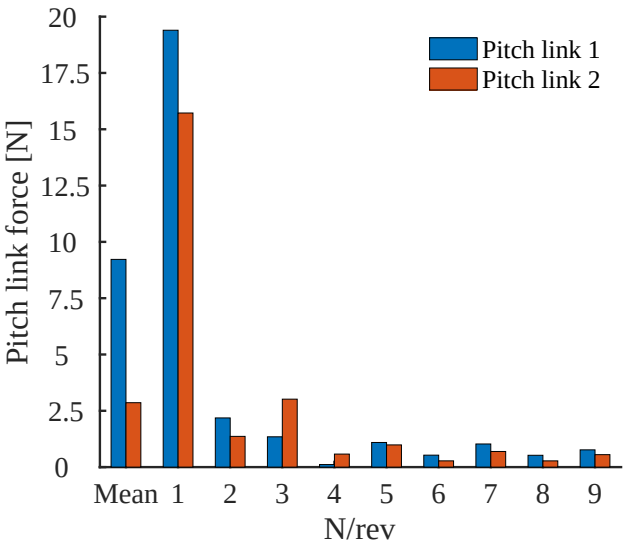

(b) Frequency domain

Figure 4.50: Phase-averaged pitch link force variation as a function of blade azimuthal location for the lateral cyclic pitch input

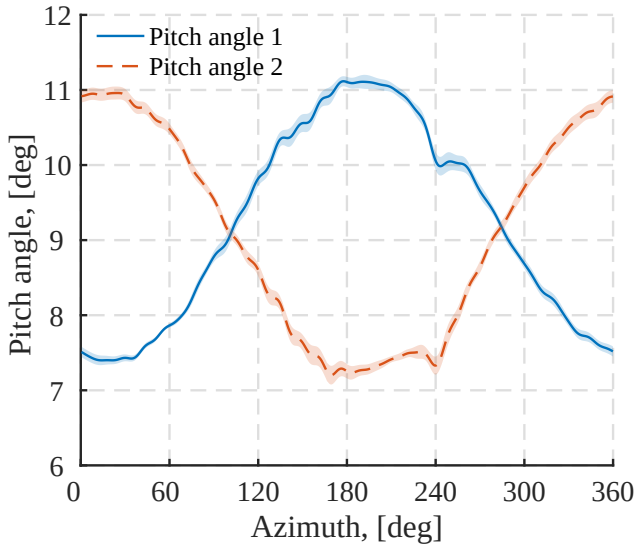

(a) Time domain

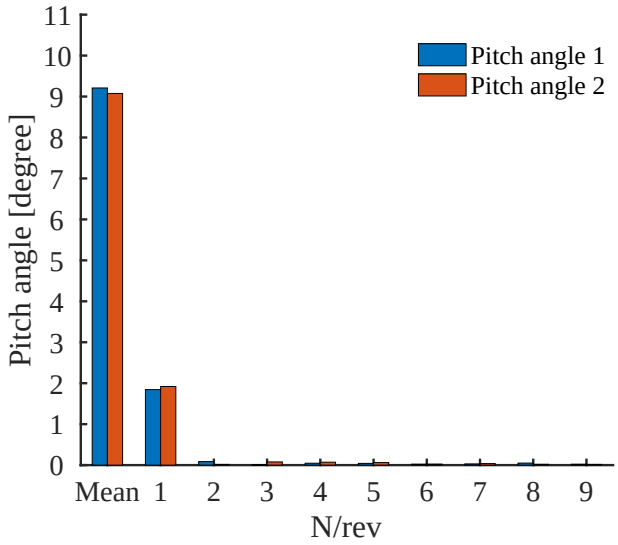

(b) Frequency domain

Figure 4.51: Phase-averaged pitch angle variation as a function of blade azimuthal location for the lateral cyclic pitch input

cosine cyclic input $\theta_{1C} = 2°$. Figure 4.52a shows the sectional lift distribution based on the phase-averaged blade flap bending variation over the entire rotor disk. The contour clearly represents the aerodynamic force variation at once-per-revolution frequency with the consistent phase, however, the lift tip loss was not captured for this case, either. Figure 4.52b compares the integrated hub loads for the lateral cyclic pitch input, revealing the pronounced 2/rev vibratory content in the estimated thrust variation. The 2/rev component of the estimated thrust agreed well with that of the measured thrust in terms of both magnitude and phase. There was a mean thrust discrepancy of nearly 5%, which was also observed in Fig. 4.46 for the test condition 1.

4.3.2.3 Test condition 3

The test condition 3 was a rapid increase of collective pitch angle by 2°, so that the rotor would experience dynamic, transient responses to the step-function excitation. It should be noted that most of the measured data shown in this section were processed with a low-pass filter at a cutoff frequency that was specifically selected for each measured quantity, in order to clearly observe trends of the response to the collective step. These cutoff frequencies were mainly selected by trial-and-error. Table 4.8 summarizes the cutoff frequencies selected for this low-pass filtering process.

First, the measured blade root pitch angle is plotted as a function of rotor revolution in Fig. 4.53. Note that the horizontal axis of plots shown in the following subsections was converted from time to the number of revolutions.

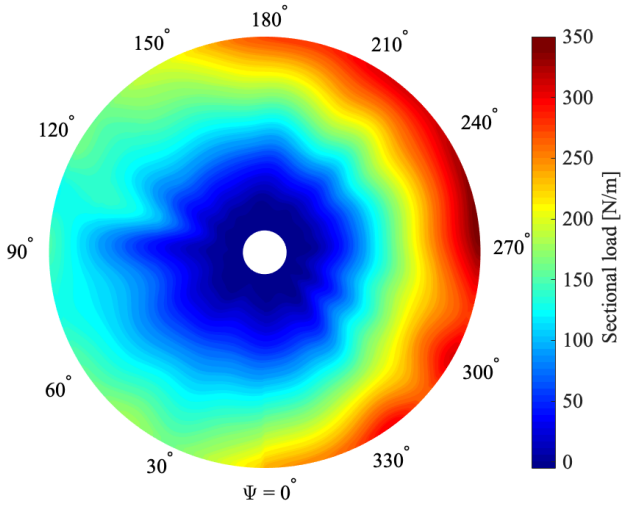

(a) Estimated lift distribution over one revolution

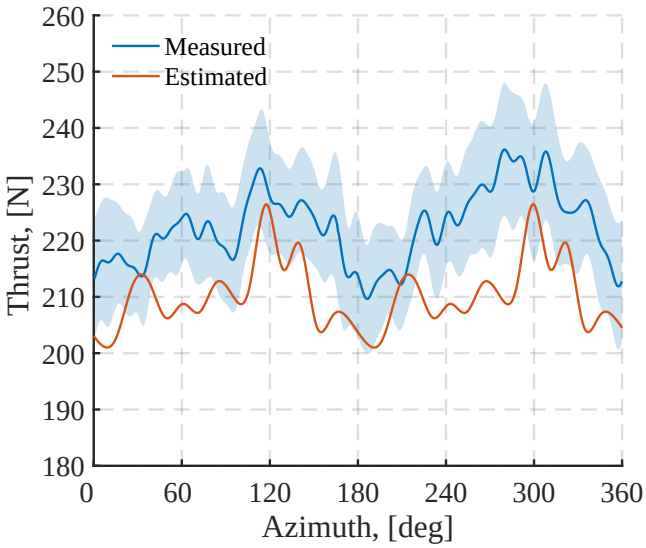

(b) Comparison between the estimated and measured rotor hub loads

Figure 4.52: Estimated rotor loads for the lateral cyclic pitch input (Test condition 2)

Table 4.8: Summary of cutoff frequencies for low-pass filtering process for Test campaign 3

Measured quantity	Cutoff frequency [Hz]
Deformations	13
Blade root pitch	13
Rotor rotational speed	42
Thrust	25
Torque	25
Pitch link load	8

To clearly show the pitch variation, the low-pass filter was applied with a 3 dB corner frequency of 13 Hz. In Fig. 4.53, the blade root pitch angle started increasing from approximately 9.5 degree during the 28th revolution, and reached the steady state value of about 11.5 degree after completing the 35th revolution.

There was an additional measured quantity specifically available for this test condition, which is the rotational speed of the rotor resulting from the rapid increase of rotor torque. Figure 4.54 shows the rotational speed variation of the rotor shaft as a function of time, low-pass filtered at a cutoff frequency of 42 Hz. The maximum speed drop was nearly 25 RPM, and the ringing behavior lasted for approximately 40 revolutions. This low-frequency oscillation possibly contaminates other measured quantities, that is, data might no longer represent the rotor physics operated at constant rotational speed of 900 RPM. However, the magnitude of the oscillation might be small (nearly 2.5%) and it has little influence of the analysis of the current study, because the primary purpose of this test condition was to excite the modes of the rotor blade

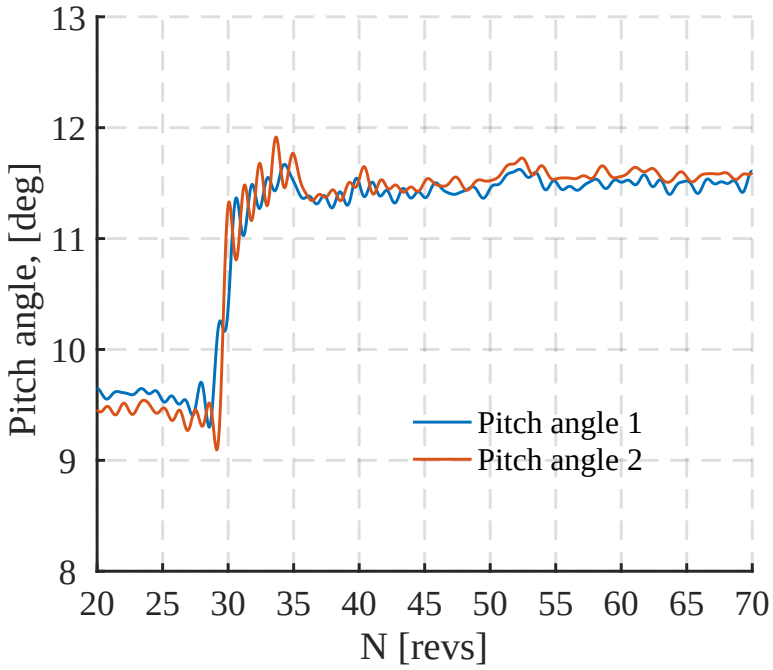

Figure 4.53: Blade root pitch angle as a function of rotor revolutions during the step pitch input operation

structure as much as possible by applying the rapid collective pitch change.

Now the rotor thrust and torque responses to the step pitch increase are examined. The time history of the low-pass filtered thrust and torque are shown in Fig. 4.55 and 4.56, respectively. The increase in thrust started during the 28th revolution and maintained the rate of change up until the 30th revolution, then the slope changed to a lower value. This slope transition was consistent to the variation of other quantities including the pitch angle variation and blade tip deflection. The rotor mean thrust was first at about 230 N at $\theta_0 = 9°$, then increased by approximately 40 N due to the 2° collective

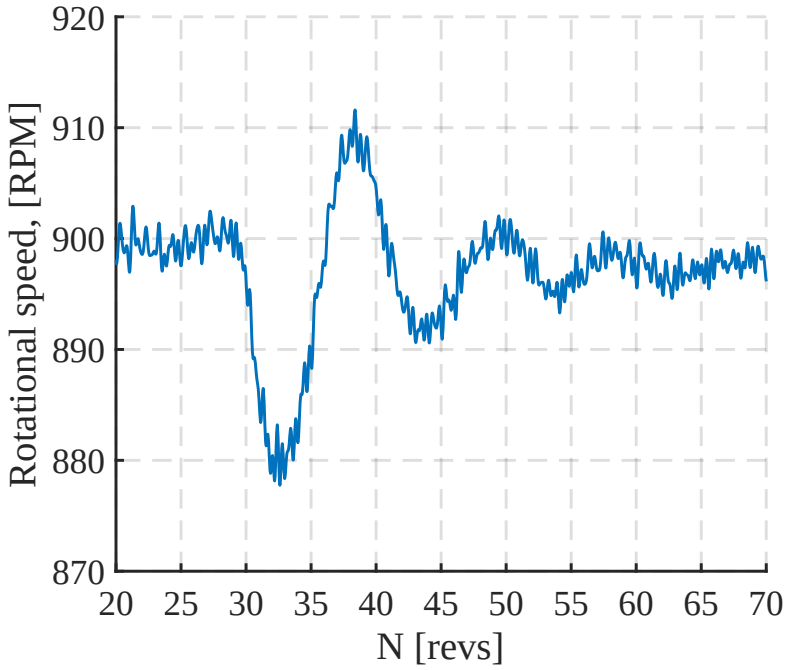

Figure 4.54: Rotational speed of the rotor as a function of rotor revolutions

step input and eventually stabilized at about 265 N.

On the other hand, the trend of the rotor torque was slightly different from that of the rotor thrust. Figure 4.56 shows the torque variation as a function of time, low-pass filtered at the 3dB cutoff frequency of 25 Hz. The rate of change of the rotor torque variation appeared to be monotonic unlike the trend of the thrust variation, and the torque reached its peak immediately after passing the 35th revolution and died out at around the 45th revolution. A possible reason for this trend difference is that there was a close correlation between the torque and the rotational speed variation and these two quantities had a pronounced influence on each other. The low-frequency rotor speed

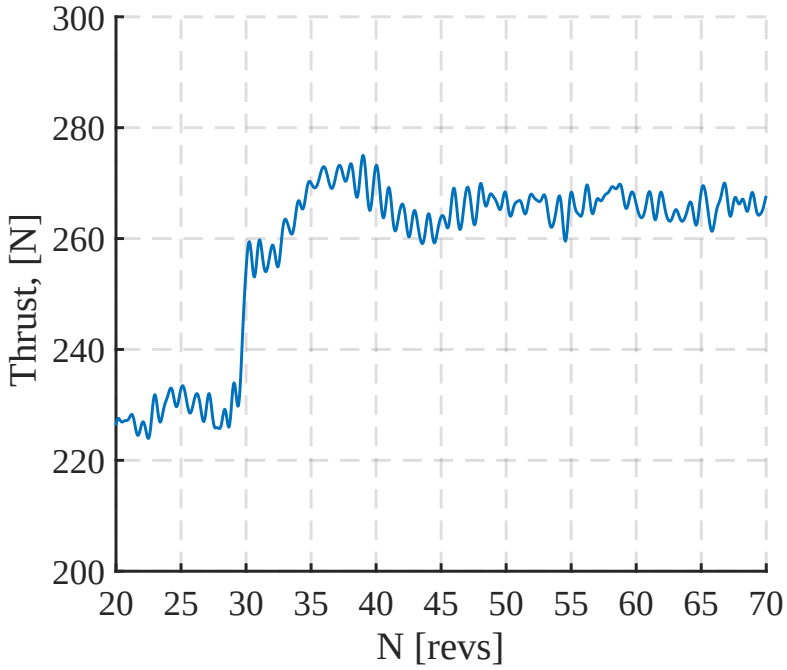

Figure 4.55: Rotor thrust response to the step pitch change as a function of rotor revolutions

ringing hence appeared more in the torque response, than in the responses of other measured quantities.

The pitch link loads variations, low-pass filtered at the 3 dB cutoff frequency of 8 Hz, for the two blade linkages are shown in Fig. 4.57. Recall that the negative slope (compression) and positive slope (tension) of the pitch link load variation correspond to the nose-up and -down motion of the rotor blade, according to the linkage mechanism (see § 3.1.2). In Fig. 4.57, the pitch link force first decreased at around the 28th revolution, associated with the beginning of the swashplate motion pushing the rotor blade (compression) to

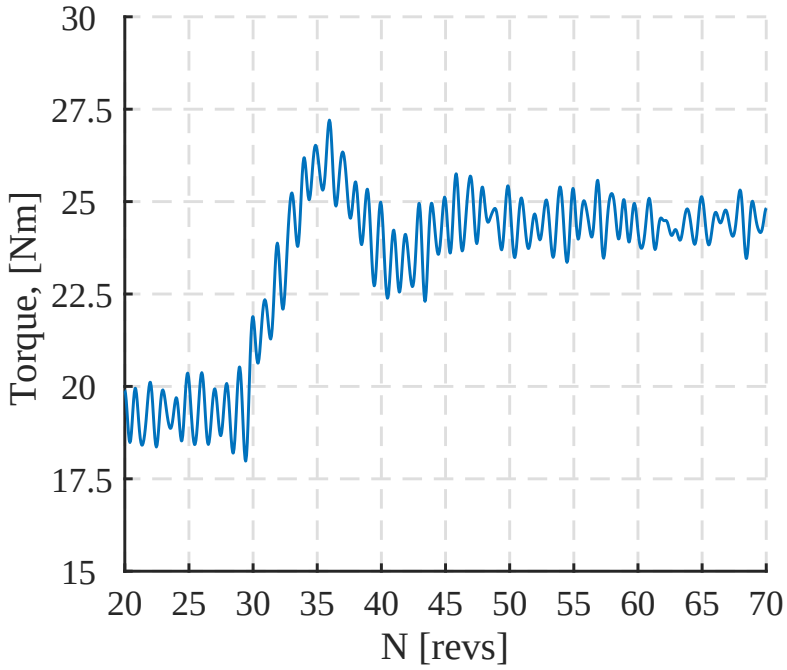

Figure 4.56: Rotor torque response to the step pitch change as a function of rotor revolutions

increase the blade pitch angle. Then, the pitch link force started increasing after passing the 30th revolution and overshot at about the 35th revolution, because of the increase in blade pitch moment in nose-down direction (tension). Hence, the trends observed in Fig. 4.57 adequately represent the blade pitch moment (aerodynamic and inertial) attributed to the dynamic collective step change.

The loads estimation methodology first computed the integrated inertial load at the rotor hub as a function of the number of revolutions, as shown in Fig. 4.58. The inertial load was obtained by the numerical differentiation

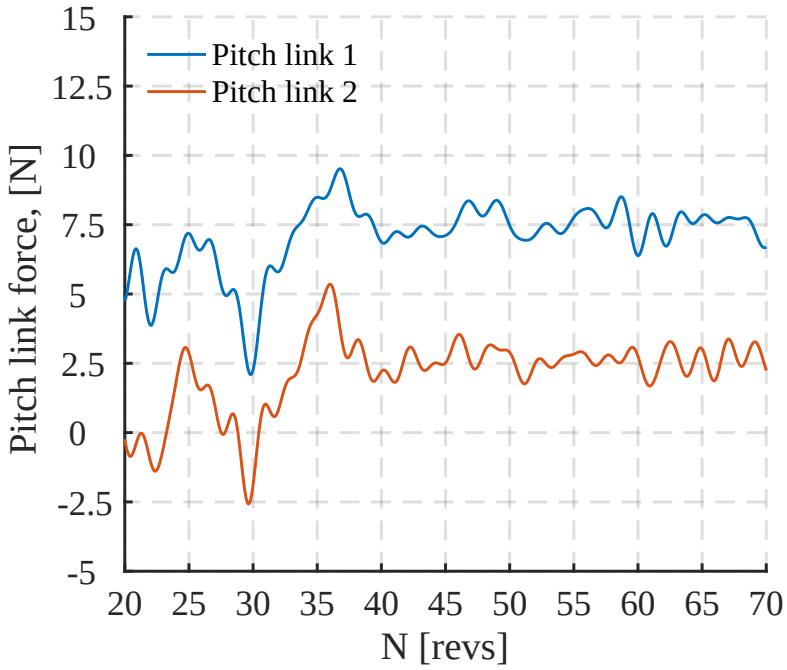

Figure 4.57: Pitch link force response to the step pitch change as a function of rotor revolutions

of the out-of-plane deformation time history in time, multiplied by the mass property of the blade structure. Note that the time history of the flap bending deformation was smoothed by 3rd-order polynomial curve fit prior to the numerical differentiation. In Fig. 4.58, there was a small fluctuation before the step pitch input was applied, and the maximum load of 7.5 N was observed immediately after the step input applied during the 28th revolution. The oscillation induced by the step lasted for approximately 300 milliseconds, which was equivalent to 4.5 revolutions.

The time history of the integrated hub load for the test condition 3

was estimated and compared to the measured thrust variation, as shown in Fig. 4.59. The resultant increase in rotor thrust due to the collective step change was found to be consistently 40 N in both the measured and estimated profile; however, there was a constant magnitude offset of approximately 15 N and a slight time lag of step response between the measured and estimated thrust. The former concern was consistently observed for all three operating conditions (the constant collective pitch input, the 1/rev periodic pitch input, and this collective step pitch input) on the same order of magnitude (10-15 N), which could possibly be explained by the area difference under the original

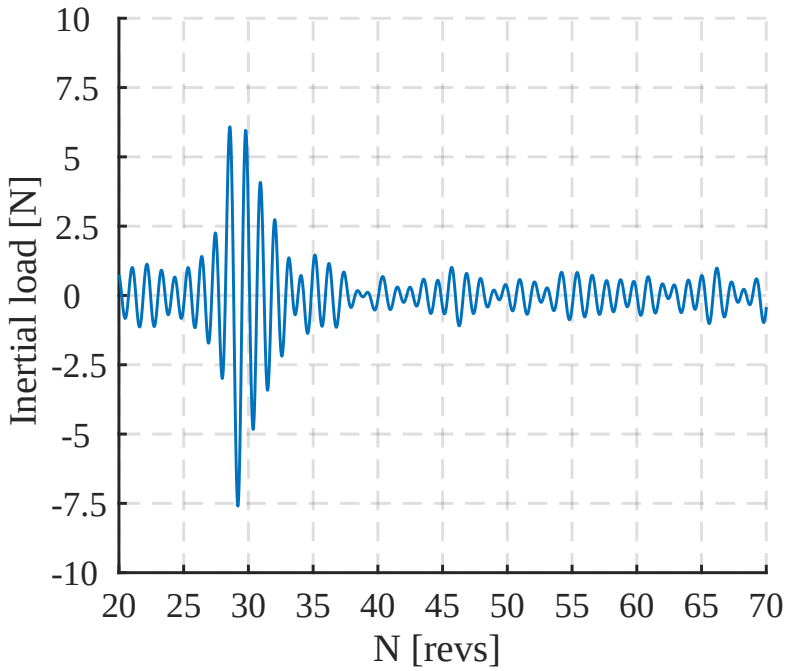

Figure 4.58: The estimated inertial load integrated at the hub as a function of the number of revolutions for the collective step pitch change (Test condition 3)

and estimated spanwise lift curve; (see Fig. 2.11). The latter concern could be because of the nature of this load estimation methodology, i.e., the estimated loads were purely based on rotor blade structural deformation measured by the non-contact optical technique (DIC), whereas the hub loads measured by the load cell contained a large number of experiment-specific factors, such as linkage mechanism, free-play and lubrication in bearings, non-ideal aerodynamic interaction with the experimental setup, or the recirculation effect in the hover test chamber. These factors might cause the constant magnitude offset and time lag between the measured and estimated thrust response; further investigation must be performed as future work.

In addition to the constant shift in mean thrust, the estimated thrust exhibits a steeper jump than the measured trend. A possible cause for the trend difference is the fact that the measured quantities in this test case were contaminated by the variation of rotational speed as mentioned before (see Fig. 4.54). Although the blade deformation measured during the test was also affected by the rotor speed change, the influence was less significant on the blade structural response measured by the non-contact optical DIC technique than that on the rotor loads measured by the load cell directly mounted on the rotor stand.

In conclusion, the integrated hub load estimation showed satisfactory agreement with the measured thrust variation for all the operating (loading) conditions, although the lack of the higher modes participation caused poor estimation of the spanwise lift distribution, particularly at regions of the blade

tip. Nevertheless, it must be emphasized that this rotor load estimation was not made by complicated, troublesome on-blade sensors but achieved by processing the sequence of digital images taken during the hover tests, and the only preparation on the blade structure was the orange fluorescent paint with random speckle patterns using a spray lacquer and a black-ink marker.

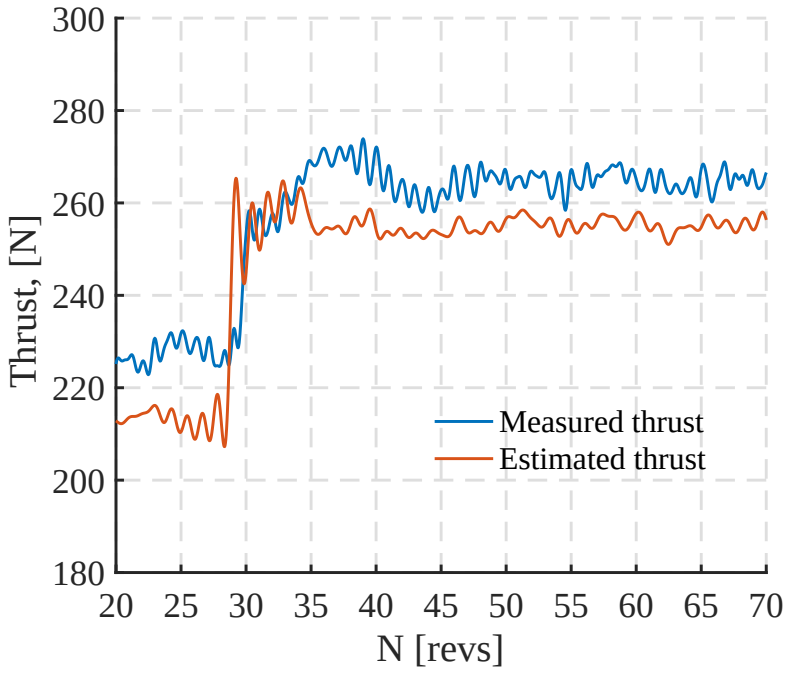

Figure 4.59: Comparison between the estimated and measured rotor hub loads for the collective step pitch change (Test condition 3)

Chapter 5

Summary, Conclusions, and Future Work

5.1 Summary and Conclusions

A helicopter rotor loads estimation methodology based on blade structural response was formulated and validated. The primary objective of this study was to develop an experimental and theoretical methodology to obtain helicopter rotor loads, without using conventional on-blade sensors. The theoretical framework of the methodology consists of three key components: (1) blade deformation time history measurement using a non-contact optical technique called Digital Image Correlation (DIC), (2) rotor blade modal properties identification using Operational Modal Analysis (OMA), and (3) rotor loads estimation methodology based on blade structural deformation and modal parameters. To verify the applicability and robustness of the proposed methodology, a series of measurements were performed in hover on a 0.46 m-diameter, small-scale rotor hover test rig and a 2 m-diameter, large-scale rotor hover test rig at several rotor configurations and operating conditions.

The 0.46 m-diameter, small-scale rotor consisted of two extremely flexible blades and a fixed-pitch hub. The three-dimensional (3D) deformation time history of the small-scale rotor blade was measured by the time-resolved

DIC technique at four different root pitch angles (0°-30°) and rotational speeds (600-1500 RPM). The time-resolved DIC was achieved by (i) taking a sequence of digital images over the whole rotor disk by stereoscopic high-speed cameras, (ii) illuminating the surface of the rotor blade painted with fluorescent orange and stochastic speckle pattern by laser light, and (iii) triggering image acquisition and laser strobe timing with a downsampled (16/rev) digital pulse train generated from an optical encoder. Blade deformation measurements consisted of the flap, lead-lag, and torsional deformation over 400 revolutions at approximately 900 measurement channels over the entire rotor span at 16 evenly-spaced azimuthal locations. The measurements revealed that the time-resolved DIC technique developed in this dissertation can be used to measure the rotating blade deformation on the order of a few millimeters.

To expand the applicability of the time-resolved DIC, several measurements were performed on the 2 m-diameter, large-scale rotor hover test rig spun at 900 RPM at different rotor configurations and operating conditions. The same methodology as the small-scale testing, i.e., the time-resolved DIC with laser strobing and fluorescence paint, was applied to the large scale rotor blade deformation measurement. First, the DIC technique was applied to the single-bladed, coaxial counter-rotating (CCR) rotor blade deformation measurement and these experimental results were compared with a well-validated numerical model. Overall, there was excellent agreement between the measured and predicted flap bending deformations. The maximum tip deflection of the CCR lower rotor blade reached 74.6 mm, which is approximately 10

times larger than the tip deflection of the small-scale rotor. The time-resolved DIC successfully demonstrated its capability of measuring the deformation time history of a rotating blade at different measurement scales.

Additional blade deformation measurements were performed on the large-scale, two-bladed, isolated single rotor with the hydraulic actuation system. The goal was to verify if the time-resolved DIC can measure rotor blade responses to a variety of loading conditions, including (i) a steady collective pitch input at a blade loading of 0.125, (ii) a 1/rev periodic pitch input, and (iii) a collective step pitch input. For the first test condition, deformations were measured and examined from various perspectives: out-of-plane blade deformation over the entire rotor disk, 3D static deformation distributed over the blade span, static deformations of each degree-of-freedom (flap, lead-lag, and torsion) along the blade quarter-chord axis, and blade tip displacement as function of azimuthal angle. For the second test condition, the tip deflection difference between the maximum and minimum reached approximately 75 mm, thus it was demonstrated that this large sinusoidal oscillatory motion of the 2 m-diameter rotor at 1/rev frequency (15 Hz) was successfully captured by the DIC technique. For the third test condition, out-of-plane, in-plane, and local blade pitch responses to the collective step input were successfully captured.

The measured deformations were input to two OMA algorithms (NExT-ERA or CP algorithm) to identify the modal frequencies, mode shapes, and damping ratios in the rotating frame. The modal parameter identification was first performed on the small-scale rotor blade. The first two modes were identi-

fied using these two OMA algorithms. To quantify the differences between the measured and predicted mode shapes, Modal Assurance Criterion (MAC) was used as a measure of agreement between two vectors. The modal frequencies and mode shapes identified by the CP algorithm agreed well with numerical predictions, however, there was some discrepancy between mode shapes identified by NExT-ERA and numerical prediction. All the modal damping values extracted by the NExT-ERA analysis were less than 3% as was the case of the CP analysis. While the NExT-ERA required a number of steps and choices of parameters based on experience or trial-and-error, the CP algorithm was quite simple to implement and did not require any tuning of parameters. Thus, the CP algorithm was selected as a primary OMA algorithm for modal identification of the large-scale rotor blade.

For the large-scale rotor blade modal identification, two different types of excitation to the rotor blade were tested: (i) random excitation at zero mean thrust and (ii) collective step input excitation. Overall, the modal extraction algorithm based on the random response successfully identified the first flap, first lag, and second flap frequencies and mode shapes. Using the MAC, it was demonstrated that there was excellent agreement between mode shapes extracted by the CP algorithm and the numerical model. On the other hand, the CP analysis extracted only the first two flap modes from the response to the collective step change. The spectrogram of the same data set showed that wide-bandwidth vibration was propagated when the step change occurred, however, this response immediately died out after the step. Hence, the first

three modes identified in the test case (i) (random excitation) were used for rotor loads estimation.

Rotor loads measurement was first performed on the large-scale, single-bladed CCR lower rotor at a blade loading of 0.09, simultaneously with the blade deformation measurement. A significant 2/rev component was observed in the lower rotor thrust and pitch link load with satisfactory agreement of the magnitude to numerically predicted results. The vibratory thrust was approximately 10% of the mean thrust, whereas the vibratory pitch link load was found to be nearly 30% of the mean pitch link force. With these results from measurements on the large-scale rotor test rig, it is found that the three essential measured quantities (blade deformation, blade modal properties, and rotor loads) were well correlated with the numerical prediction.

Finally, rotor loads were estimated based on the measured blade deformation and modal parameters identified by the CP algorithm. Rotor loads estimation includes the spanwise lift distribution along the blade quarter-chord axis and hub loads (thrust) obtained by numerical integration of the lift distribution in the spanwise direction. Note that the modal parameters for the first and second flap modes were used for rotor loads estimation because the lag mode does not contribute to the out-of-plane lift force reconstruction. Data sets taken at (1) a constant pitch, (2) a 1/rev periodic pitch, and (3) a collective step pitch on the large-scale, two-bladed rotor were used. For all the test conditions, the estimated sectional lift distribution failed to capture the typical trend of lift loss in regions of the blade tip induced by the trailed tip

vortices, due to the limited number of participating modes for load reconstruction. However, the integrated thrust agrees well with the directly-measured value for the three test cases, possibly due to the fact that the areas under the estimated and original lift curve are close to each other even if only a few modes are used for the estimation. In conclusion, the rotor loads estimation methodology is a powerful tool to obtain a rough estimate of the rotor hub loads without using on-blade instrumentation. To accurately estimate the spanwise lift distribution, a larger number of modes must be included.

5.2 Future work

Overall, the time-resolved DIC technique sufficiently shows its applicability to blade deformation measurement at a variety of different rotor configurations and operating conditions in this study. For further validation of the DIC measurement technique, simultaneous deformation measurements using different experimental approaches should be performed; for example, the pitch angle at the blade tip can be relatively easily measured using in-plane photogrammetry which locates high-speed cameras in the rotor plane and captures images of the rotor blade cross-section at the tip. Comparing results with the DIC-obtained pitch angle, one can validate the correctness of the DIC blade deformation measurement to some extent.

Additionally, regarding the DIC deformation measurement, the current study mainly focused on the blade deformation along the blade quarter-chord axis or the particular measurement point at the blade tip. The 3D DIC de-

formation measurement sometimes requires an analyst to deal with an unnecessarily large number of data points in space over the entire blade span. To effectively utilize the significant amount of measured information, spatial averaging over the neighborhood is suggested; instead of tracking one particular measurement point that corresponds to a single interrogation window, averaging 3D deformations over the neighborhood points in both spanwise and chordwise directions might effectively eliminate noise and outliers in raw data.

The DIC-OMA combined approach failed to identify structural modes higher than the third mode for both the small- and large-scale rotor blade. Since higher modes oscillate with small amplitudes, deformations might approach the noise floor of the DIC technique. Increasing the signal-to-noise ratio for improvement in resolution is essential to enable the identification of higher modes. One simple suggestion for measuring vibration for the higher-order modes could be to increase input excitation forcing to the rotor blade structure so that large elastic deformations can be obtained. Another approach could be to implement post-processing algorithms, such as the motion magnification technique, to magnify small deformation so that vibration over the specified bandwidth can be emphasized and easily picked.

The cause of low values of modal damping extraction is unclear; there is room for improvement in modal damping identification. However, specifically for the case of helicopter blade motion, the flap damping term comes from aerodynamic damping and is very high; for example, a typical articulated rotor (Lock number = 8) has a 50% flap damping ratio in hover. Flapping

motion tends to die out rapidly due to the high damping. Thus, the estimation of damping remains the most difficult part of modal analysis in helicopter rotor blade dynamics.

Investigating the reason for the discrepancy between results of NExT-ERA analysis and numerical prediction remains an important area of future work, and underlines the sensitivity of this technique to the selection of processing parameters and post-processing steps.

The measured deformation and loads of the single-bladed CCR rotor during the Test campaign 2 contained a large 1/rev component along with significant odd harmonics, although only even harmonics are expected for a single-bladed CCR rotor system. The 1/rev and odd harmonics could be attributed to aerodynamic interference with the rotor stand support structure as well as the effect of having dissimilar rotor blades, on each single-bladed rotor with a counter-weight. Additionally, the measured quantities obtained during the Test campaign 3 (the two-bladed, isolated single rotor) contained some non-negligible fluctuations. Mean flow recirculation in the closed hover test chamber might also be one of the sources for these non-ideal fluctuations observed in data. Another possible source is the presence of viscous damping in the bearing mechanism and its lubrication for rotor feathering motion, as well as some free-play in blade pitch linkage mechanism. Future work includes improvements in the experimental setup to minimize the unnecessary harmonic contents and fluctuations in the measured blade deformations and rotor loads.

Regarding the rotor loads estimation, the tip lift loss induced by the

trailed tip vortices was not quite captured due to the lack of participating modes in the estimation process. However, the tip loss might be relatively easily corrected by introducing an additional well-known shape function, such as the Prandtl tip loss function, to the estimation process, instead of struggling to identify the higher-order structural modes. The tip loss correction could not only help one to accurately reconstruct the spanwise lift distribution, but also address the consistently-observed 5% mean value offset in the estimated hub loads estimation.

One possible application of the current methodology is to derive and estimate the blade structural properties based on the estimated modes. This study used uniform, untwisted, simple blade structure for proof of concept. However, actual helicopter blades generally have non-uniform cross-section, complicated composite blade structure whose properties cannot be readily obtained. If the DIC-OMA approach can be scaled up to a full-scale, actual helicopter blade, its structural properties are obtained by only processing a sequence of digital images of the blade structure. This process is a typical usage of the operational modal analysis, that is, the primary goal of modal parameter identification (or modal testing) is to fine-tune a finite element model of a structure using experimentally-obtained modal properties. Thus, the DIC-OMA combined approach has the potential for significantly reducing the time and cost of modal testing on full-scale helicopter rotor blades.

Improvement of rotor loads estimation will eventually lead to further validation of a computational model. Accurate prediction of transient heli-

copter rotor loads will provide a foundation to develop methods to mitigate vibration in future helicopter design.

Bibliography

[1] An image of a static display of the CH-53 Sea Stallion. Downloaded from https://www.military.com/equipment/ch-53d-sea-stallion.

[2] An image of the CH-53 Sea Stallion taken under operation. Downloaded from https://commons.wikimedia.org/wiki/File:CH-53_Sea_Stallion_-_Side_View_(Balikatan_2016).JPG.

[3] J. P. Jr. Rabbott, A. A. Lizak, and V. M. Paglino. A Presentation of Measured and Calculated Full-scale Rotor Blade Aerodynamic and Structural Loads. *USAAVLABS Technical Report 66-31*, 1966.

[4] R. M. Heffernan and M. Gaubert. Structural and Aerodynamic Loads and Performance Measurements of an SA349/2 Helicopter with an Advanced Geometry Rotor. *NASA Technical Memorandum 88370*, 1986.

[5] R. M. Kufeld, D. L. Balough, J. L. Cross, K. F. Studebaker, C. D. Jennison, and W. G. Bousman. Flight Testing of the UH-60A Airloads Aircraft. *Proceedings of the 50th Annual Forum of the American Helicopter Society*, Washington, D. C., May 11-13, 1994.

[6] W. G. Bousman. Estimation of Blade Airloads from Rotor Blade Bending Moments. *NASA Technical Memorandum 100020*, 1987.

[7] G. Wang, A. Abhishek, I. Chopra, N. Phan, and D. Liebschutz. Rotor Loads Prediction Using Estimated Modal Participation from Sensors. *39th European Rotorcraft Forum Proceedings*, Paris, France, Sept. 9-11, 2010.

[8] J. Sirohi and M. S. Lawson. Measurement of helicopter rotor blade deformation using digital image correlation. *Optical Engineering*, 51(4), pp. 043603, 2012.

[9] J. Sicard and J. Sirohi. Measurement of the deformation of an extremely flexible rotor blade using digital image correlation. *Measurement Science and Technology*, 24(6), pp. 065203, 2013.

[10] G. C. Cameron, D. Uehara, and J. Sirohi. Transient Hub Loads and Blade Deformation of a Mach-Scale Coaxial Rotor in Hover. *56th AIAA/ASCE/AHS/ASC Structures, Structural Dynamics, and Materials Conference*, Kissimmee, Florida, Jan. 5-9, 2015.

[11] S. S. Rizo-Patron and J. Sirohi. Operational Modal Analysis of a Helicopter Rotor Blade Using Digital Image Correlation. *Experimental Mechanics*, 57(3), pp. 367–375, 2017.

[12] J. Baqersad, P. Poozesh, C. Niezrecki, and P. Avitabile. Photogrammetry and optical methods in structural dynamics – A review. *Mechanical Systems and Signal Processing*, 86(B), pp. 17–34, 2017.

[13] J. P. Sevenhuijsen. The photonical, pure grid method. *Optics and Lasers in Engineering*, 18(3), pp. 173–194, 1993.

[14] R. Kube, W. R. Splettstoesser, W. Wagner, U. Seelhorst, Yu. Y. H., C. Tung, P. Beaumier, J. Prieur, G. Rahier, P. Spiegel, A. Boutier, T. F. Brooks, C. L. Burley, D. D. Boyd Jr., E. Mercker, and K. Pengel. HHC aeroacoustic rotor tests in the German-Dutch wind tunnel: Improving physical understanding and prediction codes. *Aerospace Science and Technology*, 2(3), pp. 177–190, 1998.

[15] A. Macovski, S. D. Ramsey, and L. F. Schaefer. Time-lapse interferometry and contouring using television systems. *Applied Optics*, 10(12), pp. 2722–2727, 1971.

[16] O Lekberg. Electronic Speckle Pattern Interferometry. *Physics in Technology*, 11(1), pp. 16–22, 1980.

[17] G. A. Fleming and S. A. Gorton. Measurement of Rotorcraft Blade Deformation Using Projection Moiré Interferometry. *Shock and Vibration*, 7(3), pp. 149–165, 2000.

[18] G. A. Fleming and S. Gorton. Projection Moiré Interferometry for rotorcraft applications: deformation measurement of active twist rotor blades. *Proceedings of the 58th Annual Forum of the American Helicopter Society*, Montreal, Quebec, June 11-13, 2002.

[19] M. K. Sekula. The Development and Hover Test Application of a Projection Moiré Interferometry Blade Displacement Measurement System. *Proceedings of the 68th Annual Forum of the American Helicopter Society*, Fort Worth, TX, May 1-3, 2012.

[20] M. Ozbek, D. J. Rixen, O. Erne, and G. Sanow. Feasibility of monitoring large wind turbines using photogrammetry. *Energy*, 35(12), pp. 4802–4811, 2010.

[21] M. Ozbek and D. J. Rixen. Optical Measurements and Operational Modal Analysis on a Large Wind Turbine: Lessons Learned. *29th IMAC, a Conference on Structural Dynamics*, Jacksonville, Florida, Jan. 31 - Feb. 3, 2011.

[22] M. Ozbek and D. J. Rixen. Operational modal analysis of a 2.5 MW wind turbine using optical measurement techniques and strain gauges. *Wind Energy*, 16(3), pp. 367–381, 2013.

[23] O. Schneider. Analysis of SPR Measurements from HART II. *Aerospace Science and Technology*, 9(5), pp. 409–420, 2005.

[24] A. L. Abrego, L. E. Olson, E. A. Romander, D. A. Barrows, and A. W. Burner. Blade Displacement Measurement Technique Applied to a Full-Scale Rotor Test. *Proceedings of the 68th Annual Forum of the American Helicopter Society*, Fort Worth, TX, May 1-3 2012.

[25] T. Lundstrom, J. Baqersad, and C. Niezrecki. Monitoring the Dynamics of a Helicopter Main Rotor with High-Speed Stereophotogrammetry. *Experimental Techniques*, 40(3), pp. 907–919, 2016.

[26] J. Javh, J. Slavic, and M. Boltezar. High frequency modal identification on noisy high-speed camera data. *Mechanical Systems and Signal Processing*, 98, pp. 344–351, 2018.

[27] W. H. Peters and W. F. Ranson. Digital Imaging Techniques in Experimental Stress Analysis. *Optical Engineering*, 21(3), pp. 427–431, 1982.

[28] M. Sutton, W. J. Wolters, W. H. Peters, W. F. Ranson, and S. R. McNeil. Determination of Displacements Using an Improved Digital Image Correlation Method. *Image and Vision Computing*, 1(3), pp. 133–139, 1983.

[29] Z. L. Kahn-Jetter and T. C. Chu. Three-Dimensional Displacement Measurements Using Digital Image Correlation and Photogrammic Analysis. *Experimental Mechanics*, 30(1), pp. 10–16, 1990.

[30] T. C. Chu, W. F. Ranson, and M. A. Sutton. Applications of Digital Image Correlation Techniques to Experimental Mechanics. *Experimental Mechanics*, 25(3), pp. 232–244, 1985.

[31] S. R. McNeill, M. A. Sutton, Z. Miao, and J. Ma. Measurement of Surface Profile Using Digital Image Correlation. *Experimental Mechanics*, 37(1),

pp. 13–20, 1997.

[32] J. Tyson, T. Schmidt, and K. Galanulis. Advanced Photogrammetry for Robust Deformation and Strain Measurement. *SEM 2002 Annual Conference Proceedings*, Milwaukee, WI, June 10-12, 2002.

[33] T. Schmidt, J. Tyson, and K. Galanulis. Full-Field Dynamic Displacement and Strain Measurement Using Advanced 3-D Image Correlation Photogrammetry: Part 1. *Experimental Techniques*, 27(3), pp. 47–50, 2003.

[34] J. Tyson, T. Schmidt, and K. Galanulis. Biomechanics Deformation and Strain Measurements with 3D Image Correlation Photogrammetry. *Experimental Techniques*, 26(5), pp. 39–42, 2002.

[35] C. Cameron, J. Sirohi, R. Feil, and J. Rauleder. Measurement of transient loads and blade deformation in a coaxial counter-rotating rotor. *Proceedings of the 73rd Annual Forum of the American Helicopter Society*, Fort Worth, Texas, May 9-11, 2017.

[36] S. R. Ibrahim and E. C. Milkulcik. The Experimental Determination of Vibration Test Parameters from Time Responses. *The Shock and Vibration Bulletin*, 46(5), pp. 187–196, 1976.

[37] S. R. Ibrahim and R. S. Pappa. Large Modal Survey Testing Using the Ibrahim Time Domain Identification Technique. *Journal of Spacecraft and Rocket*, 19(5), pp. 459–465, 1982.

[38] J. N. Juang and R. S. Pappa. An Eigensystem Realization Algorithm for Modal Parameter Identification and Model Reduction. *Journal of Guidance, Control, and Dynamics*, 8(5), pp. 620–627, 1985.

[39] Z. Ma, S. Ahuja, and C. W. Rowley. Reduced-order models for control of fluids using the Eigensystem Realization Algorithm. *Theoretical and Computational Fluid Dynamics*, 25(1-4), pp. 233–247, 2011.

[40] Q. Qin, H. B. Li, L. Z. Qian, and C.-K. Lau. Modal identification of tsing ma bridge by using improved eigensystem realization algorithm. *Journal of Sound and Vibration*, 247(2), pp. 325–341, 2001.

[41] G. H. III James, T. G. Carne, and J. P. Lauffer. The Natural Excitation Technique (NExT) for Modal Parameter Extraction from Operating Wind Turbines. Technical Report SAND 92-1666, Sandia National Labs, Albuquerque, NM, 1993.

[42] M. H. Hansen, K. Thomsen, P. Fuglsang, and T. Knudsen. Two methods for estimating aeroelastic damping of operational wind turbine modes from experiments. *Wind Energy*, 9(1-2), pp. 179–191, 2006.

[43] T. G. Carne and G. H. James III. The inception of OMA in the development of modal testing technology for wind turbines. *Mechanical Systems and Signal Processing*, 24(5), pp. 1213–1226, 2010.

[44] E. D. Lorenzo, G. Petrone, S. Manzato, B. Peeters, W. Desmet, and F. Marulo. Damage detection in wind turbine blades by using operational

modal analysis. *Structural Health Monitoring*, 15(3), pp. 289–301, 2016.

[45] P. Comon and C. Jutten. *Handbook of Blind Source Separation: Independent Component Analysis and Applications*. Academic Press, Oxford, UK, 2010.

[46] A. D. Back and A. S. Weigend. A First Application of Independent Component Analysis to Extracting Structure from Stock Returns. *International Journal of Neural Systems*, 8, pp. 473–484, 1997.

[47] T.-P. Jung, S. Makeig, M. J. McKeown, A. J. Bell, T.-W. Lee, and T. J. Sejnowski. Imaging Brain Dynamics Using Independent Component Analysis. *Proceedings of the IEEE*, 89(7), pp. 1107–1122, 2001.

[48] M. J. Roan, L. H. Erling, and L. H. Sibul. A New Non-linear, Adaptive, Blind Source Separation Approach to Gear Tooth Failure Detection and Analysis. *Mechanical Systems and Signal Processing*, 16(5), pp. 719–740, 2002.

[49] G. Kerschen, F. Poncelet, and J. C. Golinval. Physical Interpretation of Independent Component Analysis in Structural Dynamics. *Mechanical Systems and Signal Processing*, 21(4), pp. 1561–1575, 2007.

[50] J. Stone. Blind Source Separation Using Temporal Predictability. *Neural Computation*, 13, pp. 1559–1574, 2001.

[51] Y. Yang and S. Nagarajaiah. Blind Modal Identification of Output-only Structures in Time-domain Based on Complexity Pursuit. *Earthquake Engineering Structural Dynamics*, 42, pp. 1885–1905, 2013.

[52] M. Chierichetti, C. McColl, D. Palmer, M. Ruzzene, and O. Bauchau. Combined Analytical and Experimental Approached to Rotor Components Stress Predictions. *The 1st Joint International Conference on Multibody System Dynamics*, Lappeenranta, Finland, May 25-27, 2010.

[53] H. G. Somerson. Approximation of Rotor Inflow and Flapwise Airload Distributions on Hinged Blades from Measured Strain and Motion Data. *Proceedings of the 13th Annual Forum of the American Helicopter Society*, Washington, D. C., May 8-11, May, 1957.

[54] H. Öry and H. W. Lindert. Reconstruction of Spanwise Air Load Distribution on Rotorblades from Structural Flight Test Data. *18th European Rotorcraft Forum*, Avignon, France, Sept. 15-18, 1992.

[55] L. ShouShen, J. P. Higman, and D. P. Schrage. Coupled Flap-Lag Rotor Blade Load Identification. *Proceedings of the 51st Annual Forum of the American Helicopter Society*, Fort Worth, TX, May 9-11, 1995.

[56] D. P. Schrage, Y. K. Yillikci, S. Liu, J. V. R. Prasad, and S. V. Hanagud. Instrumentation of the Yamaha R-50/RMAX Helicopter Testbeds for Airloads Identification and Follow-On Research. *25th European Rotorcraft Forum*, Rome, Italy, Sept. 14-16, 1999.

[57] D. Uehara, J. Sirohi, R. Feil, and J. Rauleder. Blade Passage Loads and Deformation of a Coaxial Rotor System in Hover. *Journal of Aircraft*, 2019.

[58] S. Yoneyama and G. Murasawa. Digital Image Correlation. *Experimental Mechanics*, 207, 2009.

[59] *LaVision 2017 Strain Master 3D, Software Package Version 8.4*. LaVision GmbH, Göttingen, Germany.

[60] J. M. Caicedo, S. J. Dyke, and E. A. Johnson. Natural Excitation Technique and Eigensystem Realization Algorithm for Phase I of the IASC-ASCE Benchmark Problem: Simulated Data. *Journal of Engineering Mechanics*, 130, pp. 49–60, 2004.

[61] P. D. Welch. The Use of Fast Fourier Transform for the Estimation of Power Spectra: A Method Based on Time Averaging Over Short, Modified Periodograms. *IEEE Transactions on Audio and Electroacoustics*, 15, pp. 70–73, 1967.

[62] C. R. Farrar and G. H. III. James. System Identification from Ambient Vibration Measurements on a Bridge. *Journal of Sound and Vibration*, 205(1), pp. 1–18, 1997.

[63] C. R. Farrar and D. A. Jauregui. Comparative Study of Damage Identification Algorithms Applied to a Bridge II: Numerical Study. *Smart Materials and Structures*, 7(5), pp. 721–731, 1998.

[64] L. Meirovitch. *Fundamentals of Vibrations.* McGraw-Hill Book, New York, NY, 2000.

[65] P. H. C. Eilers. A Perfect Smoother. *Analytical Chemistry*, 75(14), pp. 3631–3636, 2003.

[66] J. J. Stickel. Data Smoothing and Numerical Differentiation by a Regularization Method. *Computers and Chemical Engineering*, 34, pp. 467–475, 2010.

[67] W. Johnson. *Rotorcraft Aeromechanics.* Princeton University Press, 1980.

[68] J. G. Leishman. *Principles of Helicopter Aerodynamics.* Cambridge University Press, Cambridge, UK, 2006.

[69] A. Bagai. Aerodynamic Design of the X2 Technology Demonstrator™ Main Rotor Blade. *Proceedings of the 64th Annual Forum of the American Helicopter Society*, Montreal, Quebec, April 29 - May 1, 2008.

[70] C. G. Cameron. Comprehensive Aeromechanical Measurements of a Model-Scale, Coaxial, Counter-Rotating Rotor System. *Doctoral dissertation*, 2016.

[71] R. S. Pappa, J. T. Black, J. R. Blandino, T. W. Jones, P. M. Danehy, and A. A. Dorrington. Dot-Projection Photogrammetry and Videogrammetry of Gossamer Space Structures. *Journal of Spacecraft and Rockets*, 40(6), pp. 858–867, 2003.

[72] T. W. Jones, A. A. Dorrington, P. L. Brittman, and P. M. Danehy. Laser Induced Fluorescence for Photogrammetric Measurement of Transparent or Reflective Aerospace Structures. *49th Annual International Instrumentation Symposium*, Orlando, FL, May, 2003.

[73] A. A. Dorrington, T. W. Jones, P. M. Danehy, and R. S. Pappa. Laser-Induced-Fluorescence Photogrammetry for Dynamic Characterization of Membrane Structures. *AIAA Journal*, 42(10), pp. 2124–2129, 2004.

[74] A. A. Dorrington, T. W. Jones, and P. M. Danehy. Photophysics of Laser Dye-Doped Polymer Membranes for Laser-Induced Fluorescence Photogrammetry. *Applied Optics*, 43(36), pp. 6629–6638, 2004.

[75] D. Uehara and J. Sirohi. Full-field optical deformation measurement and operational modal analysis of a flexible rotor blade. *Mechanical Systems and Signal Processing*, 133, pp. 106265, November, 2019.

[76] J. Sicard and J. Sirohi. Modeling of the Large Torsional Deformation of an Extremely Flexible Rotor in Hover. *AIAA Journal*, 52(8), pp. 1604–1615, 2014.

[77] P. Mohanty and D. J. Rixen. Operational Modal Analysis in the Presence of Harmonic Excitation. *Journal of Sound and Vibration*, 270, pp. 93–109, 2004.

[78] A. Randall, J. The Modal Assurance Criterion – Twenty Years of Use and Abuse. *Sound and Vibration*, 37(8), pp. 14–23, 2003.

[79] D. Tcherniak, S. Chauhan, M. Rossetti, I. Font, J. Basurko, and O. Salgado. Output-only Modal Analysis on Operating Wind Turbines: Application to Simulated Data. *European Wind Energy Conference*, Warsaw, Poland, April 20-23, 2010.

[80] P. T. Brewick and A. W. Smyth. Exploration of the Impacts of Driving Frequencies on Damping Estimates. *Journal of Engineering Mechanics*, 141(3), pp. 30–48, 2015.

[81] D. Uehara, C. Cameron, , and J. Sirohi. Deformation Measurement and Modal Identification of an Extremely Flexible Rotor Blade. *6th Asian-Australian Rotorcraft Forum/Heli Japan*, Kanazawa, Japan, Nov. 7-9, 2017.

[82] C. Cameron, A. Karpatne, and J. Sirohi. Performance of a Mach-Scale Coaxial Counter-Rotating Rotor in Hover. *Journal of Aircraft*, 53(3), pp. 746–755, 2016.

Vita

Daiju Uehara was born in Okinawa, Japan. He received the Bachelor of Eng. in Aerospace Engineering at the University of Tokyo in 2014. Same year, he joined the UT Aeroelasticity Lab under Prof. Jayant Sirohi with a focus on an experimental study of a coaxial, counter-rotating rotor helicopter. He is a two-time winner of the Vertical Flight Foundation (VFF) scholarship from the American Helicopter Society/Vertical Flight Society, and also a recipient of the University of Texas Graduate Continuing Fellowship for 2018-2019. His recent work presented at AHS Forum 74 was recognized as the best paper for the Dynamics Sessions. He was a student intern at the NASA/Jet Propulsion Laboratory during summer 2018, and worked on the flight power modeling of small VTOL aircraft for exploration on Titan. Besides, he loves soccer.

Contact: udaiju9@gmail.com

This dissertation was typeset with LaTeX[†] by the author.

[†]LaTeX is a document preparation system developed by Leslie Lamport as a special version of Donald Knuth's TeX Program.